Design Strategies for Controlling Motion in Soft Robotic Systems

Design Strategies for Controlling Motion in Soft Robotic Systems

A dissertation presented
by

Nicholas Warren Bartlett

to
The School of Engineering and Applied Sciences
in partial fulfillment of the requirements
for the degree of
Doctor of Philosophy
in the subject of

Engineering Sciences

Harvard University
Cambridge, Massachusetts
October 2018

Dissertation advisor
Professor Robert J. Wood

Author
Nicholas Warren Bartlett

Design Strategies for Controlling Motion in Soft Robotic Systems

Abstract

The field of soft robotics has attracted much interest due to its promise of machines that are cheaper, safer, and more robust than their rigid counterparts. Despite rapid progress, there is an open question of how best to control these new types of robots. Applying control techniques from traditional robotics is far from trivial, largely due to the fundamentally different body plans of rigid and soft robots, and the highly nonlinear mechanics of elastomeric materials. This thesis proposes a holistic approach to control systems for soft robots, in which the controller is designed in parallel with robot morphology, actuation strategy, and overall system requirements. We distinguish between passive control strategies, in which some form of morphological computation is employed, and active control strategies, in which a user (or the environment) provides input. In the first part of this thesis we examine passive control. We present two novel fabrication paradigms that each establish a new class of soft robots, and show how fabrication and control are tightly coupled in each case. In the second part, we discuss how previous work in microfluidic logic can be adapted and improved to make it a viable option for active control in soft robotics. We conclude by outlining future research directions, and propose a way in which both passive and active control may be combined into a single comprehensive control strategy.

Contents

To Zoë, for everything

Acknowledgments

It is extraordinarily rare that anything is accomplished by a single person working in isolation, especially in such a collaborative enterprise as scientific research. As such, I have many people whom I would like to thank.

First and foremost, I would like to express my sincere thanks and gratitude to Professor Robert J. Wood, my advisor. He gives his students the space to explore ideas with total freedom, and yet is always willing to provide guidance when called upon. In his lab, Rob cultivates an environment of collaboration and openness, where ideas are shared and enthusiastically debated. Personally, he has made me a better researcher as well as a more critical thinker, both inside the lab and out. Rob is an inspirational figure, and it has been a privilege to work with him.

It has been humbling to work at an institution that attracts so many great minds; I have been lucky enough to interact with a number of them. Thank

you to the following Harvard faculty members for their mentorship, insight, and expertise: Professor Jennifer Lewis, Professor David Clarke, Professor Katia Bertoldi, Professor Conor Walsh, and Professor George Whitesides.

Thank you to the members of the Microrobotics Lab and neighboring labs for sharing in my research experience, and making the lab a fun place to work. A special acknowledgement is owed to a number of people who served as mentors and informal advisors, including James Weaver, Michael Tolley, Daniel Vogt, Michael Wehner, Tommaso Ranzani, Sheila Russo, and Oluwaseun Araromi.

I acknowledge how lucky I am to have been able to perform research in a setting where funding and resources are never a limitation on curiosity and intellectual exploration. Thank you to the National Defense Science and Engineering Graduate Fellowship, the Wyss Institute, and the Harvard School of Engineering and Applied Science, and to all of the people behind the scenes responsible for funding. Your generosity is very much appreciated.

A huge thank you, of course, to my parents, to whom I owe everything. Whether through a genuine interest in my research manifested in unceasing requests to explain that last point just one more time, or through finding heartfelt ways to celebrate the paper that was finally published or to recover from a failed experiment, your encouragement and support reminds me to reflect on how far I have come and motivates me to take the next step. Thank you for providing me with the opportunity to pursue my interests, academic or otherwise, and for all of the sacrifices that enabled that opportunity. To Charlie, who has been a brother, a friend, a roommate, and a role model; it would be hard

to ask for a better person to look up to. To my sister Caroline, who can always bring me down to Earth and remind me of the things that really matter.

Finally, to Zoë. Throughout my time in graduate school, you have been the first one to ask me how my day went, to share in the excitement of a new result, or simply to smile at me when I needed a friend. You have been more to me than I knew a person could be.

1

Introduction

This dissertation explores questions related to the control of soft robots. While "control" may have different meanings in different contexts, we are primarily concerned with control as it relates to effecting predictable motion in systems composed of soft materials, and how to best design and build soft systems so that they may be controllable. We believe that, within soft robotics,

questions related to control are inextricably linked to decisions made during the design and fabrication process; as such, we take a holistic, integrated approach, in which the distinction between the control system and the structure of the robot itself (or, between "brain" and "body", if you like) is not well defined.

Throughout this work, there are a number of recurring themes. The two primary physical parameters over which we have control are geometry and material. As such, careful attention is paid to questions of sizing and material choice from the outset of design. Despite these considerations, we do not always converge on the best solution from the first attempt. Consequently, we often take a highly iterative, experimental approach to design and fabrication, weighing practical considerations equally to academic ones, striving for design rules and fabrication paradigms that enable the creation of actual, functional robots.

1.1 Motivation: Why make robots soft?

When asked to imagine a robot, many people think of cold, metallic, humanoid machines akin to the cyborg popularized in the movie *The Terminator*. Alternatively, they might think of the extremely precise and incredibly fast robotic welding arms that are used in automobile assembly plants. Common to these prototypical examples are speed, precision, strength, and complexity. Traditional robots are often constructed from rigid metals that deform only minimally even under large loads, are powered by precision electric motors, and utilize feedback from high fidelity sensors to enable motion that is both accu-

rate and repeatable. However, with these impressive capabilities come significant limitations. Traditional robots are often heavy, expensive, and dangerous. Although extremely efficient in carrying out the task for which they were designed, these robots rarely adapt well to new tasks or new environments.

In light of these limitations, there has been much excitement of late surrounding soft robots[4]. In contrast to their rigid counterparts, soft robots are composed of flexible, compliant materials that easily deform. The advantages offered by soft robots have been argued in many review articles[115,33,81,43,60,94,49,82]. To a first approximation, a soft robot is that which a traditional, rigid robot is not. Whereas a rigid robot is fast and precise, with well understood kinematics, a soft robot is slow and its motion is often hard to predict. Whereas a rigid robot is a powerful, dangerous machine, soft robots often exert lesser forces and are thus safer. Whereas rigid robots are stiff and unyielding, soft robots conform to the targets of their interaction through compliance matching, and are often highly adaptable to their environments.

With this entirely open design space available to them, researchers in soft robotics often look to nature for inspiration, modeling their systems on invertebrates, such as cephalopods[65,98,48] and insect larvae[52], as well as vertebrates, including snakes[74] and fish[61]. The use of compliant materials facilitates the development of biologically inspired robotic systems that are more adaptable[105], safer[77,83], and more resilient[112] than their fully rigid counterparts.

1.2 Control challenges

For all of the benefits inherent in building robots out of soft materials, there are equally many challenges[53,13]. Soft robots are hard to control. While there are many factors that affect controllability, we will focus on just two. First, soft materials routinely undergo large strains that break many of the assumptions of simple, traditional mechanics models, quickly entering the regime of nonlinearity that can make an analytical approach intractable. Researchers are excited about exploring the possible uses of unusual materials exactly because of their nontraditional behavior, so this challenge is most often addressed, if at all, by opting for numerical methods over analytical ones, and not by seeking out more conservative materials. Second, soft robots do not have discrete joints, as do traditional rigid robots. As such, these systems are often described as possessing infinite degrees of freedom, making traditional feedback control systems difficult to apply. Some have suggested that this difficulty can be avoided by using polynomial approximations of continuous segments instead of traditional kinematic modeling techniques for discrete link robotic manipulators[62].

Despite the possible solutions to the challenges outlined above, many who work in soft robotics find that the results of modeling are simply not worth the effort. Much of the work seen to date in soft robotics has been experimental, due largely to difficulties in modeling, but also to short fabrication times and inexpensive materials. Often, it is simply less resource intensive (in terms of time, money, and effort) to take an iterative, experimental approach to design

and fabrication. As designs evolve quickly, it is often prudent to adopt a control strategy that is easily reconfigurable, prompting soft robotics researchers to gravitate towards microcontrollers and computers that can be reprogrammed at will. That is to say, many controllers seen in soft robotics are ad hoc, with too little time devoted to drawing general conclusions that may be applied beyond the specific system in question.

1.3 Contributions and chapter organization

In this work, we investigate the question of control for soft robots in pursuit of design rules and fabrication paradigms that may be valuable across diverse body morphologies. We take both a bottom–up approach, in which we consider how specific decisions made during design and fabrication alter the behavior of the full system, as well as a top–down approach, in which the behavior of the entire system is the first, and often driving, consideration. The bottom–up approach is related to ideas of emergence, embodiment, mechanical intelligence, and morphological intelligence[80,79]; generally, we refer to this approach as "passive control". The top–down approach is much more akin to traditional control strategies, in which high-level directives are considered; we refer to this approach as "active control".

Broadly, this dissertation may be thought of as two parts. Part I includes Chapters 2 and 3, and examines the idea of passive control through two case studies. Part II is made up of Chapters 4, 5, and 6, and explores the possibil-

ity of active control, examining in detail one possible implementation. Chapter 7 provides a summarizing discussion and suggests how these two approaches to soft robotic control may be reconciled in a single, coherent control strategy.

In Chapter 2, we present a strategy to fabricate soft robots with passive control through multimaterial 3D printing. Specifically, we propose that printing a material stiffness gradient that allows the robot body to transition from fully rigid to entirely soft results in increased locomotive performance as well as resilience. In addition, this fabrication paradigm suggests one solution to a ubiquitous problem in soft robots, which is frequent failure at the interface between the soft body and any rigid driving components due to high stress concentrations derived from compliance incompatibility.

In Chapter 3, we explore the potential benefits of combining various established fabrication strategies in a novel process, and characterize the resulting capabilities that are unique to this combination. Whereas Chapter 2 considered cutting edge additive manufacturing techniques, this chapter instead examines a creative integration of well known planar manufacturing processes including laser micromachining, multilayer soft lithography, and precision pin alignment for laminate assembly. This approach enables the fabrication of soft robots at small scale with unmatched complexity.

In Chapter 4, we begin our examination of active control. We propose a fluidic system of control that relies on the manipulation of, and interaction between various fluid-carrying channels. As such, this chapter is concerned primarily with the appropriate design of these fluidic channels, and an exhaustive

study into the relative benefits of different fabrication methodologies.

In Chapter 5, we use our knowledge of microchannel design and fabrication to explore the next building block of our system of active control. That is, we design and characterize a microfluidic valve, and prove its functionality in a multiplexing scheme that enables a user to address a large number of actuators with just a few control inputs.

In Chapter 6, we discuss a process to generalize the system of active fluidic control presented in the previous chapter. We detail the governing equations and their limitations, and explore a framework through which the microchannels and microfluidic valves that we have studied may be combined in a system of digital fluidic logic, enabling soft robots of unprecedented complexity.

Finally, in Chapter 7, we conclude with some suggestions on how passive and active control may be combined. To do so, we outline specific future research directions, and propose some resources for inspiration.

1.4 Previously published manuscripts

Much of the content of this dissertation has been published previously:

Tolley, M. T., Shepherd, R. F., Karpelson, M., **Bartlett, N. W.**, Galloway, K. C., Wehner, M., Nunes, R., Whitesides, G. M., & Wood, R. J. (2014, September). An untethered jumping soft robot. In *Intelligent Robots and Systems (IROS 2014), 2014 IEEE/RSJ International Conference on* (pp. 561-566). IEEE.

Bartlett, N. W., Tolley, M. T., Overvelde, J. T., Weaver, J. C., Mosadegh, B., Bertoldi, K., Whitesides, G. M., & Wood, R. J. (2015). A 3D-printed, functionally graded soft robot powered by combustion. *Science*, 349(6244), 161-165.

Trimmer, B., **Bartlett, N. W.**, & Tolley, M. T. (2015). New Developments in Soft Robotics: An Interview with Nicholas W. Bartlett and Michael T. Tolley. *Soft Robotics*, 2(3), 93-95.

Ranzani, T., Russo, S., **Bartlett, N. W.**, Wehner, M., & Wood, R. J. (2018). Increasing the Dimensionality of Soft Microstructures through Injection-Induced Self-Folding. *Advanced Materials*, 30(38), 1802739.

Bartlett, N. W., & Wood, R. J. (2016). Comparative analysis of fabrication methods for achieving rounded microchannels in PDMS. *Journal of Micromechanics and Microengineering*, 26(11), 115013.

Bartlett, N. W., Becker, K. P., & Wood, R. J. (2018). A fluidic demultiplexer for controlling large arrays of soft actuators. *In preparation.*

2

Multimaterial 3D Printing

In this chapter, we evaluate the potential of multimaterial 3D printing as a manufacturing method for building soft robots that perform morphological computation[5]. We find that although the materials available to 3D printing are severely limited in many regards, the process itself is highly capable and is a valuable strategy for fabricating soft robots that demand some degree of me-

chanical intelligence.

2.1 Motivation and goals

There were a number of motivations for the work presented in this chapter. When introducing a new fabrication strategy to the field of soft robotics, there are many potential benefits. However, we were most intrigued by three specific questions in this study.

First, there is the question of speed. Soft robots are typically very slow, as they often rely on the inflation of a bladder for actuation; locomotors in particular are notoriously leisurely. We wanted to examine the feasibility of making a mobile soft robot that could move with speed and agility. Our strategy was to use the combustion of butane and oxygen to rapidly deform the body of a soft robot, causing it to jump.

Second, there is the question of integration. Mobile soft robots (to date) are either tethered or carry rigid driving components (e.g., pump, battery, valves). For untethered systems, there is an open question of how to interface between the rigid driving components necessary for operation and the soft body of the robot. In this work, we used a multimaterial 3D printer to fabricate a modulus gradient to ease the interface between the rigid and flexible portions of our robot.

Third, there is the question of softness. As we shall see, this question will turn out to be very much related to the second question, but we wanted to ask

how soft a soft robot should be, and what value there may be in a hybrid hard-soft robot. We found that making specific portions of the robot's body rigid while keeping other portions flexible both enabled better performance and increased robustness. Achieving these two advantages simultaneously without a multimaterial 3D printer would have been extremely challenging.

2.2 Fabrication strategy

In this work, we opted for multimaterial 3D printing over the more traditional fabrication techniques used by the soft robotics community. This decision was largely informed by limitations of previous fabrication techniques.

2.2.1 Previous fabrication strategies

The 3D-printed jumping robot presented here has predecessors, both tethered[99] and untethered[110], which were fabricated using molds. The tethered system was a tripedal design fabricated from silicone elastomer that jumped by combusting a stoichiometric mixture of methane and oxygen. The untethered system was a redesign of the tethered system, scaled up to be able to incorporate the fuel and driving components onboard. The main challenges for the untethered robot were the many points of failure for the integrated electrical, chemical, pneumatic, and mechanical systems. Due to the absence of the rigid skeleton found in most rigid robots, and also to the large forces experienced during combustion, the interfaces between the various components in this jump-

ing soft robot were found to be extremely unreliable. As such, we performed a second redesign, with a particular focus on creating robust interfaces.

2.2.2 Why 3D printing?

In nature, many animals employ stiffness gradients to join rigid materials and soft structures while minimizing stress concentrations that could lead to failures at rigid/soft interfaces[90,68]. One of the reasons biological systems often outperform engineered systems is that in nature, which employs self-organization for fabrication, added structural complexity (i.e., the ratio of maximum to minimum feature size) comes at a minimal cost. Emerging digital fabrication technologies such as 3D printing are beginning to allow designers to move toward this level of structural complexity, albeit at a larger scale and with fewer materials. These technologies can be used to manufacture geometrically intricate designs as efficiently as simple designs with an equivalent amount of material.

2.3 Robot morphology

The 3D-printed jumping robot consists of two main components: the body and the core module. As shall become apparent, there is extremely close coupling between the design of the robot, its fabrication, and its actuation strategy. That is, the robot's ability to perform morphological computation is intricately linked to the capabilities and limitations inherent to the fabrication strategy.

2.3.1 Monolithic soft body

We used a multimaterial 3D printer (Connex500, Stratasys) to directly print the functional body of a robot that employs soft material components for actuation, obviating the need for complex molding techniques or assembly. The robot body is composed primarily of two nested hemispheroids.

The flexible bottom hemispheroid features a small depression that provides an initial volume into which oxygen and butane are injected. Ignition of the gases causes a volumetric expansion[99,110], launching the robot into the air (Fig. 2.1, A and B).

The top hemispheroid has a modulus of elasticity that ranges over three orders of magnitude (from approximately 1MPa to 1 GPa (Table 2.1)) through a stepwise gradient of nine different layers, creating a structure that transitions from highly flexible (rubber-like) to fully rigid (thermoplastic-like) (Fig. 2.2). In addition to providing a mechanical interface for the rigid control components, the rigid portion of the top hemispheroid also prevents undesired expansion locally and focuses the energy of combustion into the ground, enhancing the jumping efficiency.

Pneumatic legs, which use a nested hemi-ellipsoid design similar to that of the main body, surround the central explosive actuator and are used to tilt the body before a jump, controlling the direction of locomotion. This separation of power and control actuators simplifies actuation and gives greater control over the jump direction.

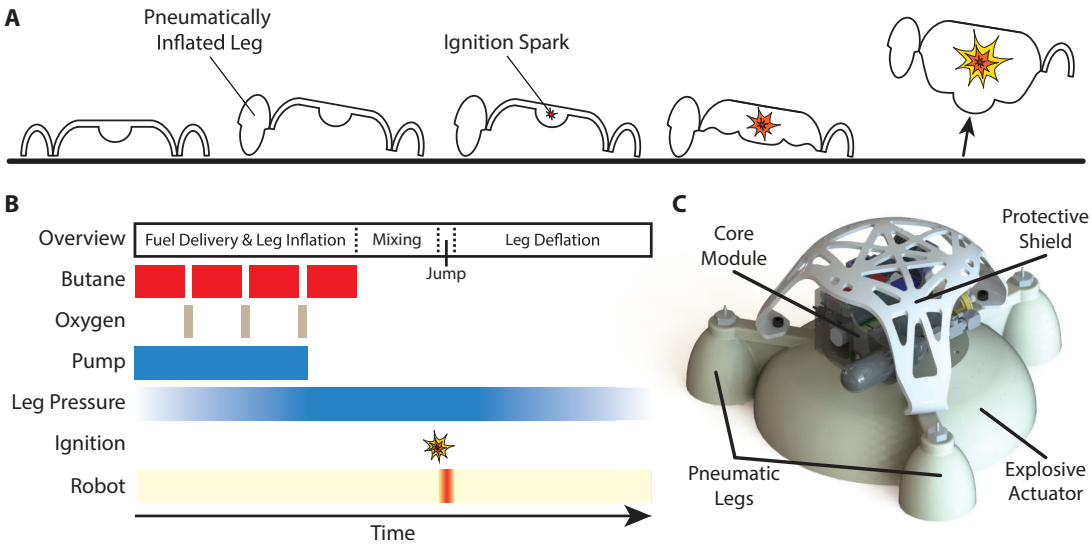

Figure 2.1: Robot design and principle of operation. (A) To initiate a jump, the robot inflates a subset of its legs to tilt the body in the intended jump direction. Upon combustion, the bottom hemispheroid balloons out, pushing against the ground and propelling the robot into the air. (B) The ignition sequence consists of fuel delivery, mixing, and sparking. Butane and oxygen are alternately delivered to the combustion chamber (to promote mixing). After a short delay to promote additional mixing of the fuels, the gaseous mixture is ignited, resulting in combustion. Leg inflation occurs concurrently with fuel delivery, and leg deflation begins shortly after landing. (C) Computer-aided design model of the entire robot, consisting of the main explosive actuator surrounded by three pneumatic legs. A rigid core module that contains power and control components sits atop the main body, protected by a semisoft shield.

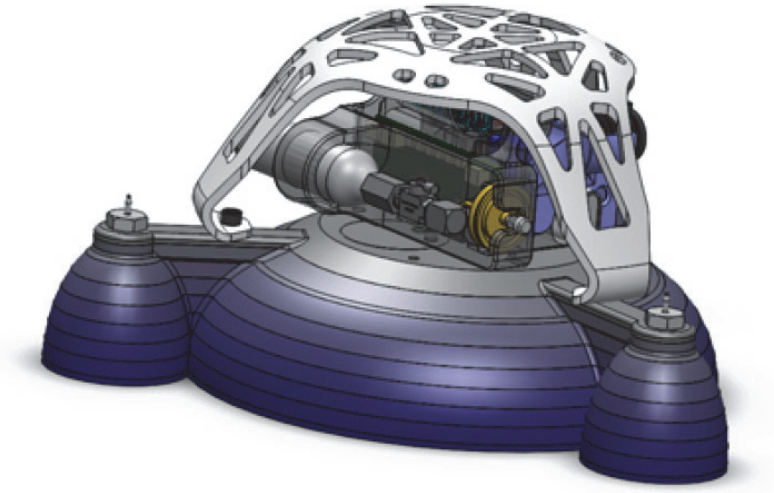

Figure 2.2: Robot material distribution. The top hemishperoid of the robot transitions from flexible (dark blue) to rigid (grey) through a stepwise gradient of nine discrete layers.

2.3.2 Core module

In order to simplify prototyping, we chose a modular design with a rigid core module containing the control components (which are expensive and change infrequently during design iteration of the body), connected through a predefined interface to the body of the robot (Fig. 2.1C). This modularity enables efficient iteration of the robot body design, as well as rapid replacement in the case of destructive testing.

The core module contains a custom circuit board, high-voltage power source, battery, miniature air compressor, butane fuel cell, bank of six solenoid valves, oxygen cartridge, pressure regulator, and an internal network of channels to facilitate interfacing between the components as necessary (Fig. 2.3). The core module is mechanically attached to the rigid portion of the body with a layer

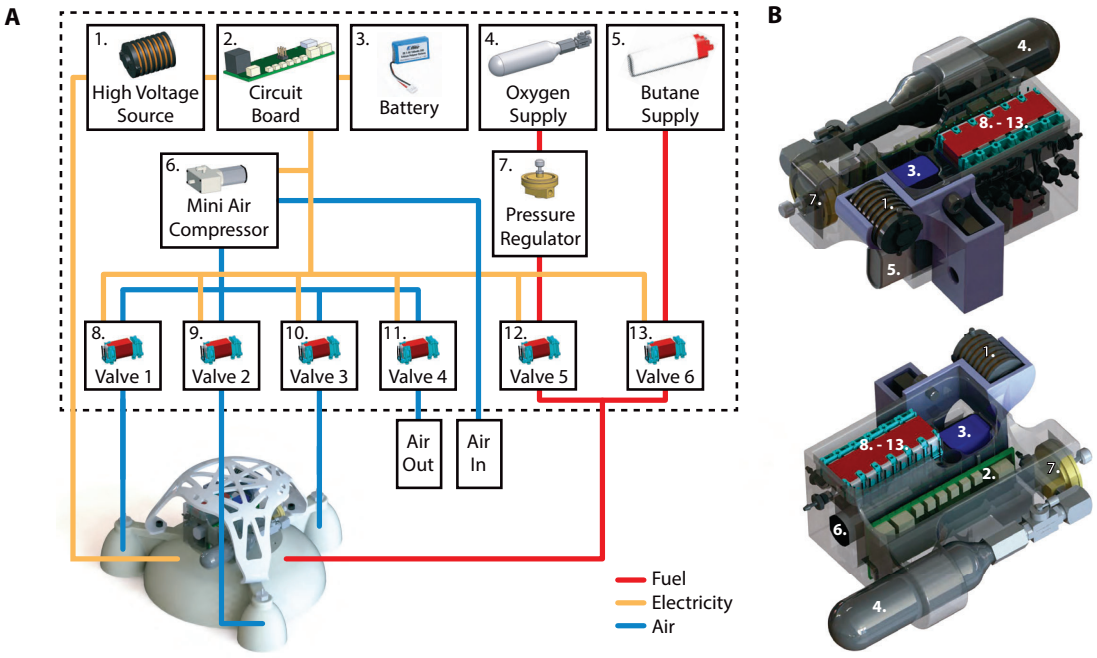

Figure 2.3: Driving components and core module. (A) Functional dependencies of the control hardware. (B) CAD model of the core module with components from (A) labeled.

of high-strength mushroom-head fasteners. Otherwise, it interfaces with the body only through four tubes (three pneumatic tubes for the legs and one tube for fuel delivery to the combustion chamber) and two wires (which produce the spark in the combustion chamber).

2.4 Actuation strategy

As stated in the introduction to this chapter, one of the motivations for this work was to create a robot that could locomote rapidly. We opted to employ combustion-based jumping to accomplish this goal. Furthermore, we saw this actuation strategy as a way to demonstrate the robustness of our fabrication

method, as combustion is a rather violent event that puts significant stresses on the body of the robot.

2.4.1 Thermodynamic model

In this section we present a thermodynamic model of a combustion-powered jump of our soft robot. This model is based on the Otto cycle (the idealized thermodynamic cycle used to model internal combustion engines). Although the ideal Otto cycle assumes a rigid volume (as is found in an internal combustion engine), it serves as a first approximation for a soft system. The timescale of the explosive phase is assumed to be sufficiently short that material strain can be neglected.

The Otto cycle (Fig. 2.4) consists of a number of processes. From ignition (1) to the end of combustion (2), there is a phase of constant volume heat addition. After all the heat from combustion has been absorbed by the working fluid, the cycle moves into isentropic expansion. The volume expands until limited by the geometry of the system (3), after which there is a phase of constant volume heat rejection, followed by isentropic contraction back to the original state.

Assuming atmospheric conditions (temperature and pressure) at ignition, we calculated the temperature at the end of combustion (T_2) using the heat of combustion of butane ($\Delta H^{\circ}_{C,butane}$), the specific heat of oxygen ($c_{v,oxygen}$), and the masses of butane (m_{butane}) and oxygen (m_{oxygen}) employed in our robot:

$$T_2 - T_1 = \frac{\Delta H^{\circ}_{C,butane}\, m_{butane}}{c_{v,oxygen}\, m_{oxygen}} \tag{2.1}$$

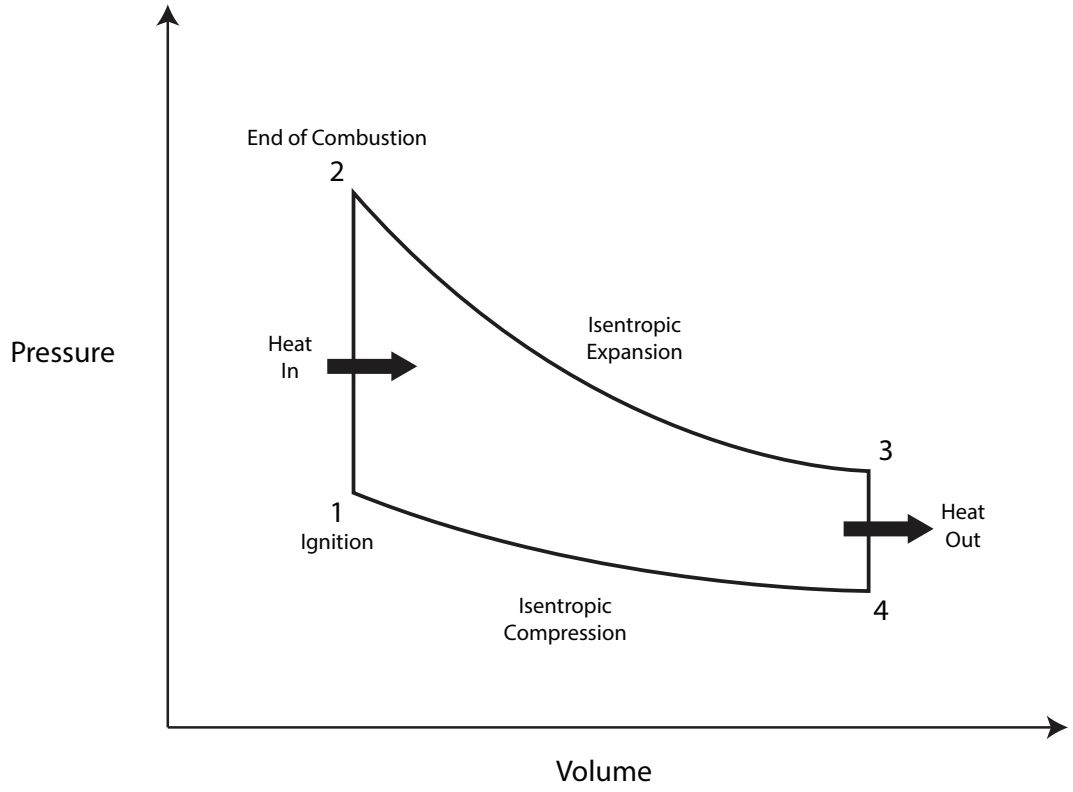

Figure 2.4: A depiction of the idealized Otto Cycle. After ignition (1), there is a phase of constant volume heat addition, until the end of combustion (2). Isentropic expansion occurs until the final volume is reached (3), and then there is a phase of constant volume heat rejection, until isentropic compression begins (4).

However, one should note that stoichiometric considerations necessitate a fixed ratio of oxygen to butane, so the amount of oxygen is in fact a function of the amount of butane (both of which are constrained by the geometry of the robot):

$$m_{oxygen} = m_{butane} \frac{M(O_2)}{M(C_4H_{10})} \gamma \tag{2.2}$$

Here, $M(O_2)$ and $M(C_4H_{10})$ are the molar masses of oxygen and butane (re-

spectively), and γ is the stoichiometric ratio of oxygen to butane (in our case γ = 6.5 (Eq. 2.5)). Thus, the temperature at the end of combustion is not a function of the amount of butane used for a jump; once the geometry of the robot is defined, an ideal amount of fuel is specified (based on the initial volume and the ideal fuel ratio), which determines the jump height. This relationship should therefore be taken into consideration at design time to identify the ideal ratio of initial to final explosive actuator volume to achieve a jump of a desired height. However, since the overall mass of the system is also a function of this volume ratio, it may be necessary to solve the design problem iteratively.

Knowing the temperature at the end of combustion, the ideal gas law is used (in conjunction with the fact that the volume has not changed) to find the pressure $P2$:

$$P_2 = P_1 \frac{T_2}{T_1} \tag{2.3}$$

The isentropic relation (Eq. 2.4), where V_2/V_3 is the ratio of the volumes before and after isentropic expansion, and k is the ratio of specific heats, determines the curve from the end of combustion to the final volume.

$$\frac{P_3}{P_2} = \left(\frac{V_2}{V_3}\right)^k \tag{2.4}$$

Finally, the cycle ends with the system transferring any remaining heat from combustion to the environment at atmospheric pressure.

2.4.2 Stoichiometry and experimental validation of fuel ratio

The stoichiometry of butane combustion (Eq. 2.5) requires an oxidative environment with a precise ratio of butane and oxygen for ignition. Based on Eq. 2.5, the ideal stoichiometric ratio of pure oxygen to butane is 6.5, which translates to an ideal volumetric ratio of approximately 6.2.

$$2C_4H_{10(g)} + 13O_{2(g)} \rightarrow 8CO_{2(g)} + 10H_2O_{(l)} + 2.9\,MJ/mol \tag{2.5}$$

In the baseline testing condition, 50 mL of oxygen was used for each of two jumps. The oxygen cartridge we used had an internal volume of 20 mL and was pressurized to 90 psi, giving an initial volume of oxygen (at STP) of 122 mL. Thus, there should have been 22 mL left after two jumps. Measurement of the remaining oxygen showed that 14.5 ± 4.2 mL (N=6) was left. The discrepancy (7.5 mL) is likely due to inaccuracies in determining the exact valve timing and imperfections in the press fits of the tubing, valves, and connectors.

The supply pressure effect was certainly a factor, as the pressure of the oxygen cartridge changed significantly from the first jump to the second. We accounted for this fact by using different valve timing on the first and second jumps. The correct timing was determined experimentally by (1) filling an oxygen cartridge to standard experimental conditions, (2) opening the valve and noting the time required to deliver 50 mL oxygen, then closing the valve, and (3) reopening the valve a second time to deliver the same amount of oxygen, again noting the (new) time. We found that after filling to 90 psi, a standard

16g CO_2 cartridge would deliver 50 mL of oxygen in 1.95 seconds. The now lower pressure cartridge would deliver the same volume of oxygen (50 mL) in 1.50 seconds upon opening the valve a second time.

Fuel measurements were taken periodically over months of testing, during which conditions (e.g. ambient temperature, humidity, etc.) varied. As discussed previously, the flow rate of oxygen was variable, and so fuel delivery was determined by experimenting with valve timing. For an oxygen cartridge filled to 90 psi, opening the valve for 1.95 seconds delivered 56.3 $\pm$5.8 mL (N = 15). The second valve opening of 1.50 seconds delivered 47.5 $\pm$ 2.7 mL (N = 6). The flow rate of butane was notoriously variable, depending on how much liquid butane was in the container, the orientation of the container, and how forcefully it was press fit into the core module (Fig. 2.3). After a procedure that produced somewhat reliable results was established, we determined a flow rate of 1.1 $\pm$ 0.4 mL/s (N = 21) for the butane.

2.5 Materials

The behavior of the 3D-printed materials from which we fabricated the robot were of critical importance to the performance of the robot. As such, we performed exhaustive mechanical testing to quantify key material properties. These material properties were then used as input parameters to simulations that would inform design decisions, yielding a robot with better performance.

2.5.1 Mechanical testing

The Stratasys website provided general information regarding the 3D-printed material used in this project (specifically, the "PolyJet Materials Data Sheet" and the "Digital Materials Data Sheet"). Published data sheets indicate that the materials used in the robot ranged in hardness from Shore A 27 to Shore D 83. We performed additional analysis of the 3D printed material through different tests on a universal testing machine (Instron 5544, Instron). Cyclic testing indicated that at high rates of extension, significant hysteresis was present due to the viscoelastic properties of the 3D printed material. However, at rates below 0.03125 mm/s, all viscous effects were negligible and the material behaved elastically. Each of the nine different materials used in the stiffness gradient was tested in a standard tensile test (ASTM D 638, Type IV), performed at 0.03125 mm/s to eliminate any rate dependent behavior. From this test, we obtained values for the shear and Young's moduli of each material, which were subsequently used in the simulations. The material properties can be found in Table 2.1.

We conducted additional extension tests on samples that featured either an abrupt transition from the softest to the most rigid material or a more gradual step-wise transition by incorporating materials of intermediate moduli. In fatigue tests in which we repeatedly stretched the samples to an extension of 5 mm (20% of the test section) at 0.03125 mm/s, the discrete samples failed after an average of 436 cycles, whereas the gradient samples lasted an order of magni-

Material	Young's Modulus (MPa)
1	1012.5
2	802.90
3	58.462
4	52.641
5	15.309
6	6.767
7	2.698
8	1.166
9	0.439

Table 2.1: Young's moduli of the materials in the gradient. The materials used were digital combinations of commercial 3D printing materials offered by Stratasys, specifically VeroWhitePlus RGD835 (rigid) and TangoPlus FLX930 (flexible). Detailed information on these materials may be found on the Stratasys website.

tude longer (most samples were discontinued after 24 hours of testing, over 8640 cycles).

2.5.2 Numerical modeling of materials

The mechanical testing information was used to simulate the operation of the robot using finite element analysis (FEA) software, which allowed us to compare the relative efficiency of jumping robots with different material distributions.

Non-linear finite element analysis was performed using the commercial package Abaqus/Explicit (v6.12) (Abaqus Unified FEA, Dassault Systemes). All materials were modeled using a Neo-Hookean material model, each with a specific initial shear modulus. The shear moduli were determined experimentally by performing uniaxial tension tests and fitting the stress-strain curves using a least squares approximation.

To qualitatively show the effect of using materials with different moduli in

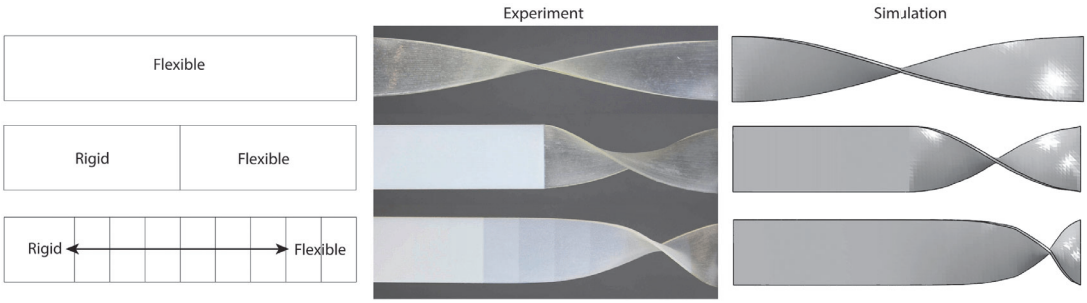

Figure 2.5: Material analysis. Qualitative twisting analysis comparing 3D-printed beams that are fully flexible (top), half rigid and half flexible (middle), or transition gradually from rigid to flexible (bottom). These tests were performed to gain an understanding of how these materials respond, as well as to validate the numerical values of the material properties used in simulation. (Left) Material distribution of the beams. (Middle) Beams under torsion. (Right) Simulation of beams under torsion.

the same structure, we deformed three beams with a different material distribution by twisting them 180 degrees. These beams were modeled using approximately 10,000 tetrahedral elements (Abaqus element code C3D4), and quasi-static conditions were assured by using a relatively long simulation time, as well as a small damping factor (Fig. 2.5). Further simulations allowed us to examine the differences in stress concentrations as a function of material distribution (Fig 2.6). The results from these studies revealed that, when compared to an abrupt material transition, the incorporation of a graded interface could achieve a 30% reduction in maximum stress upon tensile loading, reaching a value comparable to the maximum stress observed in a soft, single-material model.

2.5.3 Simulations of jump and impact

Although a perfectly smooth gradient from rigid to flexible would have been ideal, the capability of the fabrication technique was limited to a stepwise gra-

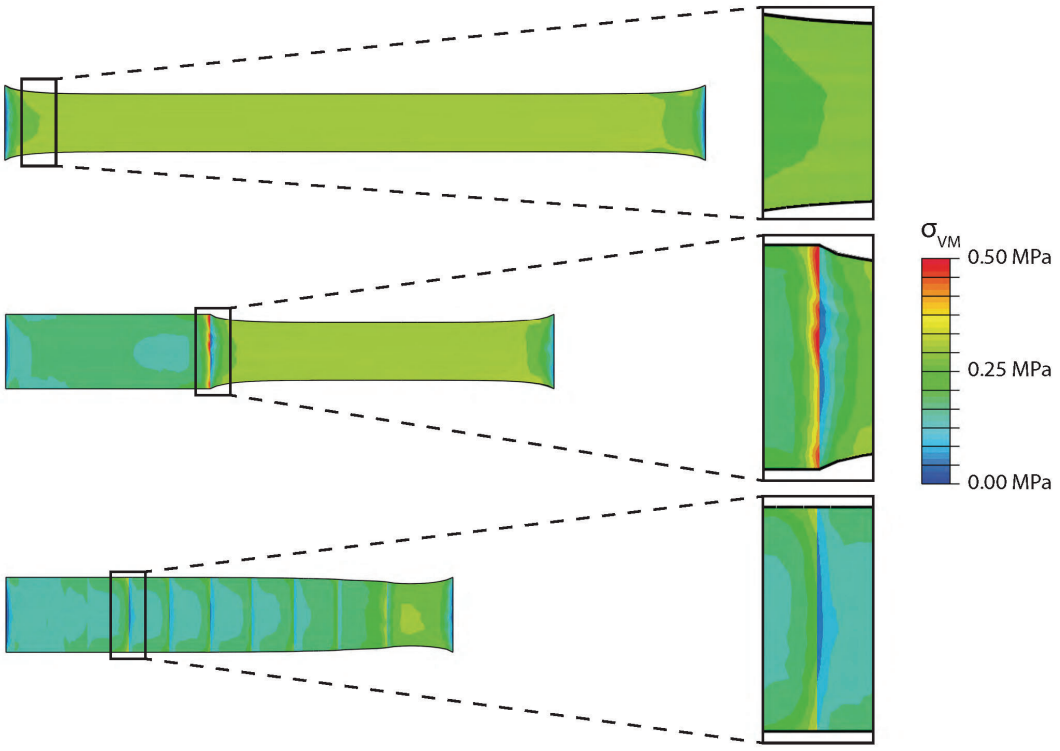

Figure 2.6: Simulations of beams in tension. Simulations of beams in tension that are fully flexible (top), half rigid and half flexible (middle), and transition gradually from rigid to flexible (bottom). The maximum stresses in each of these beams are 0.35 MPa, 0.54 MPa, and 0.37 MPa, respectively. Compared to the half rigid and half flexible beam, the fully flexible and gradient beams experience maximum stresses of 64.8% and 68.5%, respectively. Simulations were done with (undeformed) beam dimensions of 25.4 mm x 152.4 mm x 1.0 mm. Enlarged images of the points of stress concentration are shown to the right of each beam. Additional motivation for the use of a gradient was derived from considerations of the effect of stress concentrations on interfacial failure in multi-material systems, a problem that is well established in the mechanics literature.

dient of at most nine materials. The actuation strategy necessitated a flexible bottom hemispheroid, whereas the off-the-shelf control components required a rigid housing; however, the stiffness distribution of the top hemispheroid was unconstrained.

Thus, to determine how the material properties of the top hemispheroid would affect jumping, we simulated three cases: (i) a flexible top with a small rigid portion to mount control hardware, (ii) a top featuring a stiffness gradient from fully flexible to fully rigid, and (iii) a fully rigid top (Fig. 2.7A). Simulations showed that the flexible top was inefficient at directing the energy of combustion into the ground and propelling the robot, suggesting weak jump performance. As expected, the simulated rigid top robot produced the highest ground reaction force, whereas the gradient top robot exhibited a performance between the two extremes.

We carried out additional simulations to investigate the behavior of the three designs during the impact of landing (Fig. 2.7B). The results indicate that the rigid top robot experiences a given reaction force (50 N) at a much smaller deformation than either the gradient or flexible top robots. Immediately upon impact, the rigid top robot experiences an abrupt increase in force, whereas the gradient top robot experiences a more moderate increase. The flexible top robot sees almost no increase, until the small rigid portion strikes the ground, initiating a rapid increase akin to that of the rigid top robot. Integrating the force-displacement curves (up to 50 N), we find that the rigid and flexible top robots only absorb 13 and 73% (respectively) of the impact energy that the gradient

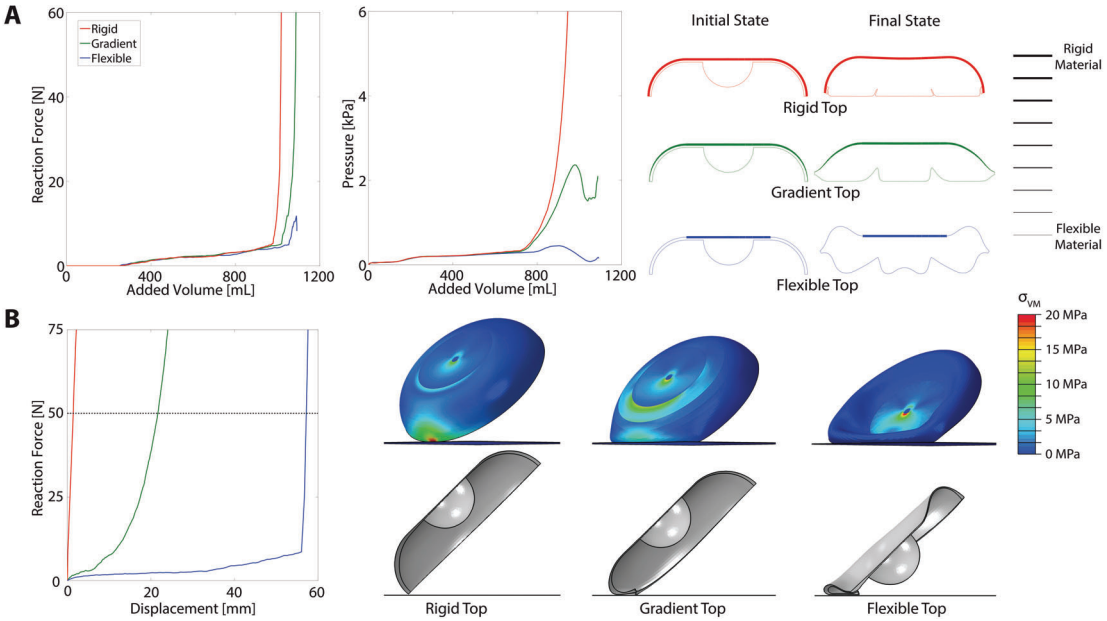

Figure 2.7: Jumping and impact simulations. (A) Jumping simulation. (Left) Ground reaction force as internal gases expand. (Middle) Pressure evolution inside the robot body as internal gases expand. (Right) Deformation state of rigid top, gradient top, and flexible top robot bodies at the initial state and the point of maximum simulated gas expansion. Line thicknesses indicate material stiffness. (B) Impact simulation. In the simulation, the robot strikes the ground at $45°$. This angle was chosen as a particularly extreme loading condition and because it correlated with observations from jumping experiments. (Left) Reaction forces experienced by the three robots upon striking a solid plane under simulated conditions representative of actual testing conditions. (Right) FEA results of rigid top, gradient top, and flexible top robots, compared at 50 N.

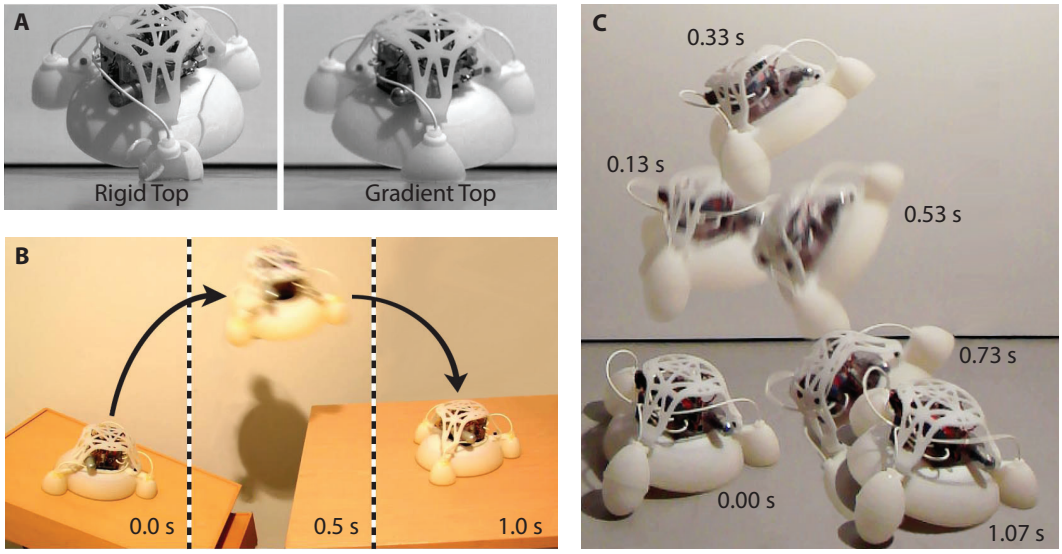

Figure 2.8: Experimental testing results. (A) Comparison of impact behavior shortly after the moment of ground contact. Identical testing conditions were used to analyze the difference in landing between a robot with a rigid top and one with a gradient top. Because the rigid top robot jumped higher under combustion-powered testing, the gradient top robot was dropped from the maximum height achieved by the rigid top robot for a direct comparison. (Left) The rigid top robot fractures upon impact. (Right) The gradient top robot is able to absorb the impact and survive the fall. (B) The robot performs a targeted jump off of an angled surface onto a table. (Left) As the robot prepares for the jump, oxygen and butane are delivered into the combustion chamber. (Middle) Upon ignition of the fuel, the robot is propelled into the air. (Right) After jumping across a gap, the robot lands on a table. (C) A sequence of images showing a directional jump. The robot pitches backward during the jump, providing a soft landing on the inflated legs. Upon impact with the ground, the robot pitches forward and returns to its pre-jump stance.

top robot absorbs. The increased energy absorbed by the gradient top robot during impact suggests that it will be most successful at distributing the impulse over a longer duration, therefore reducing peak stresses and providing the least violent landing.

2.6 Experimental results

By 3D-printing different test cases, we experimentally verified these simulation results. A jumping robot with a completely rigid top was able to jump 1.12 m untethered using 40 mL of butane and 120 mL of oxygen. Identical testing conditions on a gradient top robot produced a jump of 0.25 m. A flexible top robot was deemed impractical to print because of the predictions from FEA. As predicted by the simulations, the gradient top robot was less efficient at jumping. However, the gradient top robot was better able to withstand the impact of landing (Fig. 2.8A).

In one test, the body of the rigid top robot shattered upon landing, surviving a total of just five jumps; the gradient top robot survived more than twice that number of jumps and remained operational. Other nearly identical gradient top robots survived over 100 jumps (in 81% of these tests, we removed the core module from the body and delivered the combustion products and ignition sparks through a tether to simplify testing, reducing the system mass to about 50% that of the untethered system).

To provide a direct comparison in landing behavior, the gradient top robot was additionally dropped from the maximum height achieved by the rigid top robot and successfully survived 35 falls. The robot was dropped from numerous orientations to mimic the variability in landing. The stiffness gradient provides the necessary rigidity to transfer the impulse of combustion to generate effective jumping, and the compliance of the base absorbs and dissipates the energy of

the landing impact. Unlike the rigid top robot, in which structural failure was catastrophic, the failure mode of the gradient top robot on the 36th fall was a cracking of one of the legs, which is easily repairable with a urethane adhesive. By trading the jumping efficiency of the rigid robot for an improved ability to survive landings, the gradient top robot demonstrated a greater overall robustness.

Further testing on the gradient top robot showed high resilience and good performance (Fig. 2.8B). This robot autonomously jumped up to 0.76 m (six body heights) high and demonstrated directional jumping of up to 0.15m (0.5 body lengths, 20% of jump height) laterally per jump (Fig. 2.8C). Unlike previous combustion-powered soft jumpers that were either tethered[99] or achieved only a few untethered jumps due to inconsistent connection of electrical and mechanical components at the interface of the rigid and soft components[110], this design allowed for many successful jumps with a single soft robot (21 untethered jumps and 89 tethered jumps).

In tethered experiments on the gradient top robot (in which the control hardware was off-board and thus the robot was significantly lighter), the robot attained its highest jump of 2.35 m using 50 mL of butane and 120 mL of oxygen. With a body mass of 478.6 g, this jump corresponds to an efficiency of 0.18% (+0.11%, -0.05%). The most efficient jump was a tethered test that reached 1.60 m using 24 mL of butane and 50 mL of oxygen, corresponding to an efficiency of 0.26% (+0.15%, -0.07%). For the untethered system, a robot with a total mass of 964.6 grams jumped 0.76 m using 24 mL of butane and 50 mL of

oxygen, corresponding to an efficiency of 0.25% (+0.14%, -0.07%). The amounts of oxygen and butane used for the maximum height jump and most efficient jump did not correspond to calculated stoichiometric ratios. However, given that fuel delivery was quantified by valve timing, the exact amount of butane or oxygen delivered was unable to be precisely determined. In addition, we did not actively remove the preexisting air from the system, meaning that some amount of air was present in the combustion chamber in addition to the delivered amounts of oxygen and butane. Another source of error was the possibility that some of the butane was being absorbed into the walls of the combustion chamber.

Using smaller volumes of butane and oxygen, we were able to achieve multiple successive jumps in the tethered gradient top system. We demonstrated multiple jumps of differing heights (1.00 m jump followed by 0.30 m jump), as well as multiple jumps of roughly the same height (0.15 m and 0.15 m, also 0.50 m and 0.30 m).

As oxygen was the limiting fuel source, additional jumps could have been achieved by increasing the pressure of the stored oxygen. The pressure canister we used had an internal volume of 20 mL and was rated to contain pressures up to 6.2 MPa (900 psi). At this pressure, the canister could hold 1.62 g of oxygen, which is equivalent to 1.22 L at room temperature (20°C) and atmospheric pressure. This amount of oxygen is enough for 32 consecutive jumps. A full butane fuel cell holds 3.3 g of butane, or 1.38 L of gaseous butane at room temperature and atmospheric pressure, or enough for 57 jumps. Thus, oxygen was the

limiting fuel. For safety reasons, we used oxygen pressurized to only 90 psi and replaced the oxygen supply after two jumps.

The bodies were extremely robust, surviving dozens of jumps before they became unusable. The monolithic design has no sliding parts or traditional joints that can be fouled or obstructed by debris or rough terrain, and the nested design requires minimal deformation for actuation. As with previous jumping soft robots powered by combustion[99,110,57], and untethered systems exposed to direct flames[112], we did not observe significant damage to the soft (or rigid) body materials due to the brief exposure to elevated combustion temperatures and flames.

2.7 Conclusions

The fabrication of soft robots using multimaterial 3D printing has numerous advantages over traditional molding techniques. This strategy promotes high-throughput prototyping by enabling rapid design iteration with no additional cost for increased morphological complexity. By allowing designers greater freedom, 3D printing also facilitates the implementation of good robotic design principles, such as modularity and the separation of power and control actuators.

Beyond soft robotics specifically, the ability to print a single structure composed of multiple materials enables investigation into mechanically complex designs, without the drawbacks of complicated assembly or inconsistent man-

Figure 2.9: The fabrication strategy employed in this work enabled a robot capable of operating in diverse environments, such as dirt (left), grass, and rocks (right).

ufacturing repeatability[114]. One such design is a modulus gradient that eases the transition from soft to rigid components through stress reduction at the interface of materials mismatched in compliance. Although the materials available to this fabrication strategy are currently limited and perhaps best suited to the fabrication of prototype devices, future development of materials compatible with 3D printing will only enhance the relevance of this approach.

3

Precision Micromachining for Multilayer Soft Lithography

In this chapter, we examine a process that combines multilayer soft lithography, precision laser micromachining, and folding to establish a new paradigm for creating 3D soft microstructures and devices[88]. We exploit phase-changing

materials to transform actuators into structural elements, thereby allowing two-dimensional laminates to evolve into a third spatial dimension. To illustrate the capabilities of this new fabrication paradigm, we designed and manufactured the first MORPH (Microfluidic Origami for Reconfigurable Pneumatic/Hydraulic) device: a 12 layer soft robotic peacock spider with embedded microfluidic circuitry and actuatable features.

3.1 Fabricating for complexity

The behavior, and in particular the motion, of soft devices is fundamentally dictated by the geometry and properties of the constituent materials; consequently, manufacturing techniques play a central role in the resulting function and must be considered throughout the design process.

3.1.1 Brief survey of fabrication techniques for soft robotics

Molding is one of the most common techniques for manufacturing soft devices on the centimeter scale[69]. However, at smaller scales, the structural complexity that can be obtained is limited by the manufacturability of the mold, thus restricting the design mostly to single degree of freedom continuum bending structures[26]. 3D printing allows nearly arbitrary geometries[116], yet the paucity of compatible soft materials and limited resolution engenders mostly static devices below the mesoscale. 4D printing has been proposed to develop dynamically evolving structures that exploit the time-dependent, shape-shifting properties of

some 3D printed, stimuli-responsive materials[106]. While the possibility of printing structures that can evolve in time is certainly intriguing, 4D printing suffers from a lack of compatible materials to an even greater extent than 3D printing.

Planar manufacturing processes have also been used for fabricating soft devices across different scales, from meter sized soft robots[111], to millimeter scale soft microdevices[93]. Among planar processes, soft lithography enables dense packing of extremely fine features, leading to devices capable of (fluidic) computation, as widely demonstrated in the field of microfluidics[86]. However, with no means of altering the overall profile or shape, joints are undefinable and large motions are unattainable, relegating most soft lithographic devices to a purely two-dimensional existence. To obviate these limitations, researchers have proposed ways of fabricating 3D microfluidic devices to create 3D networks[108,131,8] and self-assembling structures[35]. A number of manufacturing methods for developing innovative soft microdevices have also been proposed, such as hydrogel-based micropatterning[45], electrically assisted ionoprinting[75], and the synthesis of materials responsive to light[91], temperature, and magnetic fields[10] for drug delivery systems.

3.1.2 Structural vs. functional complexity

Although the aforementioned techniques have enabled the fabrication of interesting examples of soft micro- and macro-systems, we believe that the potential of soft functional devices has not yet been fully explored, especially at the meso- and micro-scale, where fabrication of complex soft functional structures

still presents technological challenges.

To clarify this concept, we can observe that complexity in current soft microstructures can take many forms: microfluidic devices may embody logic circuits[86], soft microstructures may demonstrate intricate geometry[56,135], and soft microactuators may employ exotic materials and respond to diverse stimuli[29]. Here we propose a distinction between structural and functional complexity. We define "structural complexity" in terms of characteristics of the static system, such as the spatial dimensionality (i.e., whether 2D or 3D), the number and diversity of materials involved, and geometric considerations (e.g., shape and minimum feature size). "Functional complexity" encompasses the dynamic aspects of the system, such as the number of degrees of freedom, the achievable motions and deformations, and any embodied computation or intelligence.

There are very few examples of soft microstructures that combine both structural and functional complexity. One example, the Octobot[127], is a two degree of freedom autonomous soft robot fabricated by exploiting a multi-step process combining embedded 3D printing (EMB3D) and soft lithography. The EMB3D technique relies on printing functional and sacrificial inks inside an uncured matrix. The possible geometries available to this technique present great opportunities, but are limited to form factors reachable with a printing tip (i.e., about 75 μm).

3.1.3 A new manufacturing paradigm

As the Octobot example illustrates, the functional complexity of soft microstructures is limited largely by the chosen fabrication methodology. As in biology, the notion of a structure-function relationship is present in engineered devices, with structure being defined during fabrication. A new class of soft microstructures that demonstrate mature functional complexity necessitates an innovative manufacturing paradigm; to achieve this goal we propose a hybrid technique that involves soft lithography to create multilayer interconnected microfluidic networks, bulk micromachining to form distinct layer geometries, a method to vary the bending plane of fluidic microactuators fabricated using a two-dimensional process, and the ability to form stable 3D structures from 2D composites by *in situ* curing of polymers within the microfluidic network.

3.1.4 Overview of fabrication workflow

Previous work has demonstrated the possibility of exploiting laser cutting to release simple soft microactuators from an elastomeric matrix[95], while templateless prototyping of polydimethylsiloxane microfluidic structures exploiting laser machining has also been proposed[54]. Here, we use lithographic techniques to manufacture elastomeric layers with embossed features that we then further modify by means of laser micromachining. After precision alignment and bonding of individual layers, the result is a soft laminate with embedded microfluidic circuitry and a nearly arbitrarily complex profile. An overview of this process

can be seen in Fig. 3.1.

The process begins with the manufacture of a patterned elastomeric layer via conventional soft lithography. This layer is then transferred to a flexible yet inextensible substrate that is used as a carrier for further processing steps (Fig. 3.1A). A thin polymeric film is placed on top of the layer to keep it clean during handling and subsequent cutting steps. The carrier is placed into a precision laser micromachining system and, after alignment to fiducials defined during soft lithography, the elastomer is cut according to a secondary pattern (Fig. 3.1B). In this phase, we cut only the elastomer and not the carrier using a laser power of 0.7 W and focusing the laser on the top surface of the soft layer. The laser then cuts holes in the carrier that are to be used for future pin alignment. In order to do this, we focus the laser on the carrier and increase the laser power to 1.2 W. This process is repeated for all layers to be used in the final structure. Adjacent layers are then joined using surface functionalization techniques (in this work we use oxygen plasma treatment) and precision pin alignment (Fig. 3.1C). Selective bonding of consecutive layers can be achieved using masking procedures during the functionalization phase. In this way, we create multilayer laminate devices with embedded features (defined via soft lithography) and arbitrary perimeter geometries (defined via laser micromachining).

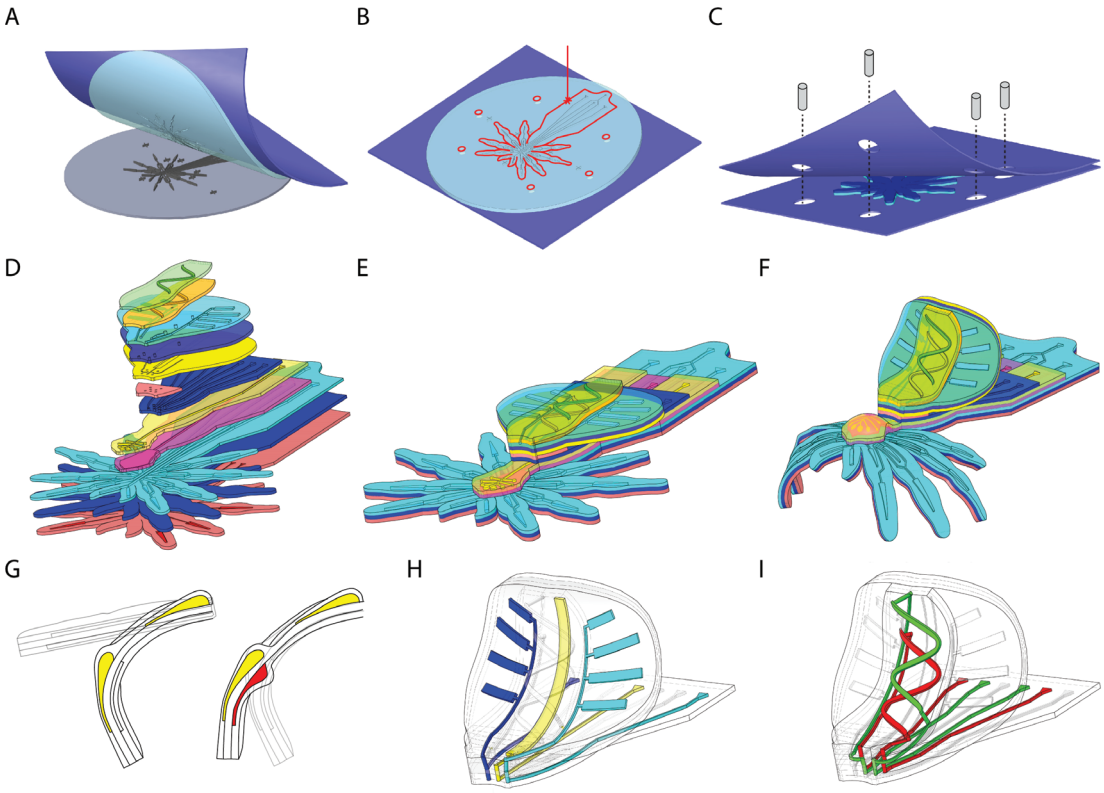

Figure 3.1: Overview of the fabrication process underlying the MORPH concept. A) Peeling a soft layer spin-coated and cured on an SU-8 patterned wafer using an adhesive substrate. B) Alignment on top of the embossed features on the soft layer and laser cutting of the soft layer and associated alignment holes. C) Aligned bonding of multiple layers through surface modifications with oxygen plasma treatment; after bonding the adhesive substrate can be peeled off to allow subsequent bonding of additional layers. D) Overview of the 12 layers composing the soft spider. E) Soft spider after bonding. F) Generation of the 3D structure through injection-induced self-folding. G) Leg design: left, shape generated due to the injection of the structural degrees of freedom (yellow); right, subsequent injection of the actuation degree of freedom (red) to antagonistically move the joint created by the structural degree of freedom. H) Actuation degrees of freedom in the abdomen sublaminate. I) Microfluidic circuit in the abdomen sublaminate, and the path of the fluid across the multiple layers.

3.2 Actuator design

In this section we investigate the effect of actuator geometry, both internal (as determined by the soft lithography process) as well as the external (as determined by the laser micromachining process). We also analyze the tolerances of our manufacturing method in terms of minimum achievable cut distance due to thermal effects generated during laser machining.

3.2.1 Effect of internal geometry

In the proposed MORPH system, we designed two types of soft microactuators: continuous bending actuators (CBAs), and discrete bending actuators (DBAs) (Fig. 3.2). CBAs have a rectangular chamber; upon pressurization the loading profile along the x-axis will be uniform, leading to a continuous bend (Fig. 3.2a). In order to obtain a discrete, joint–like bend, we designed trapezoidal chambers. In this case, upon pressurizations, the load distribution will resemble the profile shown in Fig. 3.2b. If we assume a uniform pressure distribution within the chamber, there will be a force concentration at the proximal end of the actuator chamber. The result is an anisotropic deformation of the actuator, causing a discrete, joint–like bend (Fig. 3.2b).

3.2.2 Effect of external geometry

We investigated the possibility of using the laser path to define the motion of actuatable sections of the structure, creating a previously unreported mode

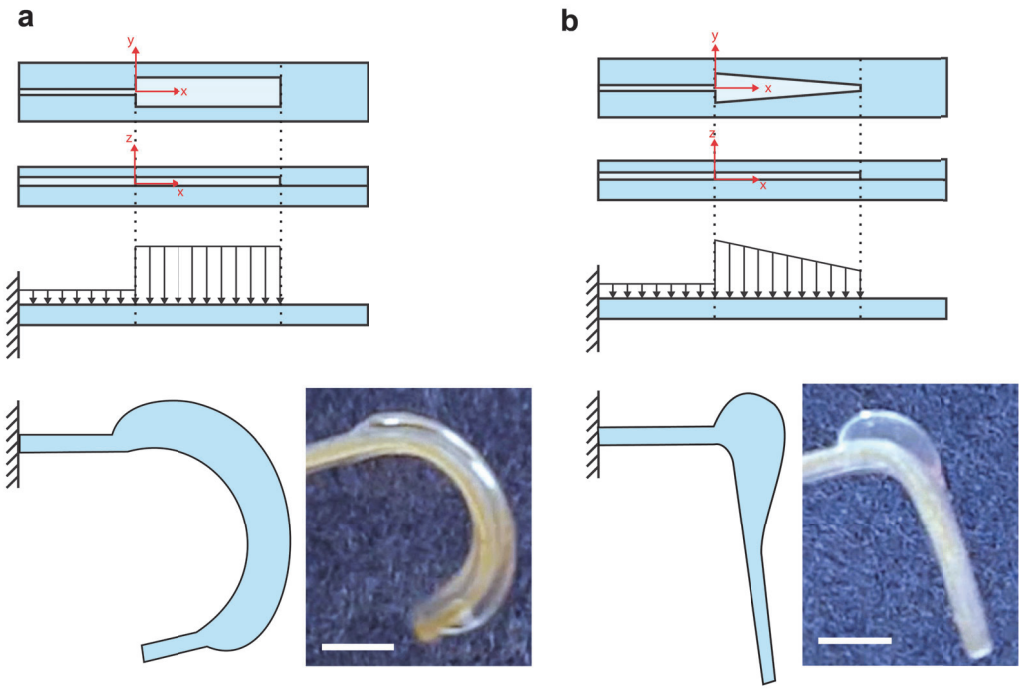

Figure 3.2: Continuous bending actuators (CBAs) and discrete bending actuators (DBAs). a) Top and side views of a CBA, loading profile, and drawing of the deformed state compared with an actual prototype. b) Top and side view of a DBA, loading profile, drawing of the deformed shape compared with an actual prototype. Scale bar is 1 mm.

of actuation for elastomeric structures. The motion of a typical bending actuator is defined by the relative bending stiffnesses of the portions of the actuator above and below the neutral axis. Referring to Fig. 3.3A, and noting that the actuators in this case are monolithic (i.e., all of the same material, and thus all of the same elastic modulus), we see that the bending motion is defined by the relative thicknesses of the material above and below the internal chamber.

As the membrane thickness m is the smallest dimension (i.e., smaller than the adjacent wall thickness d), a typical actuator will bend about the y-axis. We denote this motion as "out-of-plane bending", as the actuator bends out of the plane of its defining geometry. This behavior remains dominant until the minimum cut distance d becomes similar in magnitude to the membrane thickness m. When $d \approx m$, the bending axis begins to rotate, as m is no longer the actuator's smallest dimension. Further decreasing the minimum cut distance below the membrane thickness causes the bending axis to rotate further, until d is appreciably smaller than m and the bending axis is fully about the z-axis (normal to the plane defining the actuator geometry). We call this type of motion "in-plane bending", as the bending deformation is entirely within the plane of the actuator.

To quantify this behavior, we performed visual tracking of multiple actuators with varying minimum cut distance. Fig. 3.3B shows that indeed there is a transition from out-of-plane bending to in-plane bending as the minimum cut distance approaches and subsequently passes below the membrane thickness. Thus, we are able to program 3D actuator motion simply by choice of the 2D

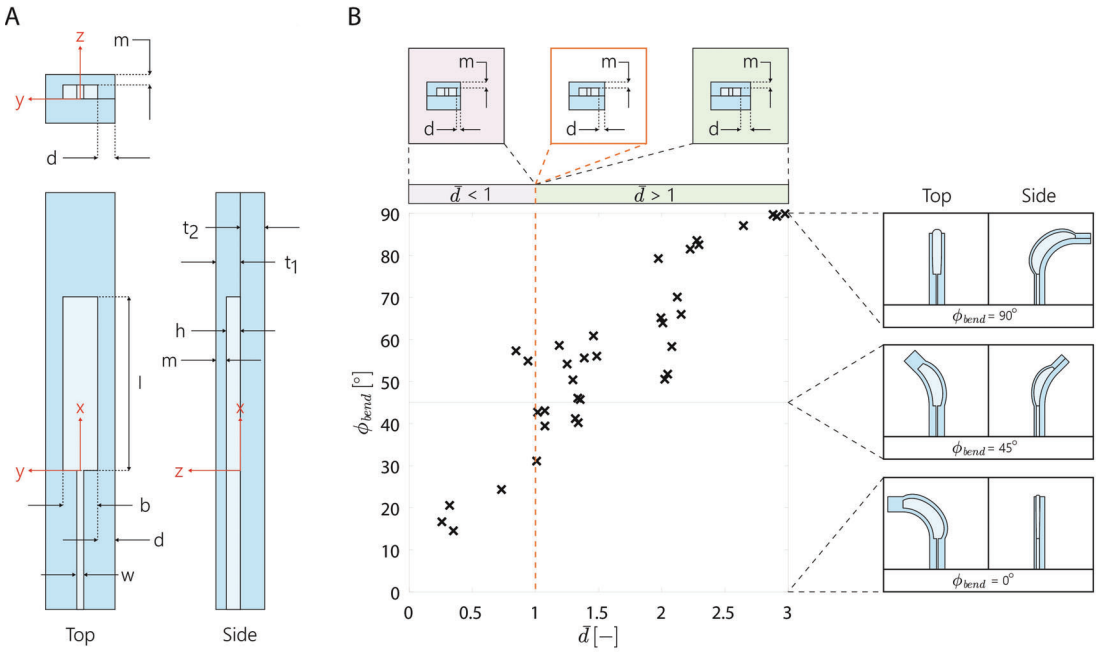

Figure 3.3: Defining actuator motion with precision laser micromachining. A) Definitions of actuator coordinate system and variables from multiple views. B) Plot of bend angle as a function of normalized cut distance, $\bar{d}$ ($\bar{d} = d/m$); the final bend angle is defined as the inverse tangent of the deflection along the *z*-axis with respect to deflection along the *y*-axis. Schematics of complete out-of-plane bending ($\phi_{bend} = 90°$), hybrid bending (e.g. $\phi_{bend} = 45°$), and complete in-plane bending ($\phi_{bend} = 0°$) are given to the right. Above the plot is a schematic detailing the various regimes of $\bar{d}$.

layer geometries.

3.2.3 Experimental setup and data analysis

To quantify the different bending modes, we performed visual tracking of various actuators. We first fabricated actuators with minimum cut path distances in the range of about 440 μm to about 40 μm (the minimum distance we could reliably cut), all with a membrane thickness of approximately 150 μm (formally, 146 μm mean with a standard deviation of 8.4 μm, n = 24). As such,

minimum cut distances ranged from three times the membrane thickness down to the smallest distance we could fabricate successfully (determined in part by thermal damage effects, discussed below).

To test an actuator, we secured it to a custom-made fixture, positioning the actuator as a cantilever beam. After pneumatically pressurizing the actuator to a set value (70 kPa) as determined by an integrated digital pressure gauge (BSP000W, Balluff Inc.), we used a syringe pump (Pump 11 Elite, Harvard Apparatus) to deliver a known volume of additional air (10 mL at a rate of 25 mL/min). With a pair of high-speed cameras (Phantom v7.3, Vision Research Inc.) arranged orthogonally, we visually tracked the tip position of the actuator as it deformed. The three-dimensional path of the tip of the actuator was reconstructed using a custom MATLAB (v. R2017a, MathWorks Inc.) script that relied in part on motion analysis software (ProAnalyst, Xcitex Inc.). The output of the reconstruction was the entire position history of the tip of the actuator, with corresponding pressure values.

The final bend angle ϕ_{bend} is defined as the inverse tangent of the deflection along the z-axis with respect to deflection along the y-axis (Fig. 3.3A). As such, a typical out-of-plane bending actuator (i.e., one that bends entirely about the y-axis) would have a bend angle of 90°. Similarly, an actuator that demonstrates fully in-plane bending (i.e., one that bends entirely about the z-axis) would have a bend angle of 0°. The data in Fig. 3.3B show that indeed there is a transition from out-of-plane bending to in-plane bending as the minimum cut distance approaches and subsequently passes below the membrane thickness.

It is interesting to note that the data are quite spread within the transition region from out-of-plane bending to in-plane bending. We hypothesize that, in addition to material irregularities and manufacturing imperfections, some of the spread may be attributed simply to the hyperelastic nature of the material. As the actuator is pressurized, the thinnest portion (whether that is the membrane defined lithographically or the sidewall defined by laser cutting) will expand to a much larger degree than the rest of the actuator. When the minimum cut path distance is of similar magnitude to the membrane thickness, we observe complex, hybrid motions in which an actuator will transition from one bending mode to another throughout the course of a single inflation. We believe this behavior is due to a strain stiffening effect, wherein the elastic modulus increases with increased deformation. As such, it is not only the geometry of the actuator but also the time-varying mechanical properties of the material that influence bending motion.

In this work, we do not present an analytical model of these bending actuators. Such a model would require detailed understanding of the relative influences of actuator geometry and the time-varying mechanical properties of elastomers that experience very high strains. To be of practical use, a model would also need to accommodate the influence of external forces that arise through contact between the actuators and their environment. As such, we decided that a model of this type was outside of the scope of this work.

3.2.4 Thermal damage and minimum cut distance

In the process of cutting through the elastomer, the laser beam damages a small region surrounding the cut path, altering the elastomer surface to such a degree that it can no longer be bonded by oxygen plasma treatment. After performing quantitative analysis, we concluded that this region of thermal damage extends up to 40 μm away from either side of the beam.

To quantify the effect of thermal damage from the laser on the functionality of our structures, we fabricated arrays of soft microactuators with incrementally smaller and smaller minimum distances between the laser cut path and the actuator features. Each actuator was inflated by hand with a syringe containing colored water. A digital pressure gauge recorded the pressure in the line. The pressure was increased slowly until the actuator burst (at which point the maximum pressure was recorded), or until the pressure reached 200 kPa.

In Figure 3.4 we plot the pressure from the gauge as a function of minimum cut distance. We summarize the data in the plot by grouping distance ranges, which can be seen in Table 3.1. In general, we note that above 40 μm all actuators reached the maximum pressure tested, suggesting that laser cut paths should be at least this distance from any feature to avoid leaks.

3.3 Injection-induced self-folding

Traditional soft actuators deform in response to a stimulus (e.g., pressure change for fluidic actuators, electric field for electroactive materials), and re-

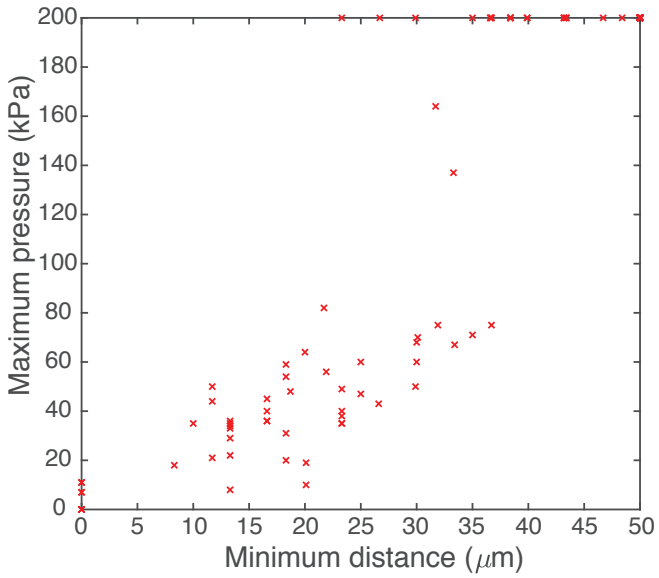

Figure 3.4: Thermal damage study. Note that actuators that did not leak even at 200 kPa are plotted at 200 kPa.

Distance range (μm)	0 - 10	10 - 20	20 - 30	30 - 40	40+
Average burst pressure (kPa)	1.4	35.9	72.8	158.8	200
% of successful actuators	0	0	18.8	61.1	100
n	39	19	16	18	85

Table 3.1: Thermal damage study, with data collected into groups. Note that above 40 μm, we see 100% successful actuators. "% of successful actuators" refers to actuators that reached the maximum tested pressure of 200 kPa.

main in that deformed state for only as long as the input is applied. For instance, a typical bending fluidic actuator is one that is straight under atmospheric pressure, but bends when pressurized. When allowed to depressurize (i.e., when the input is removed), the actuator returns to its initial, undeformed state. Below, we investigate alternative actuator behavior.

3.3.1 Structural locking principle

In this work, we demonstrate elastomeric fluidic actuators that can be "structurally locked" in their deformed states through what we define as "injection-induced self-folding". Upon pressurization, chambers within the microfluidic circuitry expand to actuate portions of the laminate through preprogrammed motions. Actuation with an inert working fluid (such as air or water) permits recovery of the initial configuration upon depressurization, while the use of a phase-changing material converts deformed actuators into permanent structural elements. Here, we refer to materials that undergo an irreversible phase transition (e.g., solidification) when exposed to specific stimuli, such as UV light or temperature as "phase-changing materials". Using these phase-changing materials, we are able to pressurize an actuator with the fluid material, and then solidify that material, effectively locking the entire structure in its deformed state. In this way, it is possible to obtain a complex 3D soft microstructure analogous to the folding-based assembly of pop-up book MEMS[129], but entirely soft. Combining both actuation strategies (i.e., the use of both inert and phase-changing working fluids) enables the transformation of static 2D laminates into dynamic 3D structures.

3.3.2 Materials

In this work, we primarily use UV-curable resin as the phase-changing material. We have also investigated the use of the uncured form of the bulk elas-

tomer. Using the elastomer precursor results in a monolithic structure that is entirely soft, and also offers an alternative stimulus for structural locking (i.e., thermal curing rather than UV curing). When total recovery of the initial configuration is required, simply using an incompressible fluid (such as water) and closing an input valve would be a viable alternative to achieve structural locking. While one could inject all microfluidic channels with a phase-changing material that is subsequently solidified, the result would be a 3D, yet entirely static structure. Far more interesting is the combination of working fluids, simultaneously locking some actuators into structural elements, while reserving other actuators to control motion.

We tested the concept of injection with phase-changing materials on simple actuators. We considered materials that cure under different stimuli, that have viscosities ranging over an order of magnitude, and that provide a range of mechanical properties, from a UV curable gel (SilGel 613) to a rigid resin (Sartomer SR355). In Fig. 3.5 we show simple soft microactuators injected with those materials. Specifically, Fig. 3.5a is a spherical actuator injected with UV curable silicone elastomer (Wacker Semicosil 912), Fig. 3.5b shows a bending actuator injected with the UV curable resin mixture (Sartomer SR355 (90%) and Esacure KTO 46 (10%)), and Fig. 3.5c shows a bending actuator injected with UV curable silicone gel (Wacker SilGel 613).

In Fig. 3.6 we can see a bending actuator injected with Sylgard 184 (mixed with a red dye for better visualization), which was thermally cured inside the actuator at 60°C for 1 h. We imaged the actuator with a confocal microscope

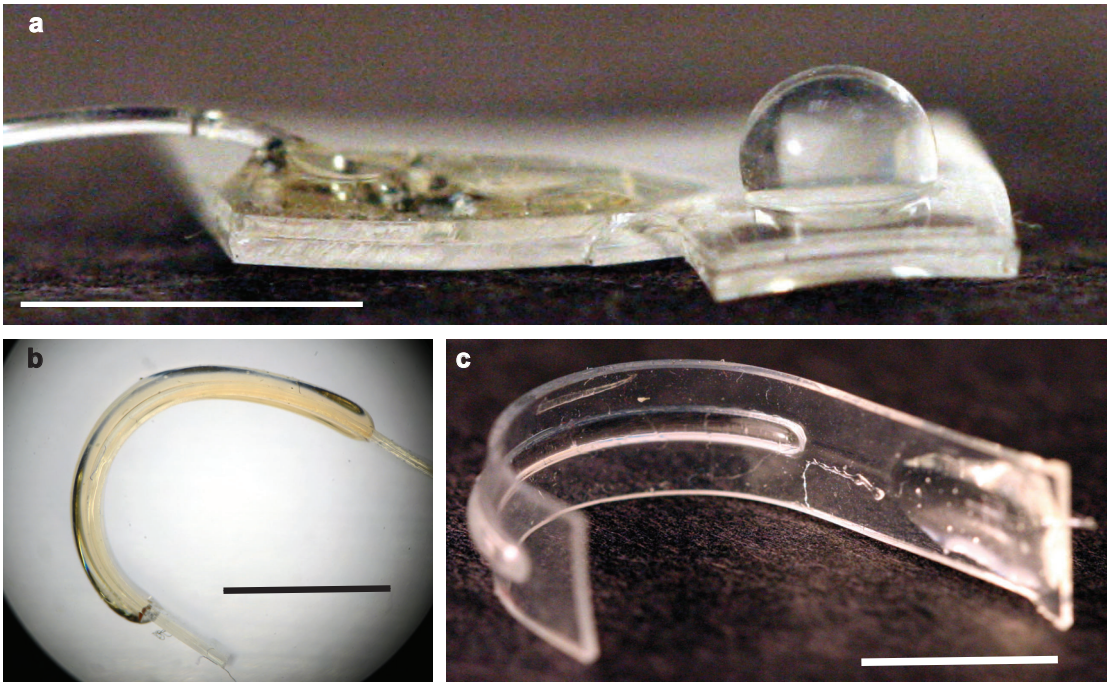

Figure 3.5: Folding resulting from the injection of UV curable materials. a) Spherical actuator injected with UV curable silicone elastomer (Wacker Semicosil 912). b) Bending actuator injected with UV curable resin mixture (Sartomer SR355 (90%) and Esacure KTO 46 (10%)). c) Bending actuator injected with UV curable silicone gel (Wacker SilGel 613). Scale bar is 5 mm.

(Olympus LEXT OLS4000, Olympus Corporation). In the inset of Fig. 3.6, we can appreciate the laser cut edges of the two layers composing the actuator as well as the area that is not bonded due to the thermal damage during the laser cutting process (indicated with arrows).

We injected some of the leg sublaminates with UV curable resin to demonstrate the fabrication of more complex 3D structures (Fig. 3.7). In this case, the injection of a more rigid material results in a skeleton. The use of the phase-changing materials enables us to generate a range of mechanical properties in the final structure depending on the material injected. Interfacial mechanic fail-

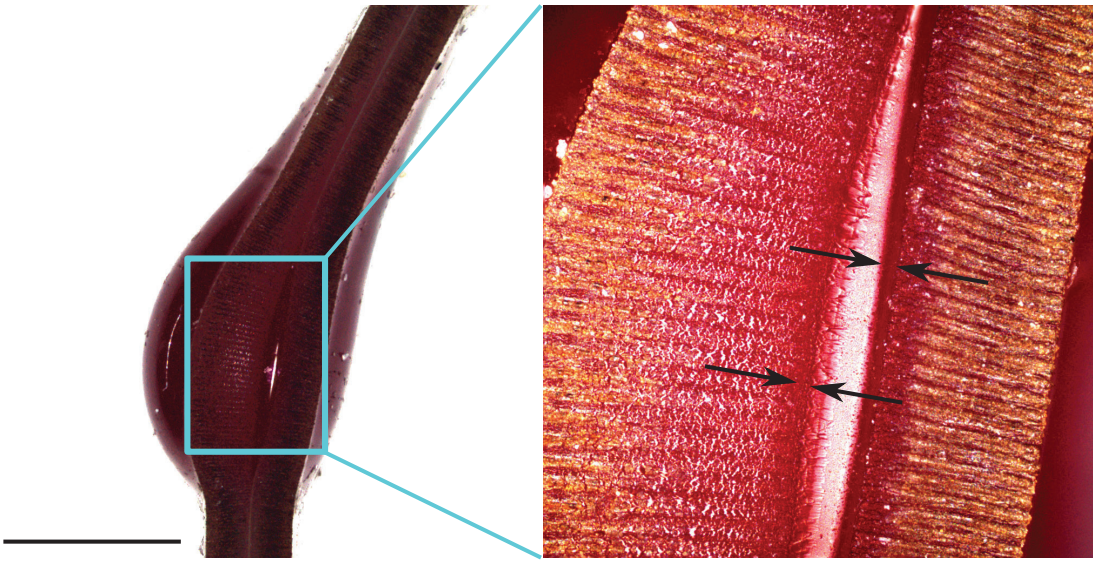

Figure 3.6: Folding resulting from the injection of thermally curable elastomer (Sylgard 184). Right inset: magnification of the interface between the two bonded layers composing the actuator, highlighting the small area of thermally damaged polymer. Scale bar is 1 mm.

ure is a risk especially when using stiffer and more brittle materials. However, if the injected material, while undergoing mechanical failure, does not tear the silicone elastomer, we observed that the shape is preserved as the containing elastomer tends to hold the injected material in place. Indeed, the large tear strength of the elastomer selected resulted in a highly robust structure that was able to maintain its shape even after inducing mechanical failure of the injected material. The flexibility in material selection, provided by the proposed manufacturing paradigm, allows the user to tune the mechanical properties of the soft actuator and the mechanical interface as desired. Therefore, one could appropriately design the relative mechanical properties of the bulk material of the soft actuator with respect to the properties of the injected material depending on the specific application requirements.

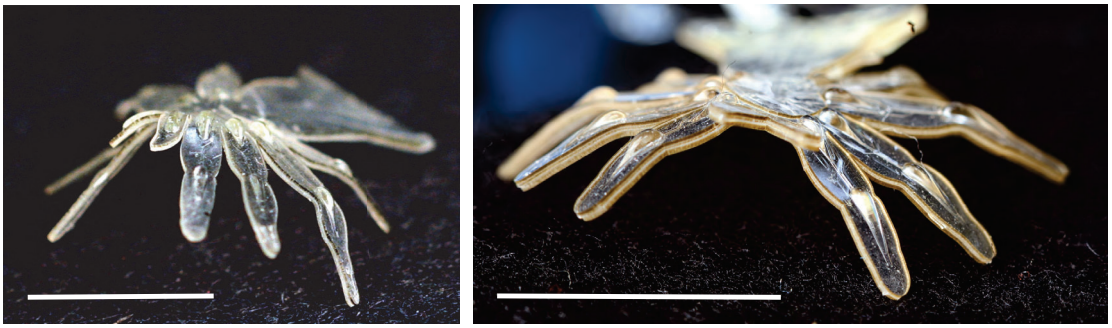

Figure 3.7: Spider leg sublaminates with structural degrees of freedom injected with UV curable resin. Scale bar is 10 mm.

3.4 Demonstration in a soft robotic spider

To demonstrate the capabilities of our fabrication strategy, we designed and fabricated a 12-layer monolithic soft peacock spider with integrated microfluidic circuitry and functional microactuators (Fig. 3.1, d-f). The soft spider is conceived as a demonstration of the multiple capabilities and features of the presented process, and it is not designed to achieve locomotion or to carry out a specific task. The complexity of the spider is best understood by individually considering the three sublaminates that compose it, each of which highlights particular benefits of this manufacturing approach.

At the bottom is the leg sublaminate, which is a three-layer laminate with two sets of actuators, one embedded on each of the top and bottom layers. Due to their relative positions, the actuators on the first and third layers act antagonistically (Fig. 3.1g); actuators on the first layer bend the legs up, while actuators on the third layer bend the legs down. We inject the third layer with phase-changing material, permanently deforming the legs into a bent configura-

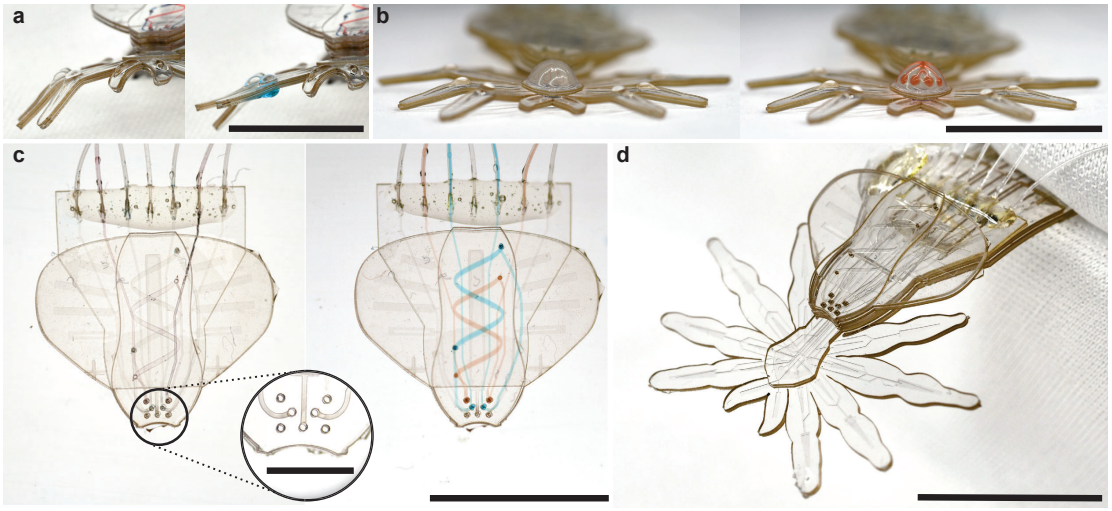

Figure 3.8: Overview of the spider structure and features. a) Detail of the legs after the injection of the structural degrees of freedom (left) and subsequent pressurization of the actuation degree of freedom with blue dyed water (right). b) Injection of the head (left) and subsequent coloring of the channels of the eyes (right). c) Abdomen sublaminate before (left) and after (right) coloring the two patterns that create the DNA symbol; inset: detail of the aligned features across the multiple layers. d) Fully assembled spider. Scale bar scale is 10 mm, except for inset in c) where it is 2 mm.

tion. By actuating the first layer, pressurized fluid at the joints forces the legs into a straight configuration (Fig. 3.8a). When the pressure is relieved, the legs return to the bent configuration. This actuation strategy mimics the biomechanics of actual spiders, whose legs are bent when not actively being straightened by internal turgor pressure[46], as is the case for the curled legs of a dead spider.

The middle sublaminate contains the head and eyes. These layers collectively demonstrate the ability to achieve hierarchical structures, as the eyes are secondary deformations on an already deformed head. The deformation induced in the head layer leads to a change in the geometry of the channels laying on top

of it (Fig. 3.8b).

The topmost sublaminate is the abdomen (Fig. 3.8c). This sublaminate highlights multiple functionalities, including multilayer fluid handling of a microfluidic circuit, different colored fluid patterns, and coordinated bending actuation that results in a structure with negative Gaussian curvature. The overall curvature of the abdomen is the product of the two principal curvatures; here, we have one curvature induced by the elevation degree of freedom (in the abdomen sublaminate, in yellow in Fig. 3.1H), and a curvature of the opposite sense due to the simultaneous actuation of the two flexing actuators (in the abdomen sublaminate, in dark and light blue in Fig. 3.1H). The result is a structure with negative Gaussian curvature.

In this structure, we also demonstrate the use of laser cutting on top of channels embossed in the soft layers to allow flow within, and between, sublaminates. The laser cutting step enables us to interconnect channels across layers in 3D, allowing fluids to move vertically through the laminate in a manner analogous to electrical vias in printed circuit boards. We enable this functionality by strategically laser cutting holes on each soft layer individually (after realignment to the embossed fiducials and before assembly) to interconnect the channels (embossed on each layer composing the laminate) in the third dimension once the layers are bonded together. This feature is particularly significant in the abdomen sublaminate, as we are able to pass the fluid through seven intermediate layers.

Mimicking the behavior of the peacock spider, three sets of independent actu-

ators are responsible for the abdomen movement: one elevating actuator raises the abdomen from a flat to a lifted configuration (in yellow in Fig. 3.1H) and two flexing actuators bend the abdomen outwards (in dark and light blue in Fig. 3.1H). To demonstrate colored fluid patterns and imitate the colorful abdomen of the animal, a pattern resembling the symbol of DNA is integrated on top of this sublaminate and colored fluid is injected through the 3D network of channels created by the combination of laser cut vias and microfluidic channels (Fig. 3.1I). The circuit is designed to be open and double-ended, to demonstrate the possibility of continuously exchanging colors.

When assembled together, these three sublaminates make up a full MORPH system composed of 12 layers (Fig. 3.8d). The device has nine independently controllable degrees of freedom and five structural degrees of freedom. The sequence of injection of the structural degrees of freedom is reported in Fig. 3.9, a-c. Actuation degrees of freedom are shown in Fig. 3.9, d-g.

The overall size of the device is 25 mm in width and the minimum feature size is 40 μm (the height of the microfluidic channels) (see Fig. 3.10 for a sense of scale). The thickness of the soft laminate in the flat configuration is about 2.8 mm and the spider reaches a height of nearly 20 mm when fully actuated. Structurally, this fully 3D multimaterial soft system features an intricate profile and internal geometry consisting of feature sizes that, taking advantage of the scalability of current soft lithographic techniques, may extend to the nanoscale. Functionally, the spider is highly reconfigurable, with nine individual degrees of freedom to control motion in multiple distinct directions, and incorporates

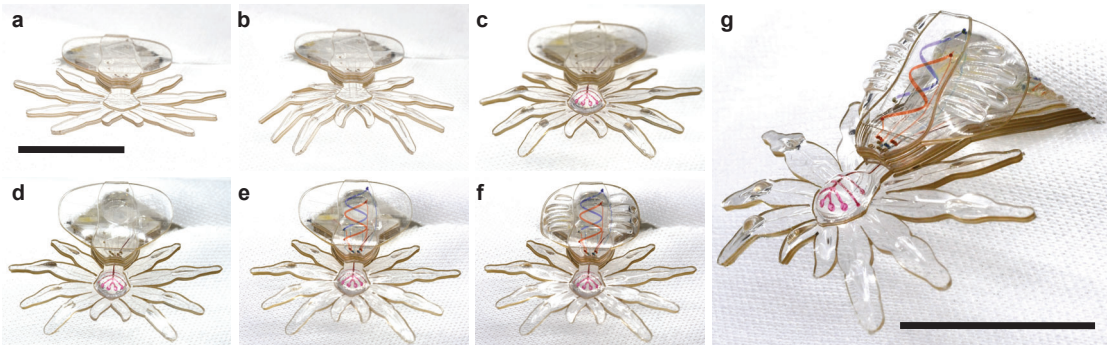

Figure 3.9: Sequence of injections that assemble and actuate the spider demonstration. a) Flat configuration post lamination. b) Legs after structural degree of freedom inflation: hips, left and right knees, and chelicerae (jaws). c) Head injection and coloring of the microfluidic channels of the eyes. d) Actuation of the elevation degree of freedom on the abdomen. e) Coloring of the DNA pattern by flowing dyed water in the microfluidic circuit. f) Actuation of both the flexing degrees of freedom on the abdomen. g) Isometric view of the 3D spider with the abdomen degrees of freedom active. Scale bar is 10 mm.

a multilayer microfluidic circuit with a 3D channel network. Future efforts will be targeted to use this technology to design functional robotic devices able to address specific challenges in areas such as surgical robotics, micromanipulation, and wearable devices.

3.5 Conclusions

The framework demonstrated here provides an example device in the form of a peacock spider showing the first steps into truly 3D soft meso- and micro-devices that are morphologically complex and contain embedded multilayer microfluidic circuitry. Leveraging the extensive work already done in many areas of traditional microfluidics, future MORPH devices could include a fluidic computation unit that would provide on-board motion coordination in a manner

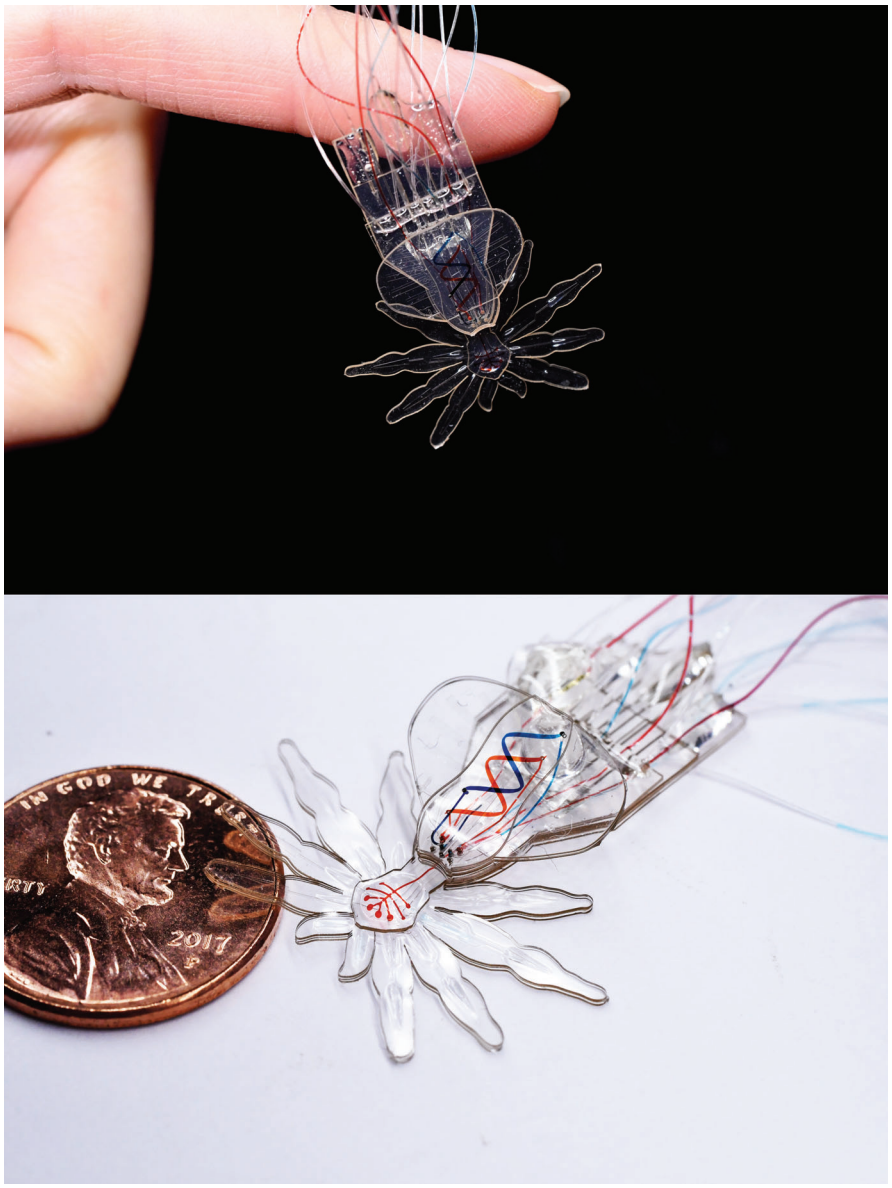

Figure 3.10: The final device next to common objects to provide a sense of scale.

similar to the central pattern generators of biology. In this way, a simple input signal could be manipulated into a complex output signal that enables intricate actuation of legs or other appendages. Additionally, the robot could probe the environment to sense the presence of chemicals or other phenomena of interest such as fluid flow, vibration, or light, and respond in an appropriate manner.

Whereas this chapter and the preceding one have examined passive control for soft robots in the form of morphological computation, we next turn to a discussion of active control in the form of fluidic computation, in hopes of providing some of the capabilities discussed above.

4

Microchannel Fabrication

In this chapter, we begin our exploration of a system of active control manifested in microfluidic logic circuits. We first lay a foundation for future, system-level concerns by examining the most fundamental building block of a fluidic circuit: the microchannel.

4.1 The relevance of microfluidics

Microfluidics is the study of very small volume fluid flow. In chemistry, microfluidics finds applications in the delivery of precise amounts of chemicals into reaction chambers. In biology, applications range from cell manipulation to protein analysis. As we saw in the last chapter, there may be interesting applications of microfluidics within the field of soft robots, if the fluid under consideration is the working fluid that drives an actuator. Beyond simply driving a single actuator, there may be significantly more interesting applications if we are able to adopt the digital logic systems that have been demonstrated in microfluidics and translate them into soft robotic systems. In this way, a soft robot may be programmed with an active controller that runs on fluid, in a manner analogous to how a microcontroller runs on electricity[72].

The translation of traditional microfluidics to soft robotics relies heavily on the adaptation of microfluidic valves. Without valves, there is no way for one channel to interact with another; the microfluidic valve is analogous to the transistor of electronics, and is the building block of any system of digital logic. As we shall see, the cross-sectional geometry of the microchannels is critical to the successful operation of a microfluidic valve. Fabrication strategies to control the cross-sectional geometries of microchannels is the topic of this chapter.

4.2 Importance of microchannel shape

In microfluidics, standard photolithographic techniques produce vertical sidewalls, yielding channels with rectangular cross sections. Such microchannels may be appropriate for a number of applications, but they pose extreme challenges in other areas, such as modeling vascular networks[9,130,20] and optofluidics[84,7,63], to name just a few examples. Consequently, one often wants control over the cross-sectional geometry of the microchannel.

4.2.1 Microfluidic valves

Channel shape is perhaps most critical in the case of microfluidic valves. Given two perpendicularly oriented microchannels that are slightly offset in the vertical dimension (so that only a thin membrane separates them), pressurizing one channel causes a deflection of the membrane into the second channel such that flow in the second channel is impeded (see Fig. 4.1). In this way, the flow within a microchannel can be modulated by the flow within a different, independent microchannel. First reported in 2000 by Unger et al.[118], microfluidic valves enable interactions between two disconnected microchannels. In that work, the authors demonstrate the capabilities of their valve by creating an elastomeric peristaltic pump. In 2002, Thorsen et al.[109] expanded this work to address large-scale integration, opening the doors to microfluidic multiplexors in which thousands of microchannels can be controlled with only a few inputs. Later work also looked at using these valves to make other pumps[14] and

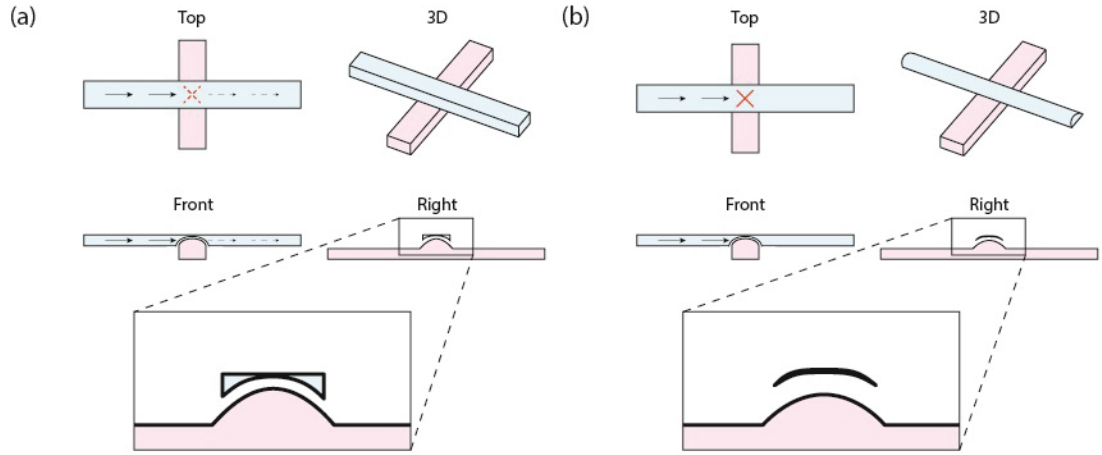

Figure 4.1: Sketches of the operation of a microfluidic valve in which the microchannel cross-section is (a) rectangular and (b) rounded. The control channel (red) is pressurized, which deflects the membrane and closes the flow channel (blue). Flow in (a) the rectangular microchannel is only partially stopped, while in (b) the rounded microchannel it is completely stopped.

mixers[55]. Additionally, microfluidic valves have become integral in biological automation[66], cell sorting[23], and protein separation[124]. They have been used to perform multiplexing[32] and, more recently, in digital fluidic logic, creating complex devices such as oscillators and shift registers[18].

4.2.2 Relevant microchannel parameters

There are a number of important parameters in the design of an effective microfluidic valve. As discussed in Studer et al.[104], membrane thickness, whether the valve is push-up or push-down, channel aspect ratio, and general scaling properties are all crucial considerations. But most fundamental to the basic functionality of a microfluidic valve is the channel profile. If a microchannel has a rectangular cross section, the deflected membrane cannot fully collapse

into the sharp corners, and flow will not be stopped. A number of groups have modeled valve closure mechanics, and have identified the most promising cross-sectional geometries[118,24,21,39,76,31]. These papers unanimously agree that a channel with rounded corners is necessary for complete valve closure. The difference in valve operation between rectangular microchannels and rounded microchannels can be seen in Fig. 4.1.

4.2.3 Fabricating rounded microchannels

Previous studies have already identified and analyzed the ideal channel shape; in this chapter, we are interested in the fabrication strategies that best produce that shape. In that regard, a number of techniques have been proposed.

The first microfluidic valves were fabricated by molding off of masters that were made with a positive photoresist. When heated to an elevated temperature, the positive photoresist reflows, creating rounded features[118]. This technique has been adopted by a number of later groups[92,122,123], and has garnered enough attention to merit a systematic characterization of the method[21]. However, there are a number of challenges associated with this method, such as the relatively low chemical and thermal stability of many positive photoresists compared to more robust alternatives[16,2]. Particularly, some of the most common positive photoresists (e.g., SPR 220) fail to integrate well with some of the most common negative photoresists (e.g., SU-8), so even using positive photoresists only for the valves becomes impractical[19].

Consequently, researchers have investigated alternative fabrication strate-

gies. 3D printing microfluidic molds was first suggested long ago[64], and now researchers are directly printings microfluidic networks[96]; a recent review presents an updated analysis of this fabrication technique[121]. Some researchers have created rounded microchannels by exposing photoresist through the backside of a glass wafer with diffuse light[24], using an inflated PDMS membrane as a mold[31], and spin coating a second layer of photoresist to exploit capillarity[19]. Others have relied on gray-scale photolithography[12,132,59,136], the surface tension of PDMS[50,1], laser micromachining[107], removal of a cylindrical element[102,36,3,78,119,17], femtosecond laser pulses[7,63] and more.

In this chapter we examine in detail five techniques most applicable to the fabrication of microfluidic valves. We do so by fabricating microfluidic channels of the same dimensions with the five different techniques, and systematically catalog the variations. In doing so, we provide a direct comparison between these different techniques. The most important evaluation parameter is whether a given technique is able to achieve a rounded microchannel; we determine the quality of the microchannel shape by building example valves and measuring their performance. After considering the cross-sectional geometry of the channels, we evaluate each fabrication strategy on a number of additional metrics, which are described in the next section.

4.3 Design of experiments

To determine the most appropriate fabrication strategy, we adhered to a strict design and testing procedure, modifying only a single parameter at a time to investigate explicitly the influence of all variables under consideration.

4.3.1 Experiment description

The fabrication strategies were evaluated on microfluidic channels of varying dimensions. Target channel heights were 10 and 50 μm and target channel widths were 50, 100, and 250 μm, resulting in six distinct channel geometries with aspect ratios ranging from 1:1 to 1:25. (Note that these values intentionally challenge commonly accepted channel aspect ratio limits[85]. We are interested in how the various fabrication strategies perform not only in conservative microfluidic device designs, but in aggressive designs as well.)

For each fabrication strategy, we altered one key parameter to determine the sensitivity of the technique; in particular, we investigated three variations of each strategy. For five fabrication strategies with three parameter variations and six different channel dimensions, this equates to ninety unique channels to be compared (in addition to the six control channels).

4.3.2 Evaluation metrics

Evaluation of the various fabrication strategies is not limited to the resultant channel cross-sectional geometry (i.e., how well the strategy can produce

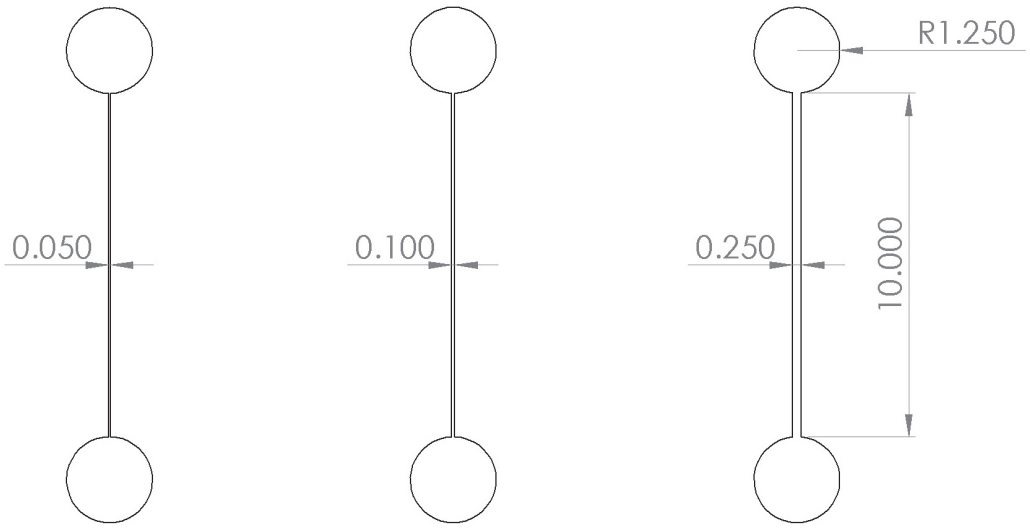

Figure 4.2: A schematic of the channel dimensions that were used to evaluate the five fabrication strategies. All dimensions are in millimeters. These three channels were fabricated at thicknesses of both 10 and 50 μm.

rounded channels). In addition, we consider resolution (i.e., the minimum feature size that can be made), dimension mapping (i.e., the correlation between design dimensions and actual device dimensions), fabrication time (both active and passive), fabrication difficulty (i.e., the amount of skill required and how tightly the process must be controlled), and process prohibitiveness (including such factors as the cost of necessary equipment, and the toxicity of chemicals involved).

4.4 Methods

All strategies but one rely at least in part on the soft lithography process[133]. In this process, a poly(dimethylsiloxane) (PDMS) device is molded from a master that is (typically) fabricated using photolithography. To make a master, a photosensitive polymer (i.e., a photoresist) is poured onto a substrate (typically a silicon wafer). When spun at high speeds, the photoresist coats the substrate evenly at a controllable thickness. After spin coating, the photoresist is exposed to a UV light source through a photomask, transferring the pattern from the photomask by cross-linking the photoresist. Upon being placed in a developer solution, the photoresist is selectively removed, leaving only the desired pattern. After surface treatment to prevent sticking, the photolithographic master can be used to mold PDMS devices that will have the negative structure of the master. After the PDMS negative cures, it can be bonded by means of oxygen plasma treatment to an unpatterned sample of PDMS, forming a final device. An overview of this process can be seen in Fig. 4.3.

4.4.1 Novel photomask fabrication procedure

For each method involving photolithography, we used a novel fabrication procedure to produce custom photomasks. We found that traditional photomask fabrication strategies were limited, mainly in process iteration time. To remedy this problem, we developed a new procedure which allows custom photomasks to be fabricated in under one hour, at a resolution that was suitable for our

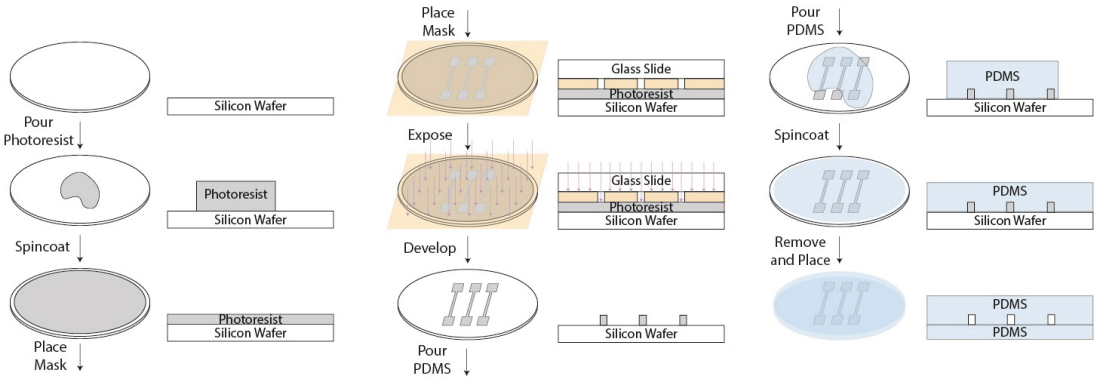

Figure 4.3: An overview of the soft lithography process. The pattern from a photomask is transfered to a photoresist-coated silicon wafer upon exposure to UV light. After development solution removes the excess photoresist, the patterned silicon wafer serves as a negative for future PDMS molding. Finally, the molded PDMS is adhered to unpatterned PDMS through oxygen plasma treatment.

needs.

To fabricate these custom masks, we first placed a thin (12.7 μm) sheet of UV-impenetrable, polyimide film (Kapton, DuPont USA) on WF Gel-Film (Gel-Pak, Delphon) that had been adhered to a glass slide. On top of the Kapton we placed a 5 μm double-sided adhesive (with both protective films removed). We then cut this laminate on a diode-pumped solid-state laser (E-355, Oxford Lasers Ltd.) in the desired pattern. After removing the scraps with tweezers, we then brought the laminate into contact with a new glass slide. Because the adhesive bond to the second glass slide is stronger than the bond between the Kapton and the Gel-Film, the Kapton and adhesive are transfered to the second glass slide (the Gel-Film remains on the first glass slide). This second slide (with the patterned Kapton adhered to it) serves as our photomask. We observed that this process creates high quality photomasks that do not suffer sig-

Mask	Nominal (μm)	Actual (μm)	Difference (μm)
Negative	50	62.1	12.1
	100	113.2	13.2
	250	264.2	14.2
Positive	50	40.3	-9.7
	100	92.5	-7.5
	250	241.2	-8.8

Table 4.1: Actual channel widths for the custom photomasks. The discrepancy is due to the kerf of the laser.

nificantly from the laser ablation process. An image of one such mask can be seen in Fig. 4.4. A diagram of the entire fabrication process can be seen in Fig. 4.5.

We used the same cutfile to generate the photomasks to be used with both the positive and negative photoresists (we simply removed the inverse "scrap" to form the inverse mask). Due to laser kerf, the final mask dimensions were slightly different. Channel widths for the two masks can be found in Table 4.1.

4.4.2 Control

Control devices were fabricated using the standard soft lithography process. Three inch, <100>, virgin test grade, boron doped, p-type silicon wafers (ID: 447, University Wafer) were used as the substrate. The 10 μm channels were fabricated with SU-8 2010 (MichroChem Corp.) while the 50 μm channels were fabricated with SU-8 2050 (MichroChem Corp.). Exposure was performed using a MAS 500 IR/VIS Mask Alignment and Exposure system, with a measured exposure power of 21.9 mW/cm^2 at 365 nm. For development, we used SU-8 De-

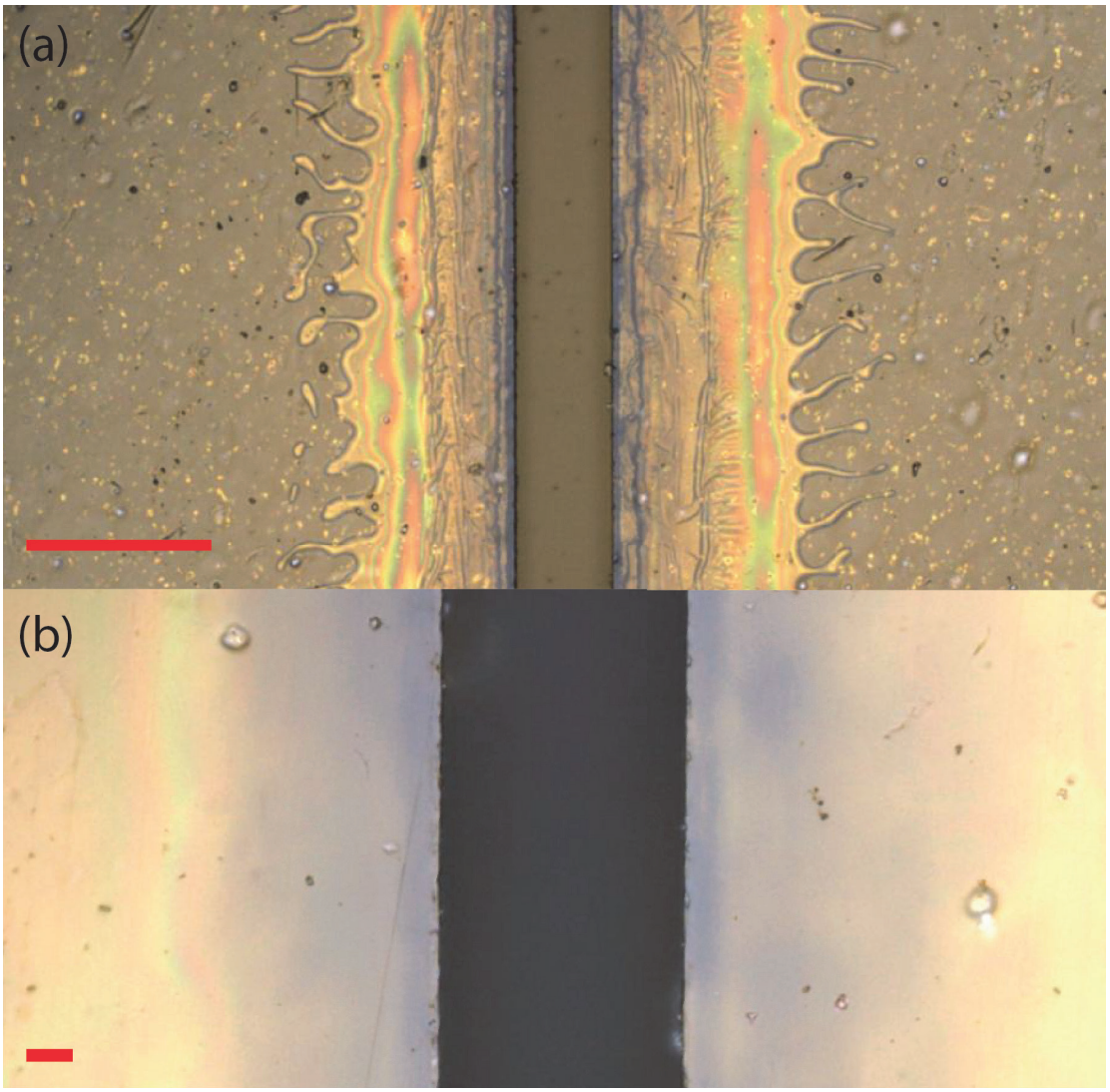

Figure 4.4: (a) An image of a section of the mask for the 50 μm channel. Note that the vast majority of the portion of the mask that appears to show thermal damage (the brighter yellow portion that surrounds the edge of the channel) is in fact only thermal damage to the adhesive layer, and thus does not compromise the performance of the mask. Scale bar is 100 μm. (b) The same section of the mask at higher magnification. Scale bar is 10 μm.

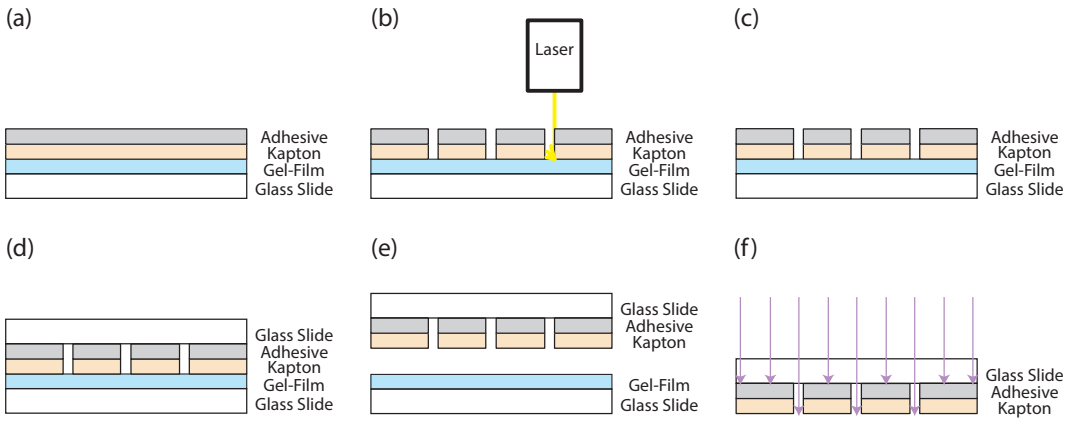

Figure 4.5: Custom photomask fabrication procedure. (a) Kapton is placed on Gel-Film that is adhered to a glass slide. Double-sided adhesive is placed on the Kapton. (b) The laminate is laser cut. (c) Scraps are removed. (d) A second glass slide is placed on top of the adhesive. (e) The second glass slide is pulled off, separating the laminate. (f) The Kapton adheres to the second glass slide, and can be used as a photomask.

veloper (MichroChem Corp.). For surface treatment, the silicon wafers were exposed to silane (trichloro(1H, 1H, 2H, 2H-perfluorooctyl)silane, Sigma-Aldrich) vapor in a dessicator.

After silanizing the wafers overnight, we poured PDMS (Sylgard 184, Dow Corning) that had been mixed in a 10:1 ratio (base:curing agent) over the wafers, degassed under vacuum to remove bubbles, and cured. Curing was typically performed at 60°C for at least four hours, although occasionally we cured at higher temperatures (up to 70°C) for shorter durations to enable faster process iteration.

Once cured, the PDMS was removed from the wafer and manually cut with a razor blade into thin (approximately 2 mm) slices to view the cross section of the channels. We used a confocal microscope (Olympus LEXT OLS4000, Olympus Corporation) to evaluate the channels and take dimensional data, while we

used a scanning electron microscope (SEM) to take the images that are presented in this chapter.

Except where noted, all of the strategies tested use the same fabrication procedure as has been described for the control devices.

4.4.3 Reflow of positive photresist (+PR)

Perhaps the most common method to achieve rounded microchannels is to reheat a developed photoresist pattern slightly beyond its melting temperature such that the photoresist begins to flow. Surface tension causes the corners of the device to round, changing the cross-sectional geometry of the device to a new shape that is retained upon cooling.

Unfortunately, SU-8 does not melt at a sufficiently low temperature to enable reflow. In the following procedure we used Megaposit SPR 220-7.0 positive photoresist (Dow Chemical Company). First, we prebaked a virgin silicon wafer at 115°C for five minutes. After cooling back to room temperature, we spincoated hexamethyldisilazane (HMDS) at 2000 rpm to promote adhesion of the photoresist to the wafer. We then spincoated the photoresist at 1500 rpm for a target thickness of 10 μm. We soft baked at 115°C for 90 seconds, and exposed at an energy dose of approximately 1300 mJ/cm^2. The photoresist was then allowed to rehydrate for at least four hours, after which we performed a post exposure bake at 115°C for five minutes. After allowing full cooling back to room temperature (at least 20 minutes), we developed in Megaposit MF-24A Developer (Dow Chemical Company) until the features were appropriately defined (which

can take 10-30 minutes). Once dry, we placed the wafer on a hotplate (set to either 90, 120, or 150°C) for five minutes to reflow the photoresist.

Due to the low viscosity of SPR 220-7.0, the maximum thickness of photoresist that can be achieved in a single spincoat is limited. In order to achieve a 50 μm layer of photoresist, multiple spincoat-bake cycles are required. Although multiple spincoat procedures producing layers up to about 54 μm have been reported[44], we found this procedure to be much too sensitive to warrant serious investigation. As such, we were unable to create any 50 μm thick devices using positive photoresist.

4.4.4 3D printing (3DP)

Among the fabrication strategies examined, 3D printing is unique in that it does not involve any type of photolithography. Molds were designed using commercially available CAD software (Solidworks, Dassault Systemes SOLIDWORKS Corp.).

For this method, we chose three different printers to compare: an Objet30 Scholar (Stratasys Ltd.), a Form 1+ (Formlabs), and a Titan 1 (Kudo3D Inc). The Objet30 uses a technique called PolyJet printing (a form of inkjet printing), in which droplets of liquid photopolymer are jetted onto a build tray, and then flash-cured with a UV light. The Form 1+ operates as a stereolithgraphy (SLA) printer, in which a focused UV laser traces patterns in a vat of photopolymer precursor. The Titan 1, also an SLA printer, is slightly different in that it uses digital light processing (DLP), in which the image of the entire layer is pro-

jected at once. We chose not to examine a fused deposition modeling (FDM) 3D printer; although these printers are among the most common style of printers, they often have relatively poor resolution. Conversely, 3D printers that use two-photon polymerization, such as the Nanoscribe (Nanoscribe GmbH), are able to achieve sub-micrometer resolution, but have a significantly limited build volume and are often prohibitively expensive. As such, they are outside the scope of this investigation. A thorough discussion of the various types of 3D printing can be found in a review by Waheed et al.[121].

4.4.5 Backside exposure through glass wafer (BSE)

This fabrication procedure closely follows the one outlined by Futai et al.[24], although with some minor variations. In this process, we used a 200 μm thick, 100 mm diameter borosilicate glass wafer (V015.04-1004, Plan Optik AG) instead of a silicon wafer as is traditionally used in photolithography. After the soft bake, the wafer is flipped over and the photomask is placed on the backside of the glass wafer. As a result, the photomask is offset from the photoresist by the thickness of the wafer. When the photoresist is exposed with diffuse (rather than collimated) UV light, the photomask offset causes the resulting channels to have sloping rather than vertical sidewalls. Because our UV light source outputs collimated light, we had to introduce an additional optical element. For this modification we placed a 120 grit UV fused silica ground glass diffuser (DGUV10-120, Thorlabs Inc.) approximately 7mm above the photomask.

The test parameter that we varied in this fabrication strategy was the exposure energy. For both the 10 and 50 μm devices, we chose to expose at the recommended energy (from the datasheet) and at both 50 and 100 mJ/cm^2 above the recommended value. For the 10 μm device (using SU-8 2010), the corresponding exposure energies are 125, 175, and 225 mJ/cm^2, while for the 50 μm device (using SU-8 2050), the corresponding exposure energies are 150, 200, and 250 mJ/cm^2. Although the direct exposure power of our UV light source was measured as 21.9 mW/cm^2, the power was reduced to 20.4 mW/cm^2 by exposing through the glass wafer, and further reduced to 12.3 mW/cm^2 when the diffuser was introduced. Thus, we used this last value (12.3 mW/cm^2) when calculating the relevant exposure times.

4.4.6 Inflated PDMS membrane (IPM)

Following the work of Hongbin et al.[31], this fabrication strategy uses a PDMS device as the mold for a second PDMS device. In this method, the first PDMS device is made using the standard soft lithography process. This PDMS device is then bonded to a thin PDMS layer that has been spun onto a silicon wafer at 1000 rpm, resulting in a membrane that is about 75 μm thick. To bond the two layers, we exposed the PDMS to oxygen plasma (35 W at 0.4 mbar for 20 seconds) using a low pressure plasma system (Pico BR PCCE 7", Diener electronic GmbH + Co. KG). After silanizing the resultant PDMS device, we had a set of functional microfluidic channels. This device was then used as a mold for the second PDMS device. We punched inlet holes and connected the channels

to a pressure-regulated air supply. Pressurizing the channels caused the thin membrane to deflect. We then cast a new layer of PDMS over the PDMS mold (while still under pressure), and cured. In this way, the shape of the deflected membrane of the PDMS mold is transfered to the resulting PDMS device. See Hongbin et al.[31] for a figure showing this process.

As reported by Hongbin et al.[31], the deflection of the membrane depends in part on the width of the channel. However, it also depends in part on the degree of pressurization. Thus, we tested this procedure under inflation pressures of 1, 3, and 5 psi (6.89, 20.68, and 34.47 kPa, respectively). These pressures are higher than those reported by Hongbin et al., but are reasonable due to the fact that we used a thicker membrane.

4.4.7 Secondary spin coating (SSC)

The final fabrication strategy examined here is based on the "thin film wings" method reported by Dy et al.[19]. In this method, a master is made in the typical photolithographic procedure using SU-8 photoresist. As such, the structure will have vertical side walls and sharp corners. A thin film of SU-8 is then spun onto the structure. Capillary action causes the liquid SU-8 to wick into the sharp corners of the master. After soft bake, exposure, and post exposure bake, the secondary photoresist layer adheres to the original photoresist structure, resulting in a final master that features rounded corners.

For this fabrication method, we varied the spin coat speed to control the thickness of the second photoresist layer. We were careful to try to deposit the

same amount of photoresist on each sample, which was a roughly 25 mm diameter pool of photoresist in the center of the wafer. The spin coat speeds we tested were 1000, 2000, and 4000 rpm.

4.5 Results and discussion

After fabricating and imaging the microchannels produced with the various techniques described above, we were able to draw a number of significant conclusions. The test results are summarized in general before we examine each technique individually.

4.5.1 Summary of results

Compared to the control, all of the fabrication techniques produced rounded microchannels, predicting good performance as microfluidic valves. These predictions were confirmed by fabricating and testing actual valves, as discussed below. The detailed results for each method will be presented in the following subsections as well as in the conclusion; here we compare the results across methods.

In Fig. 4.6 we compare the shapes of the channels fabricated from the different techniques. For easy comparison, here we only consider the 10×100 μm channels. Because neither the inflated PDMS method nor the secondary spin coating method produced channels of 10×100 μm, they are excluded from Fig. 4.6.

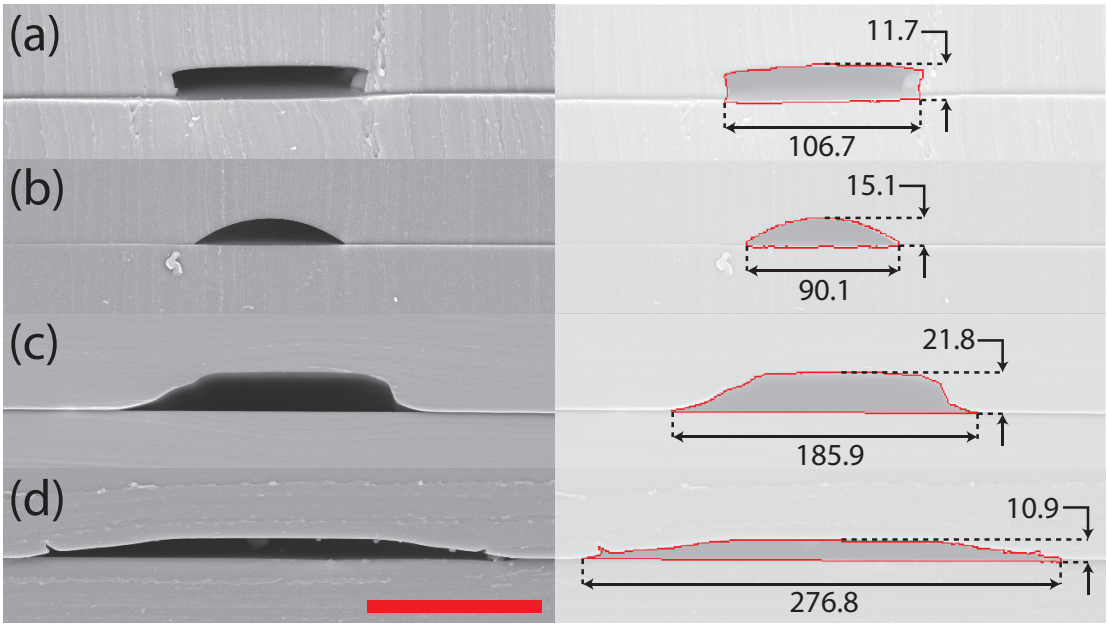

Figure 4.6: SEM images of 10 × 100 μm channels for the different techniques. (a) Control. (b) Positive photoresist, reflowed for 5 minutes at 150°C. (c) 3D printed mold on Titan 1 from Kudo3D. (d) Backside exposure at 225 mJ/cm^2 exposure energy. As the last two methods (IPM and SSC) failed to produce channels of the specified dimensions, we do not include them here. (Left) Original SEM image. (Right) SEM image with channel highlighted and dimensions added. All dimensions are in micrometers. Scale bar is 100 μm.

To further quantify channel shape quality, we fabricated microfluidic valves (as described in Fig. 4.1) with the three methods that produced 10 × 100 μm channels (as well as with the control channels). With flow channel pressures of five and ten psi, we tested the necessary control channel pressure (up to a maximum of 25 psi) required to both slow and completely stop flow. The results of these tests are reported in Table 4.2. While these tests were performed using air as the working fluid, we repeated the tests with water and found analogous results.

In Fig. 4.7, we plot the deviation of the actual dimensions from the target

	Flow pressure	Control pressure (slow flow)	Control pressure (stop flow)
Control	5 psi	13 psi	23 psi
	10 psi	19 psi	n/a
+PR	5 psi	11 psi	13 psi
	10 psi	15 psi	17 psi
3DP	5 psi	9 psi	12 psi
	10 psi	13 psi	17 psi
BSE	5 psi	4 psi	5 psi
	10 psi	10 psi	11 psi
IPM	–	–	–
SSC	–	–	–

Table 4.2: Results of microfluidic valve testing with flow channels fabricated from the different methods that produced 10 × 100 μm channels. Control channels were 10 × 250 μm and the membrane thickness was approximately 50 μm. We report both the control pressure required to slow and completely stop flow, as determined by observing the rate of bubble production when we submerged tubing connected to the output of the flow channel. The maximum control pressure tested was 25 psi; above this value we classify the valve as exhibiting incomplete closure.

dimensions for all fabricated channels. For methods involving photolithography, the target dimensions are simply the dimensions of the photomask. For 3D printing, the target dimensions are the dimensions defined in the print file.

4.5.2 Control

As expected, control samples fabricated with SU-8 produced channels with nearly vertical sidewalls (see Fig. 4.6(a)). In fact, the sidewalls are slightly undercut (likely due to minor underexposure, despite using the manufacturer's recommended exposure energy), suggesting even worse valve closure performance. Compared to the target dimensions, the actual microchannels were consistently within just a few micrometers (for both channel width and channel height).

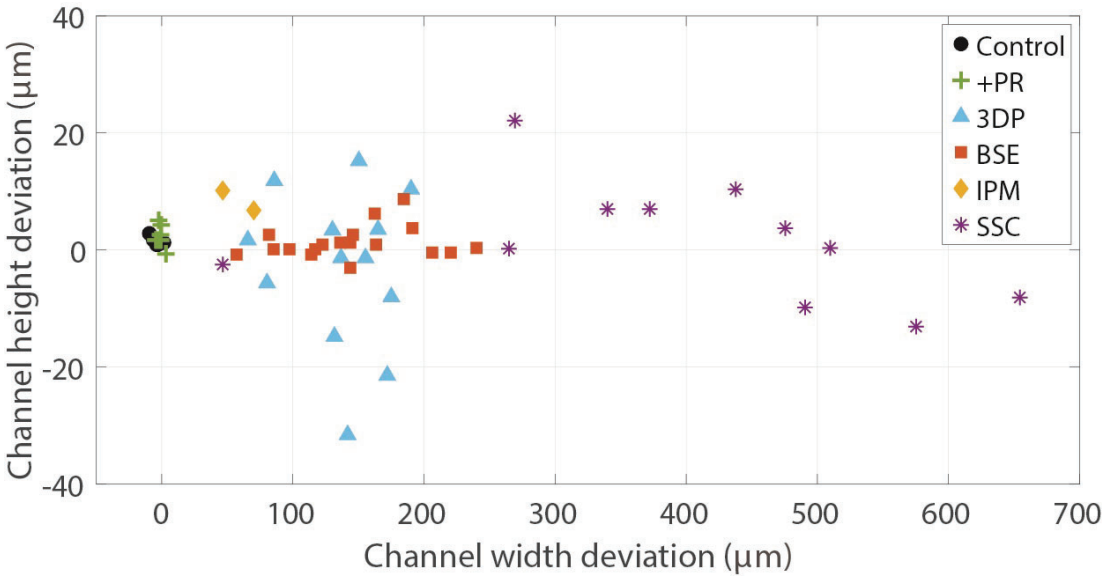

Figure 4.7: Plot showing the deviation of actual channel dimensions from those of the photomask (or, in the case of 3D printing, the print file). Each plotted point represents a distinct microchannel that was fabricated and measured.

4.5.3 Reflow of positive photoresist

Determining an appropriate recipe for the positive photoresist we used (SPR 220-7.0) was extremely challenging. To determine our recipe, we relied on the datasheet recipe as a starting point, but made modifications based on equipment and processing specifics. We found this process to be highly sensitive to small variations in procedure. Even more challenging was the variability of results from one experiment to the next, despite using the same process parameters. The source of this variability was likely do to the fact that fabrication was performed in a loosely regulated clean room, whereas processes that use this photoresist are typically performed in a much more tightly controlled cleanroom.

Once these challenges were overcome and we found a suitable recipe, we were able to produce high quality microchannels with regards to both cross-sectional geometry and resolution. As shown in Fig. 4.8, reflow of the post-development device at different temperatures allows for fine control of channel geometry. However, we were unable to achieve channels of 50 μm thickness, due to the complications introduced by attempting multiple spin coating steps, as noted previously. As has been noted by others[21], the final geometry of the microchannel is dependent on the processing parameters, and predicting the geometry of the final, rounded channels from the geometry of the rectangular channels is not as trivial as may be naïvely assumed.

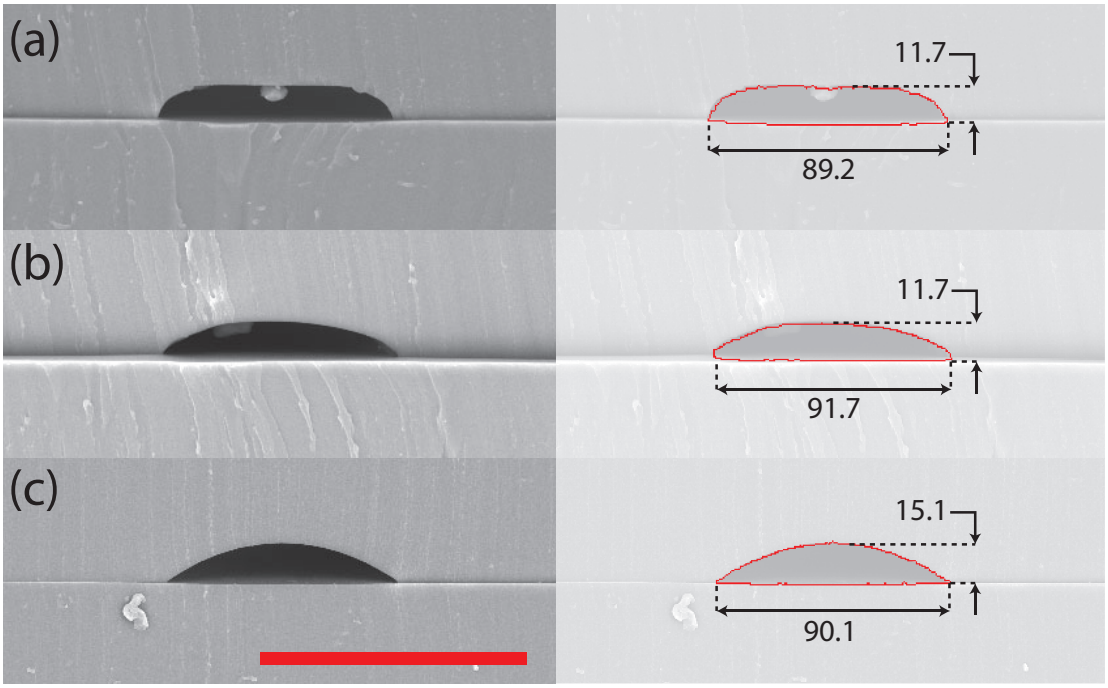

Figure 4.8: SEM images of 10 $\times$ 100 μm channels reflowed for five minutes at (a) 90°C, (b) 120°C, and (c) 150°C. (Left) Original SEM image. (Right) SEM image with channel highlighted and dimensions added. All dimensions are in micrometers. Scale bar is 100 μm.

In summary, this technique is able to produce very fine channel sizes with good control over channel shape, but is inappropriate for thicker channels. Additionally, this method requires strict process control and substantial infrastructure, which may make it inaccessible for many potential users.

4.5.4 3D printing

In general, the chosen 3D printers performed well; the cross section shape of the microchannels were all suitable. Using 3D printing for microfluidic valves is promising in that rounded microchannels are achieved "for free" at smaller dimensions due to either surface tension effects (in the case of the Objet30 and other Polyjet printers) or due to the spatial energy distribution of UV light projections (in the case of SLA printers like the Form 1+ and the Titan 1). Additionally, the fabrication process is extremely simple and almost entirely "hands off".

However, there are shortcomings. The resolution on current 3D printers is limited; many are unable to print at the size scale of interest, and those that are able can only do so at the expense of distorted dimensions. As can be seen in Fig. 4.6(c), there is poor correlation between the dimensions defined in the print file and the actual microchannels that are fabricated. However, if the relationship between the file dimensions and the physical dimensions is well understood, this problem can be avoided.

When printing on the Objet30, we were careful to control for print direction. One can see in Fig. 4.9 that the direction of travel of the print head has a sub-

stantial effect on the print quality of channels of these sizes. Ideally, one would always be able to align the direction of the channel with direction of travel of the print head. However, for most microfluidic chips this restriction is not feasible. For this reason, other printing technologies may be more appropriate.

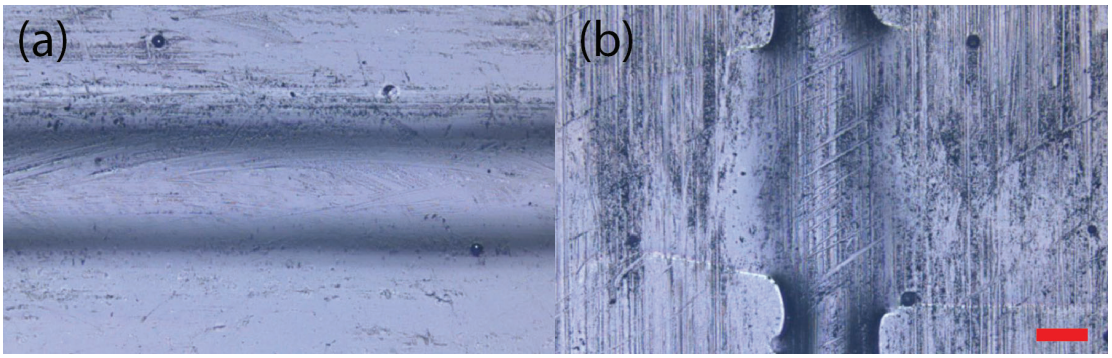

Figure 4.9: Confocal microscope images of channels printed (a) parallel and (b) perpendicular to the direction of travel of the print head of the Objet30 Scholar from Stratasys. In these images, the print head travels from left to right. Note how the microchannel in (a) is smooth and consistant while the microchannel in (b) is broken. Scale bar is 100 μm.

As mentioned above, many printers are unable to print at the small scale in which we are interested. Even with the printers we examined here, we often tried to print below the advertised resolution, as can be see in Table 4.3. When printing below the nominal resolution of the printer, we consistently found that feature dimensions were of compromised fidelity. We found that the Objet30 was unable to print the 50 μm wide channels at all.

Another relevant consideration is the tray size of the printer. Most high resolution printers have a limited build volume which is defined in part by the size of the build tray. While for many microfluidic applications this may not be an issue, it is a limitation that should be noted.

	Feature size	Layer thickness
Objet30	100 (μm)	28 (μm)
Form 1+	300 (μm)	25 (μm)
Titan 1	50 (μm)	5 (μm)

Table 4.3: Comparison of the advertised resolution for each printer used, from the corresponding manufacturer website. The "feature size" corresponds to the XY resolution, while the "layer thickness" corresponds to the Z resolution.

Finally, users may see limitations due to the surface roughness of the printed molds. As the printers in this study all employ printing styles (PolyJet, SLA, DLP SLA) that require thermosets, there are unfortunately few post-processing options that are viable, given the feature sizes of interest. In other types of printing (such as FDM) that use thermoplastics, parts may be treated with an acetone vapor polish to increase surface smoothness. If surface roughness becomes a significant issue, one solution is to simply use a more advanced printer. At the time of this writing, there are a number of high resolution DLP SLA printers that offer excellent surface quality; perhaps the highest surface quality is offered by printers using continuous liquid interface production (CLIP)[117].

In summary, 3D printing is an extremely simple method to produce rounded microchannels of good cross-sectional geometry. However, resolution is often limited, physical dimensions may vary greatly compared to print file dimensions, and overall print size can be small.

4.5.5 Backside exposure through glass wafer

As noted in the Methods section, we used exposure energies that were either recommended by the photoresist datasheet, or slightly above. Comparatively higher exposure energies were reported by Futai et al.[24]. Regardless, we found that increased exposure energy led to increased channel widths, in concurrence with Futai et al.

However, we did find some degree of tearing of the PDMS upon removal from the wafer. This phenomenon can be seen in Fig. 4.10. The tearing appears to have no correlation with channel dimension, as it was seen in different samples across a range of channel widths and heights (see also Fig. 4.11). Most likely, the relevant parameter here is the wafer material (all other wafers were silicon, whereas this technique requires glass). The authors are confident that this problem could be overcome with a simple surface treatment of the glass wafer.

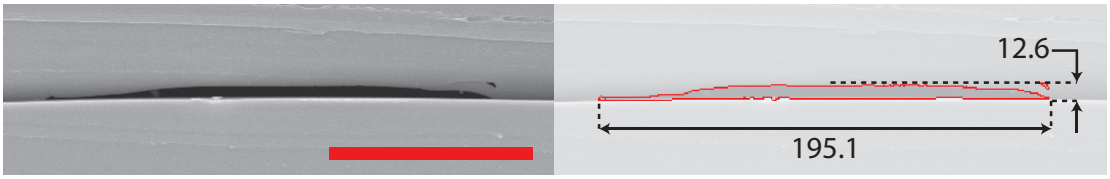

Figure 4.10: SEM image of 10 $\times$ 100 μm channel exposed at 175 mJ/cm^2. Notice the tearing in the top right of the channel. (Left) Original SEM image. (Right) SEM image with channel highlighted and dimensions added. All dimensions are in micrometers. Scale bar is 100 μm.

While most channel shapes were similar to those shown in Fig. 4.6(d), some aspect ratio channels (most notably the narrow but tall channels, such as the 50 $\times$ 50 μm channels) showed sharp corners, as can be seen in Fig. 4.11. This effect may have to do with the specifics of the diffuser we used. Regardless, this

technique may not be appropriate for taller channels.

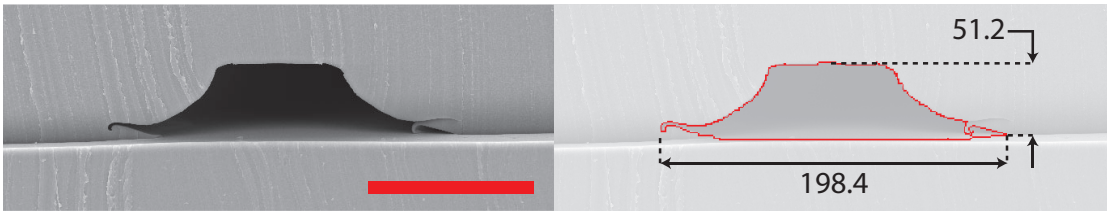

Figure 4.11: SEM image of 50 $\times$ 50 μm channel exposed at 150 mJ/cm^2. Notice the sharp corners at the top of the channel. (Left) Original SEM image. (Right) SEM image with channel highlighted and dimensions added. All dimensions are in micrometers. Scale bar is 100 μm.

In summary, this method provides a very simple fabrication process that is nearly as easy as standard photolithography with a silicon wafer. However, there is significant channel widening, and glass wafers typically cost about an order of magnitude more than silicon wafers.

4.5.6 Inflated PDMS membrane

When successful, this method produced satisfactory microchannels; however, the method quite often failed to produce channels at all. In contrast to Hongbin et al.[31], we found little to no effect from increasing the pressure of the inflated membrane. This discrepancy may be due to the thickness of the inflated membrane. Hongbin et al. report a membrane of about 20 μm from spincoating at 1000 rpm, but in our attempts spinning at 1000 rpm created membranes of much greater thickness (approximately 75 μm). With a thicker membrane, we would require much larger variations in pressure to see noticeable changes in deflection. While experimenting with higher pressures, we occasionally plastically deformed the thin membrane, revealing one failure mode of this technique.

We additionally tried spincoating at higher speeds to achieve thinner membranes (2000 rpm to fabricate an approximately 40 μm thick membrane), but encountered other problems. With a thinner membrane, we noticed a tendency for the channels to collapse during curing. This effect is even more pronounced in wide, tall channels. In fact, we saw channel collapse in wide, tall channels even with the thicker membrane, as can be seen in Fig. 4.12.

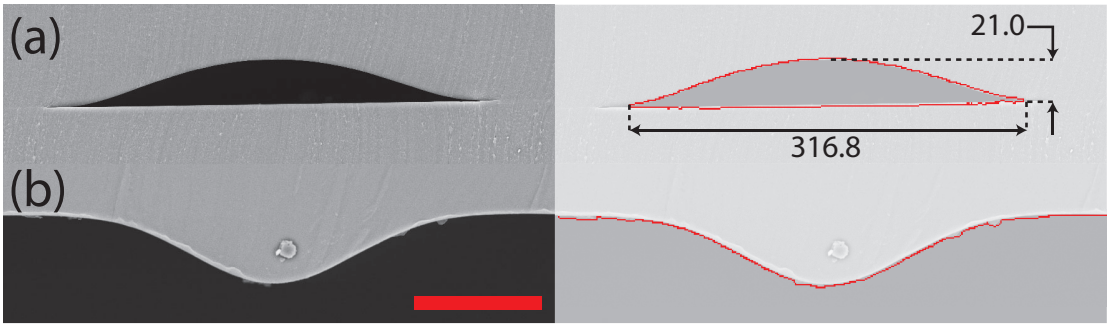

Figure 4.12: SEM images of 250 μm wide channels inflated at 5 psi. (a) 10 μm mold produced normal channels. (b) 50 μm mold produced collapsed channels. Consequently, this image does not include a bottom layer of PDMS. (Left) Original SEM image. (Right) SEM image with channel highlighted and dimensions added. All dimensions are in micrometers. Scale bar is 100 μm.

As noted previously, the channel height is partially a function of the channel width, so control over channel dimensions is limited. However, this relationship can be exploited as a benefit; one can create a single channel of varying height simply by varying the channel width.

In summary, this method is capable of producing channels of an appropriate shape, and has the interesting ability to create a single channel of variable height. However, the fabrication process involves many steps, is dependent on a variety of parameters, and is prone to frequent failure for more aggressive channel dimensions.

4.5.7 Secondary spin coating

Secondary spin coating is a very straightforward strategy to achieve rounded microchannels. We were unable to consistently achieve the 10 μm tall channels, as the secondary spin coating step effectively covered them. The 50 μm channels were all successfully fabricated, and produced channels with acceptable cross-sectional geometry.

However, there are two major drawbacks. First, the orientation and location of the microchannels with respect to the wafer are important. Channels aligned radially (i.e., whose long dimension passes through the wafer center) will be mostly symmetric, but those aligned tangentially will by asymmetric. The asymmetry increases with distance from the center of the wafer. This effect can be seen in Fig. 4.13.

The second drawback is a significant channel widening. It is typical for channel widths to grow hundreds of microns upon secondary spin coating. For example, the final width of the nominally 50 $\times$ 50 μm channel spun at 1000 rpm was over 600 μm. Note also that the height of the channels will change upon secondary spincoating, although this fact can be accounted for in the design.

In summary, this method is able to produce microchannels of the correct shape, but requires careful consideration of channel orientation, location, and spacing to create a functional microfluidic network.

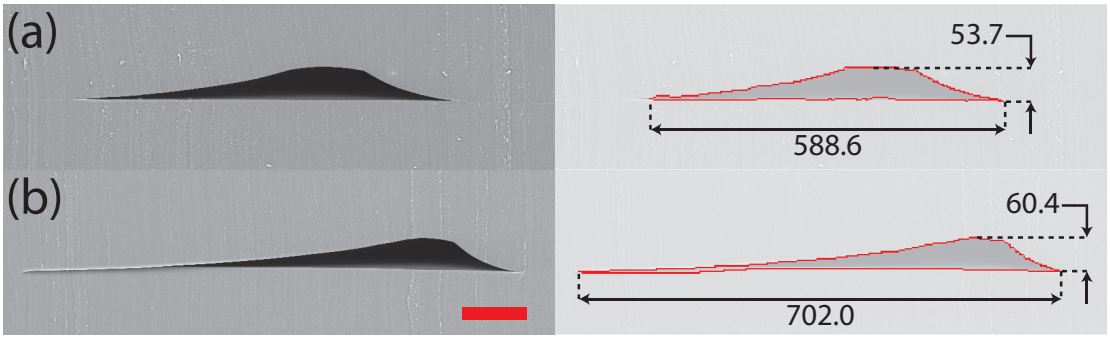

Figure 4.13: 50 μm tall channels with a secondary spin coating at 4000 rpm. (a) 100 μm wide channel (nominally), near the center of the wafer. (b) 250 μm wide channel (nominally), offset from the center of the wafer. Notice the increasing assymmetry with distance from the center of the wafer. (Left) Original SEM image. (Right) SEM image with channel highlighted and dimensions added. All dimensions are in micrometers. Scale bar is 100 μm.

4.6 Conclusions

As to which fabrication strategy is best for creating rounded microchannel, the answer is largely qualified; different strategies have different benefits and limitations. We have attempted to collect our findings in Table 4.4, ranking each fabrication method on a number of metrics, which are described below.

It should be noted that all methods were able to produce channels of the appropriate shape, although to varying degrees. The quality of the channel shape is quantified by each channel's performance in a valve, but here we rank shape as a binary "good" or "bad" depending on whether or not there was complete channel closure. Resolution is quantified by the smallest channel heights and widths achieved when trying to fabricate 10 $\times$ 50 μm channels. If we were unable to fabricate 10 $\times$ 50 μm channels with a given method, we then used the smallest dimensions achieved in any successful channels. Specifically, all meth-

ods produced 10×50 μm channels except for the inflated PDMS membrane method, in which case we used the smallest dimensions from the 10×250 μm channels (as we were likewise unable to fabricate 10×100 μm channels). Dimension mapping is reported as an average deviation from target channel dimensions, as described in Fig. 4.7. Fabrication time lists both the active time (i.e., time that requires the user to be present) and the total time. We assume four hours for PDMS curing and six hours for wafer silanization and mold baking. Fabrication difficulty and process prohibitiveness are ranked qualitatively based on our experience with the various fabrication methods and the infrastructure, safety precautions, etc. required.

In terms of ultimate resolution and dimension mapping, the reflow of positive photoresist performed best by far. However, this method has the drawbacks of a complicated fabrication process, high sensitivity to process parameters and disturbances, the use of dangerous chemicals, and the need for expensive infrastructure. On the other end of the spectrum is 3D printing. This method is extremely easy, fast, safe, and requires almost no user skill. However, resolution is limited, and channels often do not print at the dimensions specified in the design file.

The other methods each have their own strengths and weaknesses. Exposing through the backside of a glass wafer yields resolutions and controllability approaching that of reflowing positive photoresist, but allows one to work with much easier, safer, and more robust negative photoresists (such as SU-8). However, channel shape is not always ideal, there is significant channel widening,

and glass wafers are significantly more expensive than silicon wafers. Using an inflated PDMS membrane as a mold enables the creation of individual channels with varying heights, but the fabrication process is long and inconsistent, and molds are somewhat fragile. Secondary spin coating is extremely simple and produces a very robust mold, but channel dimensions grow significantly and, unless the channels are placed very deliberately, the channels become asymmetric.

We summarize the major factors affecting channel height, width, and degree of rounding below in Table 4.5, along with a high-level comparison of fabrication times in Table 4.6.

Fabrication strategy	Channel shape	Resolution	Dimension mapping	Fabrication time	Fabrication difficulty	Process prohibitiveness
		Evaluation parameter				
Control	×	11 μm (height) 60 μm (width)	2 μm (height) −4 μm (width)	45 min (active) 7 hr (total)	Moderate	Moderate
+PR	✓	12 μm (height) 36 μm (width)	2 μm (height) −1 μm (width)	85 min (active) 11.5 hr (total)	Difficult	High
3DP	✓	12 μm (height) 116 μm (width)	−3 μm (height) 137 μm (width)	30 min (active) 9 hr (total)	Easy	Low
BSE	✓	9 μm (height) 119 μm (width)	1 μm (height) 145 μm (width)	45 min (active) 7 hr (total)	Moderate	Moderate
IPM	✓	17 μm (height) 311 μm (width)	8 μm (height) 58 μm (width)	90 min (active) 17.5 hr (total)	Moderate	Moderate
SSC	✓	10 μm (height) 327 μm (width)	2 μm (height) 403 μm (width)	55 min (active) 7 hr (total)	Moderate	Moderate

Table 4.4: Performance of the different fabrication strategies for different evaluation parameters. Channel shape: a binary "good" or "bad" based on whether or not the given channel could be completely closed off when incorporated in a microfluidic valve. Resolution: these are the smallest widths and heights achieved when attempting to fabricate 10 × 50 μm channels (or the smallest successfully fabricated channel), rounded to the nearest micrometer. Dimension mapping: values obtained by averaging width and height deviation from the photomask or print file (as in Fig. 4.7) and rounding to the nearest micrometer. Fabrication time: we assume four hours for curing of PDMS and six hours for silanization of wafers and baking of 3D-printed molds.

Method	Variable	Major factors
Control	Channel height	• Type of photoresist used • Photoresist spin coat speed
	Channel width	• Width of photomask
	Degree of rounding	n/a
+PR	Channel height	• Type of photoresist used • Photoresist spin coat speed • Reflow temperature and time
	Channel width	• Width of photomask • Reflow temperature and time
	Degree of rounding	• Reflow temperature and time
3DP	Channel height	• Channel height (and width) defined in print file • Printer and print material used
	Channel width	• Channel width (and height) defined in print file • Printer and print material used
	Degree of rounding	• Channel height and width defined in print file • Printer and print material used
BSE	Channel height	• Type of photoresist used and spin coat speed • Exposure energy
	Channel width	• Width of photomask • Thickness of glass wafer • Exposure energy • UV light source optical profile (collimated vs. diffuse light)
	Degree of rounding	• Thickness of glass wafer • Exposure energy • UV light source optical profile (collimated vs. diffuse light)
IPM	Channel height	• Type of photoresist used and spin coat speed • Channel width (of PDMS device used as mold) • Membrane thickness (of PDMS device used as mold) • Inflation pressure (of PDMS device used as mold)
	Channel width	• Width of photomask
	Degree of rounding	• Channel width (of PDMS device used as mold) • Membrane thickness (of PDMS device used as mold) • Inflation pressure (of PDMS device used as mold)
SSC	Channel height	• Type(s) of photoresist used and spin coat speed(s)
	Channel width	• Width of photomask • Type of photoresist used for second spin coat • Second photoresist spin coat speed • Channel height (defined from first photoresist spin coat) • Microchannel orientation
	Degree of rounding	• Channel width (of PDMS device used as mold) • Type of photoresist used for second spin coat • Second photoresist spin coat speed • Channel height (defined from first photoresist spin coat) • Microchannel orientation

Table 4.5: Summary of the major factors affecting the key microchannel variables for each method. Notice that a single factor often affects multiple variables.

Method	Channel height	Active time	Total time
Control	10 μm	45 min	6.75 hr
	50 μm	55 min	7 hr
+PR	10 μm	85 min	11.5 hr
	50 μm	n/a	n/a
3DP	10 μm	30 min	8.5 hr
	50 μm	30 min	9.5 hr
BSE	10 μm	45 min	6.75 hr
	50 μm	55 min	7 hr
IPM	10 μm	90 min	17.5 hr
	50 μm	100 min	17.75 hr
SSC	10 μm	55 min	7 hr
	50 μm	65 min	7 hr

Table 4.6: Summary of fabrication time to make masters. Values are approximate. We assume the starting point is a complete CAD model, and the finishing point is a ready-to-use mold (i.e., post silanization). For the lithgraphic techniques, we include the time required to fabricate a photomask. For the total time, we assume 6 hours for silanization of wafers and baking of 3D-printed molds.

5

Microfluidic Multiplexing for Soft Robotics

Soft robots are notoriously difficult to control; untethered soft robots rely on rigid control components, while tethered soft robots either have limited functionality or require a large, obtrusive tether. In this chapter, we propose the

introduction of multiplexing to soft robotic control to increase complexity while minimizing the reliance on off-board components. Multiplexing of pneumatic and hydraulic lines has been used in the microfluidics community to enable increased functionality, but its utility has been restricted to systems that operate at low pressures and low flow rates. In this chapter, we improve upon microfluidic multiplexing to make it suitable for soft robotic applications, and demonstrate its functionality by controlling a large array of soft actuators with just a few control inputs. In doing so, we drastically increase the achievable complexity of tethered soft robots, and contribute to the development of soft control systems for untethered soft robots.

5.1 Motivation

A grand challenge of soft robotics is the demonstration of a fully soft, untethered, highly functional robot. The majority of fully soft robots are tethered, relying on off-board components for either power or control, or both[98,99,15,101,87,88]. Almost all untethered systems are not fully soft, as they incorporate rigid elements such as batteries, circuit boards, or mechanical valves[112,5,61,74,11]. The authors are aware of only one example of a fully soft, untethered robot: the Octobot[128]. While certainly a very impressive demonstration of highly integrated fabrication, and a significant step forward for the field, the Octobot is only able to perform one preprogrammed motion. As such, the field is still in search of its first example of a fully soft, untethered robot capable of diverse behaviors.

The soft robotic spider presented in an earlier chapter is an example of a complex system capable of diverse behaviors[88]. Of course, this robot is tethered, relying on many hydraulic lines which were controlled off-board. It should be noted, however, that the fabrication process for MORPH systems may be of particular note due to the ease with which it can accommodate microfluidic circuitry. The techniques to fabricate rounded microchannels presented in the last chapter are all compatible with that process. However, to make a microfluidic circuit capable of any degree of control, microfluidic valves must be incorporated. As such, this chapter examines these microfluidic valves in detail, at times relying heavily on the conclusions reached in the last chapter regarding microchannel fabrication.

5.1.1 Robot subsystem development

Any autonomous robot has fundamental subsystems that include structure, actuation, sensing, power, and control. The structural subsystem is essentially the body of the robot, and ties together the other subsystems. The actuation subsystem is what enables the robot to move. Arguably the majority of research in soft robotics to date has been in developing muscle-like actuators; as such, there are many examples[70,34,51,134,30,97,100]. Most of these soft actuators are fluidic, in that they are powered either hydraulically or pneumatically. The sensing subsystem allows the robot to receive input from its environment. There are myriad demonstrations of soft sensors as well[120,47,41,42,25,58]. The power subsystem provides the energy with which the actuators perform work. Although

research in this area has been overshadowed by developments in actuators and sensors, there are a number of power subsystems for soft robots[103,126,73]. The control subsystem is situated between the power and actuation subsystems (perhaps with input from the sensing subsystem, if there is feedback) to dictate how and when power is delivered to the actuators. Of all the subsystems, soft controllers are perhaps the least developed[113].

Indeed, one of the central motivations for developing soft robots is that they exhibit a kind of mechanical intelligence in which the body or structure reacts organically to the environment, obviating the need for traditional control feedback loops that rely on precision sensing and actuation. Two examples of such systems were examined in the opening chapters of this dissertation. However, even if feedback control may be deemed unnecessary in some (or even all) soft robots, the challenge of distributing energy to the system's actuators remains.

5.1.2 Fluidic control for soft robots

When implementing a control subsystem for a soft robot, we must carefully consider the design of the full system. A large percentage of soft actuators are powered by pressurized fluid; as such, there are many reasons why we may want fluidic control for soft robots. Using the same medium for the power, control, and actuation subsystems lends itself to more straightforward subsystem integration and overall simplicity. A single medium also allows the robot designer to blur the boundaries between various subsystems, enabling greater design freedom. For example, a single pressurized fluidic line may simultaneously affect the

behavior of a different fluidic line (as part of the control subsystem) and cause a downstream component to bend or change shape (as part of the actuation subsystem). This type of subsystem fluidity is much harder (or potentially impossible) to accomplish with mismatched media. While the default control subsystems are electrical (e.g., microcontrollers and computers), there are applications in which we may want to avoid electricity, such as with robots that operate underwater. Additionally, there are many situations in which we may want to offload as much low-level control to the mechanics of a system as possible. Finally, a fluidic control subsystem may be composed of microfluidic valves that are significantly smaller and less expensive than the electromechanical solenoid valves that are typically used to interface between an electrical control subsystem and a fluidic actuation subsystem.

There is precedent for fluidic control systems. "Fluidics" was an active research area in the latter half of the twentieth century as a potential method of control that was impervious to radiation and electromagnetic pulses. The United States government was particularly interested in this technology for its aerospace and military applications[27,38]. However, interest waned with the rise of the silicon revolution as electrical devices began to drastically outperform pneumatic and fluidic control systems.

5.1.3 Tethering

Given that not all subsystems have been developed at the same rate, many soft robots are tethered to allow off-board power and control. Tethered systems

may be seen as stepping stones to future untethered robots or as final systems in their own right. Regardless, we should still seek to minimize the influence of tethers on the behavior of the system. That is, we should strive for small tethers with as few lines as possible over large, obtrusive tethers composed of many lines. A physically large tether may pull on a robot, introducing undesirable forces and moments; this effect becomes more pronounced as size decreases. Furthermore, abrupt changes in mechanical properties at interfaces are a common source of failure in soft robotics[5,67]; as such, a complex tether that relies on many parallel, independent connections will be significantly less robust than a simpler tether with only a few connections.

5.1.4 The potential of multiplexing for soft robots

We believe that the dual challenges of underdeveloped soft control subsystems and unmanageable tethers can be addressed simultaneously. In this chapter, we propose that the functionality of soft robots may be enhanced through a soft control subsystem that exploits microfluidic multiplexing. A demultiplexer enables control over a large number of outputs with only a few inputs, and can be embedded within the body of a soft robotic system. Such an architecture minimizes the size and complexity of any tether by drastically reducing the number of control lines required to address all of the system's actuators. By moving more of the control subsystem on-board, microfluidic multiplexing brings the field closer to fully soft, untethered, highly functional robots.

5.2 Microfluidic Multiplexing

Demultiplexers are most commonly seen in the realm of electronics, although some have been demonstrated within microfluidics. Compared to their electrical analogs, microfluidic demultiplexers presented in the literature exhibit less favorable input–output scaling. Additionally, these demultiplexers have only been demonstrated in low pressure, low flow rate systems. The microfluidic demultiplexer presented below improves upon that which has been reported previously, in that it demonstrates the scaling relationship that has been shown in electrical demultilplexers, and can accommodate the pressures and flow rates required to control soft actuators.

5.2.1 Principle of operation

A demultiplexer is a device that allows a small number of inputs to select one among a much greater number of outputs (see Fig. 5.1). Each input toggles the state of every output, ensuring that half of the outputs are open and half of the outputs are closed. The first input ensures inverse states for the first and second halves of the outputs. The second input again ensures inverse states for half of the outputs, but does so by keeping the first and third quarters of the outputs in the inverse state of the second and fourth quarters. Later inputs select smaller and smaller groupings of outputs (eighths, sixteenths, thirty-seconds, etc.) until the groupings consists of single alternating outputs. By selecting which half of the outputs are controlled by a given input, n outputs can be con-

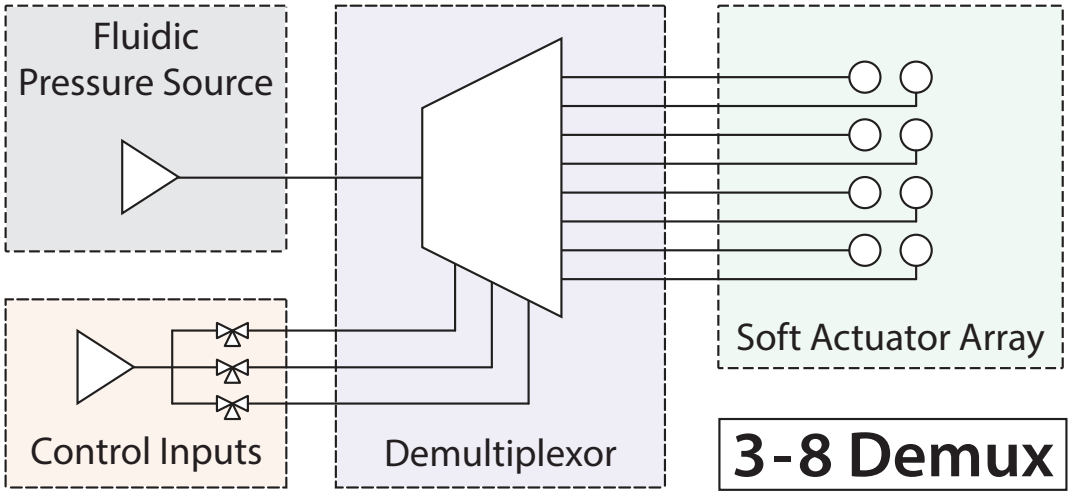

Figure 5.1: Demultiplexer principle of operation. In this work, we use a demultiplexer to reduce the number of control lines required to address a soft actuator array. Generally, a demultiplexer uses n inputs to select one among 2^n outputs.

trolled with just $log_2 n$ inputs. This scaling has been demonstrated repeatedly in the electrical domain.

5.2.2 The microfluidic approach to multiplexing

The microfluidic demultiplexer presented in this chapter was inspired by earlier designs presented in the literature[109], but with notable and important differences. In that earlier work, each "input" was in fact two independent microfluidic channels which were externally constrained to be in inverse pressurization states. That is, while one was pressurized, the other was manually depressurized. As such, the number of inputs required to control n outputs was shown to be $2\,log_2 n$, twice that of electrical demultiplexers.

The multiplexing scheme in this chapter more closely resembles the scaling

laws of the electrical domain in that the number of inputs required to control n outputs is just $log_2 n + 1$. We accomplish this nearly two-fold reduction in the number of required control inputs compared to previously reported microfluidic demultiplexers by explicitly enforcing the inverse pressurization state requirement in the demultiplexer itself rather than doing so artificially through external manipulation. The fundamental difference is a single line that acts as both a flow channel and a control channel simultaneously. The details of this design choice are discussed in the following section.

5.2.3 Design details

Referring to Fig. 5.2, the outputs $O_0 - O_7$ are all connected to a single input channel on the flow layer, denoted "Static Flow" (SF). This channel is set to a single static pressure (P_{SF}), and does not change. A separate network of interconnected channels on the flow layer is connected to a distinct input, denoted "Static Control" (SC). The input to this line is also set to a static pressure (P_{SC}, with $P_{SC} > P_{SF}$). Each branch of SC transitions from the flow layer to the control layer by means of a microfluidic via (depicted as purple circles in Fig. 5.2). The continuation of these channels on the control layer (SC_2, SC_1, and SC_0) then cross under the output channels of the SF line ($O_0 - O_7$). Where their widths increase, these channels behave as valves; where their widths remain small, these channels do not affect the flow of the channels above them (refer back to Fig. 5.4 and consider cases of $w_c - w_f << 0$). Finally, there are the channels denoted "Variable Control" (VC), whose pressure may be tog-

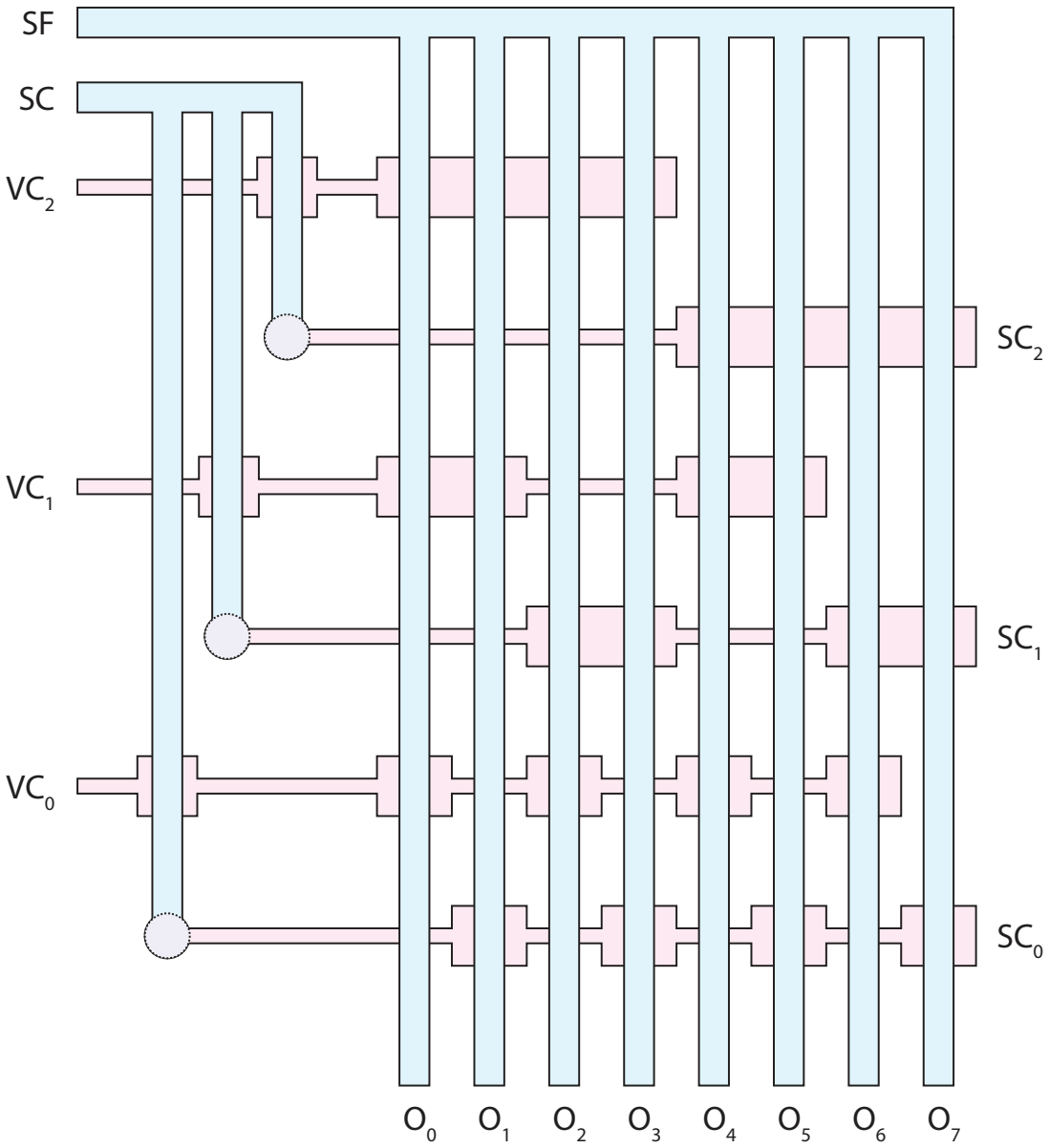

Figure 5.2: Demultiplexer design schematic. SF and SC lines are always pressurized, with the pressure of the SC line greater than that of the SF line. The three VC lines may either be pressurized (to a pressure greater than that of the SC line) or vented to atmospheric pressure to select among the eight outputs. This example design demonstrates control of eight outputs with three variable inputs (plus one static input). SF: Static Flow, SC: Static Control, VC: Variable Control, O: Output.

gled between atmospheric pressure (established by using a three-way valve on each VC channel) and a given high pressure (P_{VC}, with $P_{VC} > P_{SC}$). Each VC channel behaves as a valve (or set of valves) that affects half of the outputs, but also consists of an additional valve that closes a branch of the SC channel, opening the other half of the outputs. That is, we couple the pair of microfluidic lines that define a single input by using a valve as a logical NOT gate.

Considering the three (variable) input, eight output demultiplexer in Fig. 5.2, the default state is all inputs low, corresponding to $[VC_2\ VC_1\ VC_0] = [0\ 0\ 0]$. In this state, SC_2 closes $O_4 - O_7$, SC_1 closes O_2, O_3, O_6, and O_7, and SC_0 closes O_1, O_3, O_5, and O_7. Consequently, O_0 is selected. If VC_0 is set high (giving [0 0 1] for the input state), the first valve on VC_0 closes SC_0, such that O_1, O_3, O_5, and O_7 are no longer closed (at least, not by SC_0). Downstream, VC_0 closes O_0, O_2, O_4, and O_6. Consequently, O_1 is selected. Any output may be selected with the correct combination of variable inputs. In fact, the input state vector $[VC_2\ VC_1\ VC_0]$ is exactly the selected output in binary notation (e.g., [1 0 1] selects O_5).

5.2.4 Demultiplexer fabrication

The demultiplexer was made from three layers of elastomer. The topmost layer (the "flow layer") was fabricated from PDMS (Sylgard 184, Dow Corning) mixed in the standard 10:1 ratio and poured over a mold that was 3D-printed on an Objet30 Scholar 3D printer (Stratasys Ltd.) using VeroWhite material. The middle layer (the "control layer") was fabricated from MED4-4220 (NuSil

Technology) mixed in the recommended 1:1 ratio and poured over a silicon wafer mold fabricated via traditional soft lithography. The bottommost layer (the "base layer") was fabricated from Sylgard 184 poured on an unpatterned silicon wafer. The three layers were bonded with oxygen plasma treatment.

In the previous chapter[6], we compared fabrication strategies for creating rounded microchannels. In this work, we opted to use 3D printing because we have relatively large channel sizes, and prioritize iteration time and fabrication simplicity over ultimate microchannel resolution.

5.3 Valve Design and Characterization

At the heart of any demultiplexer is a switch that can toggle an output between two states. In electronics, that switch is a transistor. In microfluidics, that switch is a valve that either stops flow in a microchannel, or allows flow to proceed uninhibited. The microfluidic valve presented in this paper is an adaptation of the first microfluidic valve presented by Unger et al.[118]

5.3.1 Design overview

A single valve consists of two perpendicularly oriented microchannels, offset slightly in the vertical direction so that they are separated by a thin membrane (see Fig. 5.3A). When one microchannel is pressurized, it expands, deforming the surrounding elastomer, and causing the membrane to deflect into the other microchannel and impede the flow (see Fig. 5.3B).

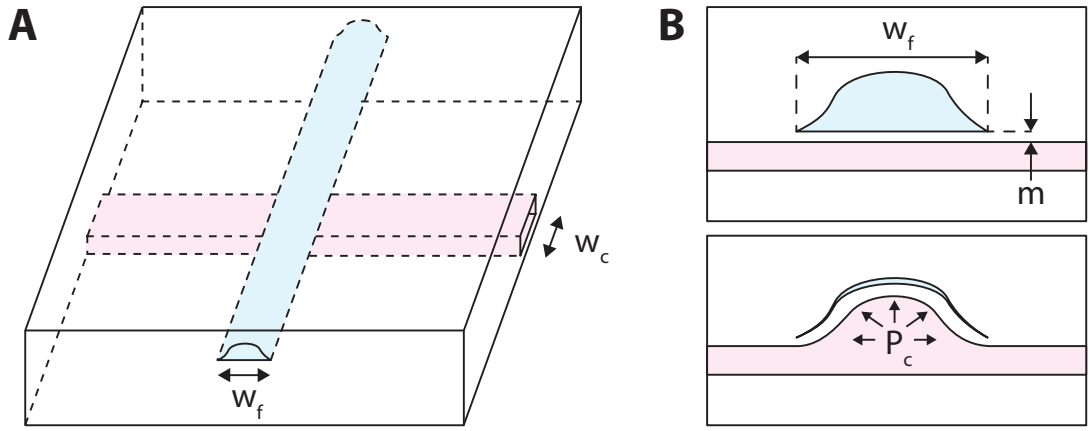

Figure 5.3: Principle of operation of a microfluidic valve. (A) A valve consists of two perpendicular microchannels offset slightly in the vertical direction. When the "flow" channel (blue) is above the "control" channel (pink), the valve is designated as "push-up". w_f: width of flow channel. w_c: width of control channel. **(B)** As the control channel is pressurized, it expands, deflecting the elastomeric membrane into the flow channel. P_c: pressure of control channel. m: membrane thickness.

We call the "flow" channel the microchannel that carries the fluid whose flow is modulated by the valve, and we call the "control" channel the microchannel that enacts the modulation. In our configuration, the control channel is always below the flow channel, in a configuration called a "push-up" valve. Others have shown[22] that this configuration is preferable to the alternative "push-down" configuration, in which the control channel is above the flow channel. We have shown in the previous chapter[6] that the shape of the flow channel is critical to ensure full valve closure, and that various fabrication strategies may be employed to achieve acceptable channel shapes, subject to design requirements. In this chapter, we use soft lithography to fabricate the control layer mold and 3D printing to fabricate the flow layer mold.

5.3.2 Analytical modeling vs. experimental characterization

Analytical models of microfluidic valves have been presented in the literature[40,22]. However, these models make assumptions about the profile of the flow channel that do not apply to the valves presented here (e.g., that the profile is parabolic). Modifying these analytical models to accommodate our valve geometry would quickly become intractable. As such, we opted to characterize our valves experimentally.

Valve characterization consisted of a variable sweep of both channel sizes and membrane thicknesses. By systematically altering individual variables, we determined the control pressure (P_c) required to stop a given flow pressure (P_f) as a function of control channel width (w_c), flow channel width (w_f), and membrane thickness (m) (see Fig. 5.3A and B).

We found that while the widths of the flow and control channels have a slight effect on the valve closing pressure, the membrane thickness more strongly influences valve behavior (see Fig. 5.4). This decoupling is fortuitous in that system requirements (such as actuator pressure and actuation frequency) can drive channel geometry while valve behavior can be tuned simply by altering the membrane thickness.

5.3.3 Influence of material properties

Due to the strong influence of the membrane on valve behavior, we sought to understand the contribution from material choice in addition to geometry.

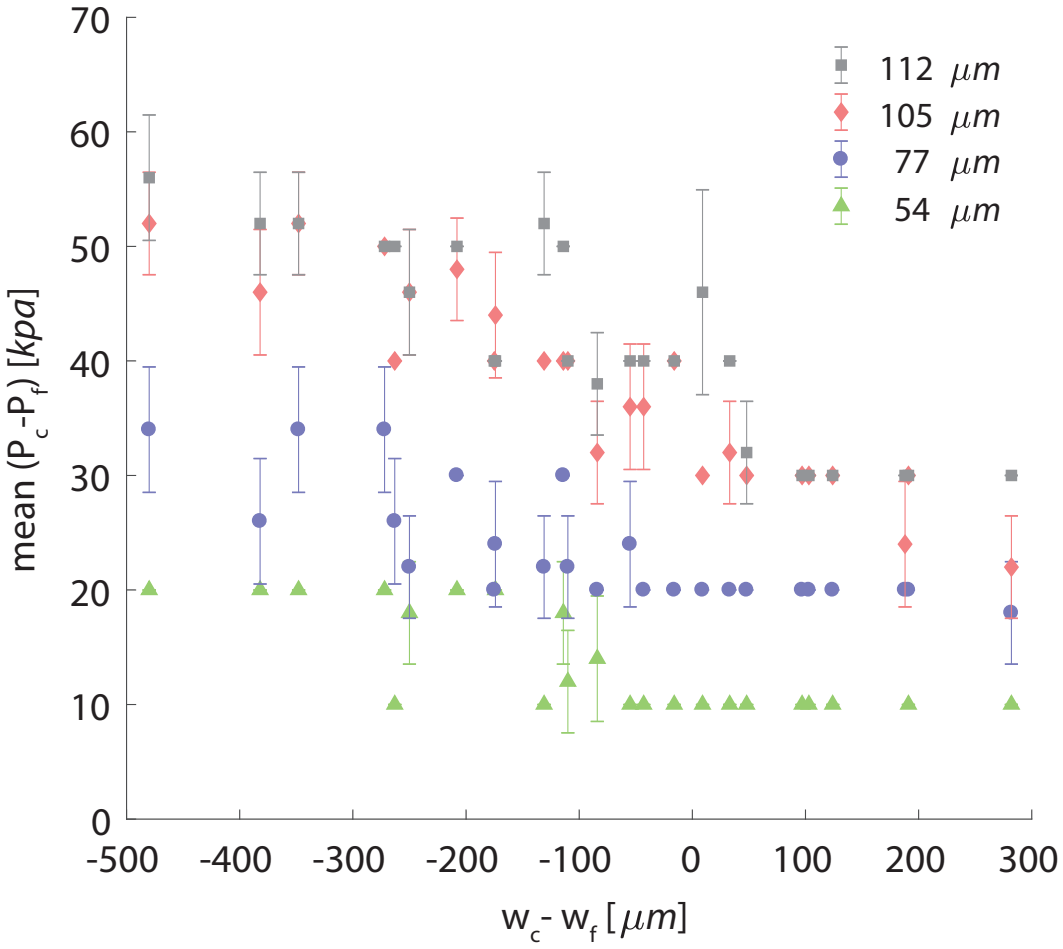

Figure 5.4: Valve characterization. For four different membrane thicknesses (112, 105, 77, and 54 micrometers, corresponding to the gray, pink, purple, and green markers, respectively), we characterize the average difference in pressure between the control channel and the flow channel required to close the valve (i.e., mean$(P_c - P_f)$) as a function of the difference in channel width between the control channel and the flow channel (i.e., $w_c - w_f$). P_f: pressure of flow channel. Membrane material is MED4-4220 for the above data. Each data point represents five trials.

While most microfluidic systems are fabricated from Sylgard 184 (Dow Corning), we found this material somewhat constraining, especially in that it is a relatively stiff elastomer, with a durometer of Shore A 44[37]. We investigated the use of an alternate elastomer, MED4-4220 (NuSil Technology), which has a durometer of Shore A 17[71]. While preliminary valve testing was done with membranes made from Sylgard 184, we repeated the valve characterization described above with membranes made from MED4-4220 and found significantly more robust performance.

5.3.4 Testing setup and equipment

Valve characterization was performed with a compressed air line regulated with a manually operated relieving pressure regulator. Pressures were recorded using manual pressure gauges (0-100 kPa, minimum gradation of 2 kPa; 0-400 kPa, minimum gradation of 10 kPa). Membrane thicknesses were determined by measuring cross-sections with a confocal microscope (Olympus LEXT OLS4000, Olympus Corporation).

We made a set of 25 valves by fabricating five flow channels and five control channels which were bonded together. We repeated this process for four different membrane thicknesses, yielding a total of 100 valves. Each valve was tested at five operating points (p_f = 20, 40, 60, 80, or 100 kPa), resulting in 500 distinct data points of valve characterization data. To test a valve, we first pressurized a flow channel to one of the five operating points. The output of the flow channel was connected to a tube submerged underwater, so that bubbles were

produced. We then gradually increased the pressure in the control channel until the bubbles stopped completely, indicating full valve closure.

5.4 Soft Actuator

The demultiplexer discussed above has been designed to operate at a scale large enough to be relevant to soft robotics. The test of such a system is in its ability to operate functional actuators; for such a demonstration, we have chosen to use tri-chambered pneumatic bending actuators[105]. While the demultiplexer presented here could be adapted to any of a wide variety of soft fluidic actuators (and was partially sized as such), we have specifically chosen these actuators for three reasons. First, the actuators are small enough that we can fabricate a large array in a small area, demonstrating the favorable scaling properties of the demultiplexer. Second, we are able to show complex motions to mirror the non-trivial microfluidic logic scheme, because the actuators each possess two degrees of freedom. Finally, these actuators demonstrate one fabrication strategy for elegant integration of actuation and control subsystems by using both molding and soft lithography.

5.4.1 Actuation modes

Each actuator is composed of three individually addressable pneumatic chambers. Because each chamber is offset from the neutral axis of the actuator, pressurizing any one chamber produces a moment which causes the actuator to

bend. By modulating the pressure in each chamber, one can produce bending in any direction. Fig. 5.5A depicts the typical bending mode of the actuator. Fig. 5.5B shows a single actuator in its unpressurized state, as well as the three states resulting from pressurizing each of the chambers individually.

5.4.2 Actuator fabrication

The actuator is fabricated by dip-coating uncured elastomer (Elastosil M 4601, Wacker Chemie) onto a set of three stainless steel pins whose position is defined by a custom laser-cut fixture. The fixture securely holds the pins in a vertical orientation. As the pins are dipped into uncured elastomer, they are coated individually. The elastomer remains on the surface of the pins as it cures due to surface tension. Further dippings continue to coat the individual pins, but also allow elastomer to bridge between the pins. After the elastomer is fully cured, the pins are removed, resulting in a single tri-chambered bending actuator.

5.5 Integrated Demultiplexer and Soft Actuator Array

As mentioned above, microfluidic multiplexing has been previously demonstrated, but not at pressures and flow rates that can drive soft actuators. With our redesigned demultiplexer and a target actuator, we built an integrated system to demonstrate the relevance of microfluidic multiplexing to soft robotics.

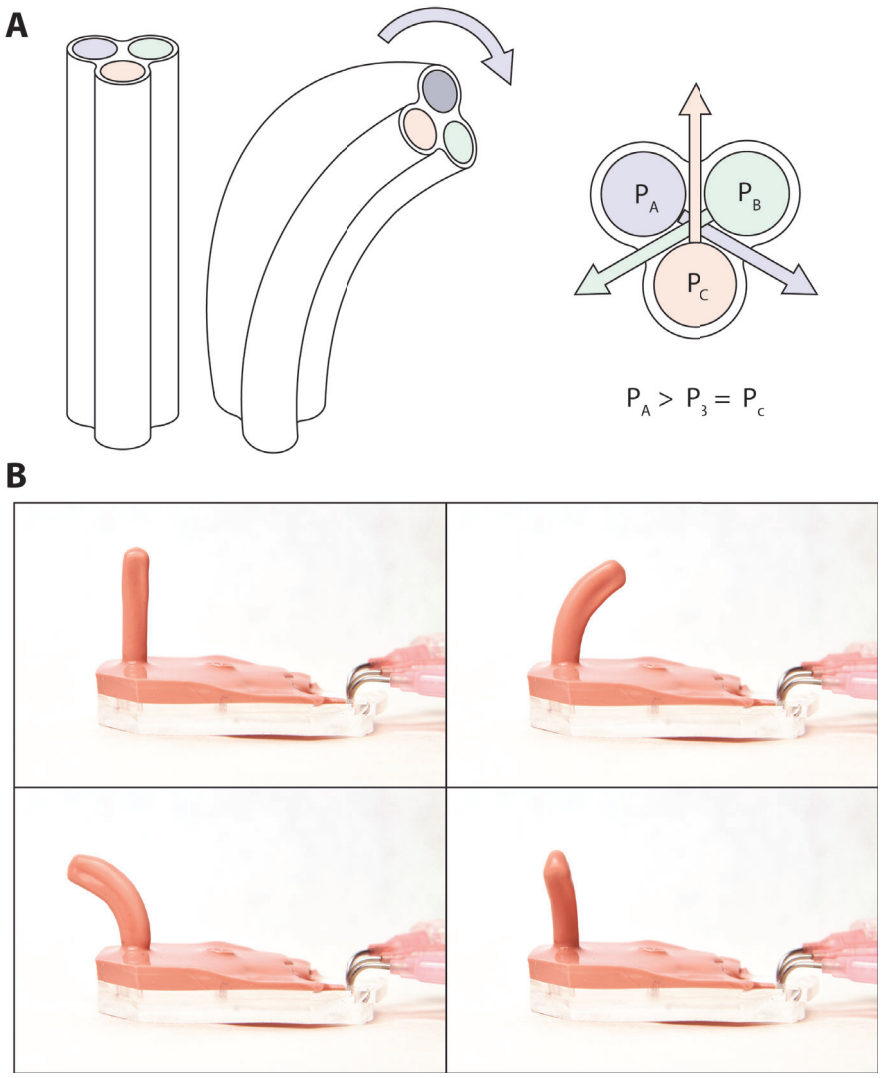

Figure 5.5: (A)Actuator principle of operation. A single actuator consists of three chambers. When any single chamber is inflated, the actuator bends towards the side of the actuator opposite the pressurized chamber. (The tops of the actuators are cut away in the image to show the individual chambers.) **(B) Actuator bending.** *Top left*: No chambers are pressurized, yielding an undeformed state. *Top right*: The front left chamber is pressurized, causing bending towards the back right. *Bottom left*: The front right chamber is pressurized, causing bending towards the back left. *Bottom right*: The back chamber is pressurized, causing bending towards the front.

5.5.1 Integration of fabrication strategies

To integrate the demultiplexer with an array of actuators, we had to address system-level concerns. The actuators exhibit a trade-off in that fewer coatings during fabrication enable a lower actuation pressure, but also pose a higher risk of failure due to a defect in a thin chamber wall. In a large array in which a single failed actuator would compromise the entire system, we prioritized robustness over a lower operating pressure.

To develop the integrated system, very few modifications to the fabrication procedure were necessary. Whereas the actuators were previously made by coating pins that were directly press-fit into their acrylic fixture, in the integrated system we inserted the pins through the top layer of the demultiplexer before they were inserted into the fixture. In this way, the elastomer that would form the actuators would drip down the pins and coat the surface of the demultiplexer as it was curing. For the specific case of the materials used in this work (i.e., Sylgard 184 for the top layer of the demultiplexer and Elastosil for the actuators), curing the elastomer used for the actuators on top of the fully cured elastomer of the demultiplexer resulted in a conformal seal. Once the actuators were cured, the pins were removed from the bottom of the top demultiplexer layer, which was then plasma bonded to the remaining demultiplexer layers.

5.5.2 Pentaradial array demonstration

In contrast to the demultiplexer schematic detailed in Fig. 5.2, we demonstrate a fully integrated system with a 4 (variable) input, 16 output demultiplexer. In this demonstration (see Fig. 5.6), five tri-chambered actuators are arranged at the vertices of a pentagon (in this system, only 15 of the available 16 outputs are used). In this configuration, we can demonstrate both clockwise and counter clockwise traveling waves, in addition to an outward radial wave.

In this demonstration, flow channels were designed to be 1000 μm wide, but in practice were 1217 μm wide. Control channels were designed to be 200 μm wide (when not part of a valve) and 1000 μm wide (when part of a valve), but in practice were 594 and 1338 μm, respectively. Thus, when not part of a valve, $w_c - w_f = -623$ μm, and $w_c - w_f = 121$ μm when part of a valve. With operating pressures of $P_{SF} = 90$ kPa, $P_{SC} = 105$ kPa, and $P_{VC} = 120$ kPa, we have $P_c - P_f = 15$ kPa or 30 kPa (based on whether the flow channel in question is connected to SF of SC, and whether the control channel in question is connected to VC or SC). With a membrane thickness of 67 μm (achieved by spin-coating elastomer on a blank wafer at 1000 rpm), we would expect (based on Fig. 1C) that for $w_c - w_f = 121$ μm (i.e., when part of a valve), $P_c - P_f = 15$ kPa or 30 kPa would be sufficient to close the valve. Similarly, we would expect (based on Fig. 1C) that for $w_c - w_f = -623$ μm (i.e., when not part of a valve), $P_c - P_f = 15$ kPa or 30 kPa would be insufficient to close the valve. Indeed, this is what we found in the demonstration, corroborating the results of the valve

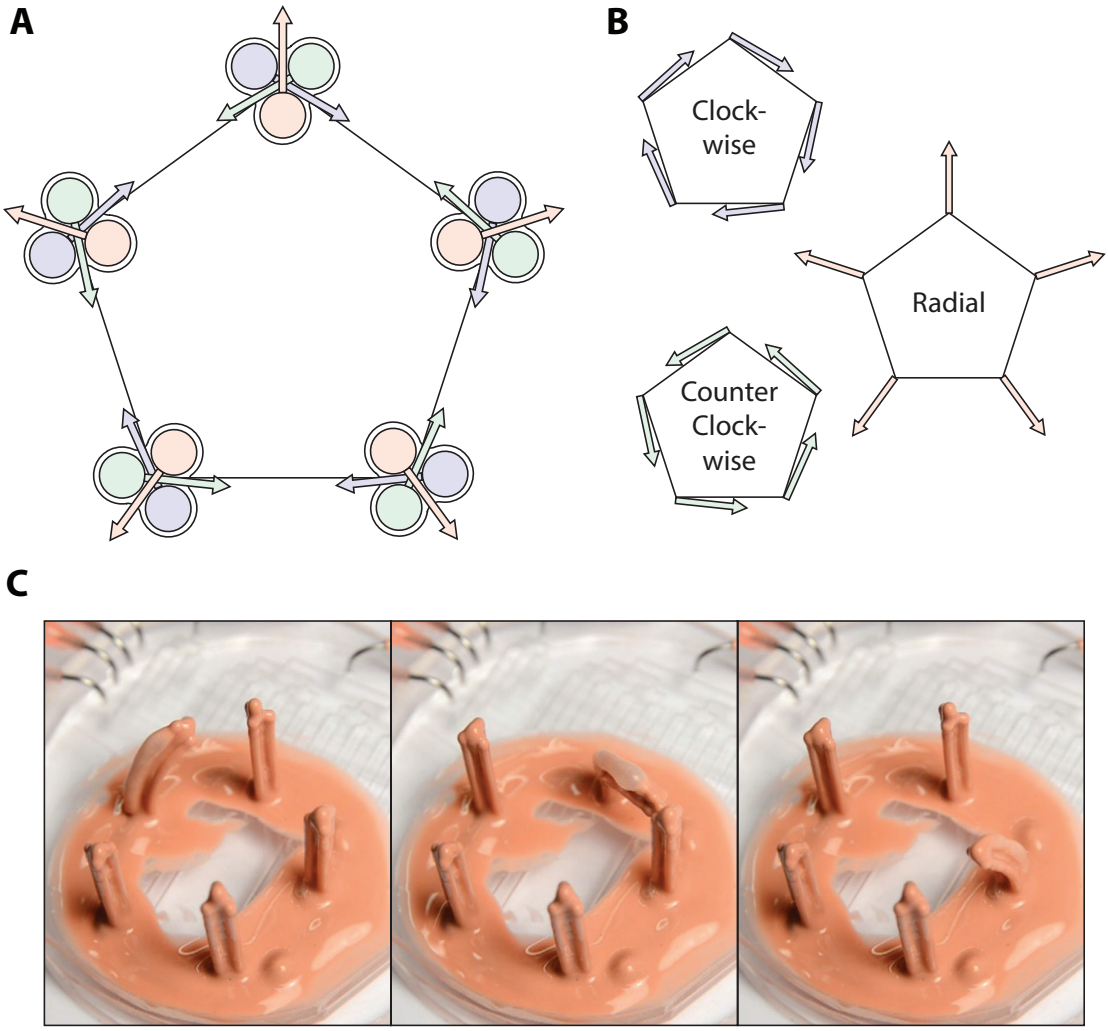

Figure 5.6: Multiplexed pentaradial soft actuator array (A) A tri-chambered actuator is placed at each vertex of a pentagon, aligned so that the actuator can bend along the edge of the pentagon. **(B)** Sequential actuation of the five tri-chambered actuators allows clockwise, counter clockwise, and radial actuation patterns.**(C)** Images of the fabricated radial array during the first three states of a clockwise traveling wave.

characterization.

5.6 Conclusions

Many advances in the field of soft robotics have revolved around sensors and actuators. Developments in soft control subsystems, in contrast, have been significantly limited. In this chapter, we proposed a microfluidic multiplexing architecture that suggests one possible path forward for soft control systems.

While microfluidic multiplexing has been demonstrated previously, there are three distinct differences presented in this chapter. First, we use a multiplexing scheme that much more closely resembles the architecture of electrical demultiplexers, decreasing the number of required control channels by a factor of two compared to earlier microfluidic demultiplexers presented in the literature. We are able to demonstrate such drastic reductions by taking advantage of the shared media (i.e., fluid) between the actuation and control subsystems, a feat that would be much more challenging with mixed media subsystems (e.g., fluid actuation and electrical control). Second, the system size is scaled to be able to accommodate much higher pressures and flow rates, bringing microfluidic multiplexing into relevance for soft robotics. Finally, we introduce a new membrane material to accommodate the higher pressures and flow rates that are required in a scaled-up system.

We demonstrate the functionality and applicability of our demultiplexer by controlling a large array of tri-chambered actuators. Beyond this demonstration,

we anticipate that such a multiplexing scheme will be highly relevant for tethered soft robotic systems that seek to minimize the effect of a tether. For example, microfluidic multiplexing may be appealing to surgeons who need to control a large number of degrees of freedom in a laparoscopic tool, and yet only have a laparoscopic port of a limited size for the tether.

In other scenarios, users may desire even more on-board control. We turn next to fluidic logic circuits that perform digital computation, bringing the field ever closer to complex autonomous soft robots.

6

Fluidic Logic Components and Circuits

In the preceding chapters, we examined strategies to fabricate rounded microchannels (with the prospect of microfluidic valves always a constant consideration), as well as one implementation of microfluidic valves in a multiplexing scheme that controlled an array of soft robotic actuators. We turn now to the next steps in developing a system of fluidic logic for soft robotics. Having con-

sidered microchannel fabrication and valve design, we look to other fundamental building blocks of fluidic circuits.

6.1 Governing equations and assumptions

Before examining the building blocks of a system of fluidic logic in detail, we must appreciate the relevant variables and assumptions. Beginning with the Navier–Stokes equation, the fundamental starting point of all fluid dynamics problems, we make a number of assumptions to reduce the problem to that defined by the Hagen–Poiseuille equation. After examining the relevance and scope of the simplifying assumptions, we test the limits of our analytical approach through a scaling analysis.

6.1.1 Navier–Stokes

The Navier–Stokes equation, in its most general form, can be said to describe how fluid moves. In this section, we follow the treatment provided by a comprehensive microfluidics review paper[72]. Within the microfluidics community, it is commonly assumed that the working fluid is water, or some aqueous solution. As such, microfluidics most commonly deals with the incompressible form of the Navier–Stokes equation. Further assuming that the fluid in question is Newtonian and there are no body forces in the system, we arrive at Eq. 6.1:

$$\rho\frac{\partial u}{\partial t} = -\rho u\nabla u - \nabla p + \eta\nabla^2 u \tag{6.1}$$

In the preceding equation, ρ is the fluid density, u is the fluid velocity field, t is time, p is the pressure, and η is the fluid viscosity. Examining Eq. 6.1, we see that a fluid's change in momentum can arise from either convective, pressure, or viscous forces.

From this equation, it is common within microfluidics to make another set of simplifying assumptions. Specifically, we consider fully developed, steady-state flow along one direction of an infinitely long, straight, cylindrical channel. In this condition, the flow is laminar and free of any acceleration. As such, the convective term in Eq. 6.1 goes to zero, as does the time-dependent term. We thus arrive at Eq. 6.2:

$$\nabla p = \eta \nabla^2 u \tag{6.2}$$

If the consequences of geometric considerations are propagated through (e.g., that the flow field is axisymmetric), and we perform the necessary integration, we arrive at a simplified case described by the Hagen–Poiseuille equation.

6.1.2 Hagen–Poiseuille

The Hagen–Poiseuille equation describes the volumetric flow rate for steady-state pressure-driven flow in an infinitely long, perfectly straight, cylindrical channel. The Hagen–Poiseuille equation is shown in Eq. 6.3:

$$Q = \frac{\pi r^4}{8\eta} \frac{\Delta p}{L} \tag{6.3}$$

In this equation, Q is the volumetric flow rate, r is the radius of the channel, and L is the channel length.

To gain a better intuitive understanding of the relationship between pressure and flow rate, we may simplify Eq. 6.3 by grouping terms and writing:

$$Q = \frac{\Delta p}{R_H} \tag{6.4}$$

where:

$$R_H = \frac{8\eta L}{\pi r^4} \tag{6.5}$$

We call the variable R_H the hydraulic resistance. As we shall shortly see, writing the Hagen–Poiseuille equation in the form of Eq. 6.4 and considering the hydraulic resistance (Eq. 6.5) separately will lend profound insight into the nature of microfluidics.

6.1.3 Violating assumptions of the model

Up until this point, we have made a number of assumptions. Specifically, we assume an incompressible, Newtonian fluid; no body forces; fully developed, steady-state, laminar flow that is free of any acceleration; and an infinitely long, perfectly straight, cylindrical channel.

The violation of some of these assumptions may have rather simple remedies. For instance, the correction required from considering different channel cross-sections is quite straightforward. For non-cylindrical channels, we can replace

the channel radius r with r_H, which is known as the hydraulic radius. In general, we define:

$$r_H = \frac{2A}{P} \tag{6.6}$$

where A is the cross-sectional area of the channel, and P is the perimeter. Note that for a cylindrical channel, $A = \pi r^2$ and $P = 2\pi r$, which allows us to recover $r_H = r$. For a rectangular channel with width w and height h, the hydraulic radius becomes:

$$r_H = \frac{w \times h}{w + h} \tag{6.7}$$

This common substitution yields estimates that are quite close to exact solutions[72].

As another example, we may consider the assumption of a channel of infinite length. In traditional microfluidics, researchers are of course interested in channels of finite length that are not perfectly straight, and have found that violating the assumption of an infinite, perfectly straight channel is not terribly egregious. Correcting other assumptions is not as simple, as we shall see.

6.1.4 Hydraulics vs. pneumatics

In a system of digital logic, an ideal medium would carry information at infinite speeds and experience no losses of any kind as it moves. In any real system of logic, whether utilizing electrons or fluid elements, a signal will travel at finite

speeds and will experience losses (e.g., due to some resistance). Within fluidics, the properties of our working fluid (e.g., density, viscosity) will influence computation times, switching frequency, and other relevant system parameters.

Most researchers in microfluidics use water (or some aqueous solution) as their working fluid (we call such systems "hydraulic"). For soft robotic applications, it is often much more convenient and practical to use air (these systems we call "pneumatic"). This change in working fluid introduces a number of complications. First, water is incompressible, while air is compressible. In deriving the Hagen–Poiseuille equation, we began with the incompressible form of the Navier–Stokes equation. Violating this assumption by switching from hydraulics to pneumatics will have certain repercussions on the final system.

We additionally assumed laminar flow. Laminar flow may be defined as flow that exhibits a Reynolds number (Re) under 2300 (assuming the conditions of the Hagen–Poiseuille equation; a more general requirement is that Re is less than unity). This relationship is typically expressed as:

$$Re < 2300 \tag{6.8}$$

where:

$$Re = \frac{\rho\, U D}{\eta} \tag{6.9}$$

Here, U is some characteristic velocity (in our case, we may use the volumetric flow rate through the channel divided by the channel cross-sectional area) and

D is some characteristic length (in our case, this may be the hydraulic radius, r_H).

Given that the density of air is three orders of magnitude less than that of water, and that its viscosity is two orders of magnitude less, Eq. 6.9 would suggest that, for a given system, changing from water to air would yield a Reynolds number a full order of magnitude lower. However, this assumes that U and D are constant. While the characteristic length of the system is invariant under changes in working fluid, the characteristic velocity certainly is not. Remembering Eq. 6.3, we see that flow rate scales inversely with viscosity:

$$Q \sim \eta^{-1} \tag{6.10}$$

We may take flow rate as a surrogate for the characteristic velocity, as they scale identically for a given channel geometry. (A given channel geometry implies a given cross-sectional area, and we said above that the characteristic velocity can be considered to be the flow rate divided by the cross-sectional area.) Considering Eqs. 6.9 and 6.10, we may write:

$$Re \sim \rho\eta^{-2} \tag{6.11}$$

Again using the actual relative densities and viscosities of water and air, we see that switching from water to air actually increases the Reynolds number by an order of magnitude, in part because it increases the flow rate by two orders of magnitude (all else being held equal). This increase in Reynolds number from

changing the working fluid can be enough to cause the flow to leave the laminar regime. Even more consequential than using air rather than water is the effect of channel size, to which we turn next.

6.1.5 Scaling

In Eq. 6.10, we have considered how flow rate scales with the working fluid viscosity. However, Eq. 6.3 suggests that flow rate scales much, much more strongly with the effective channel radius:

$$Q \sim r^4 \quad or \quad Q \sim r_H^4 \tag{6.12}$$

To gain somewhat of an intuitive understanding of relative magnitudes, we calculated flow rates for different microchannels, of sizes ranging from those relevant to microfluidics (10 μm height and 100 μm width) to those that may be relevant for soft robotics (250 μm height and 1000 μm width). We assumed air as the working fluid, with a moderate applied pressure of 138 kPa and a standard channel length of 20 mm. The result of these calculations can be seen in Fig. 6.1.

As a check on these calculations, we compared the predicted flow rate to an actual system presented in the literature that was fabricated and tested. In that work[18], a microchannel with dimensions of 100 μm by 15 μm and an applied pressure of 138 kPa yielded a flow rate of 4.4 μL/s; our model predicts 4.2 μL/s at the same operating condition.

Having provided some confirmation to our model, we then sought to inves-

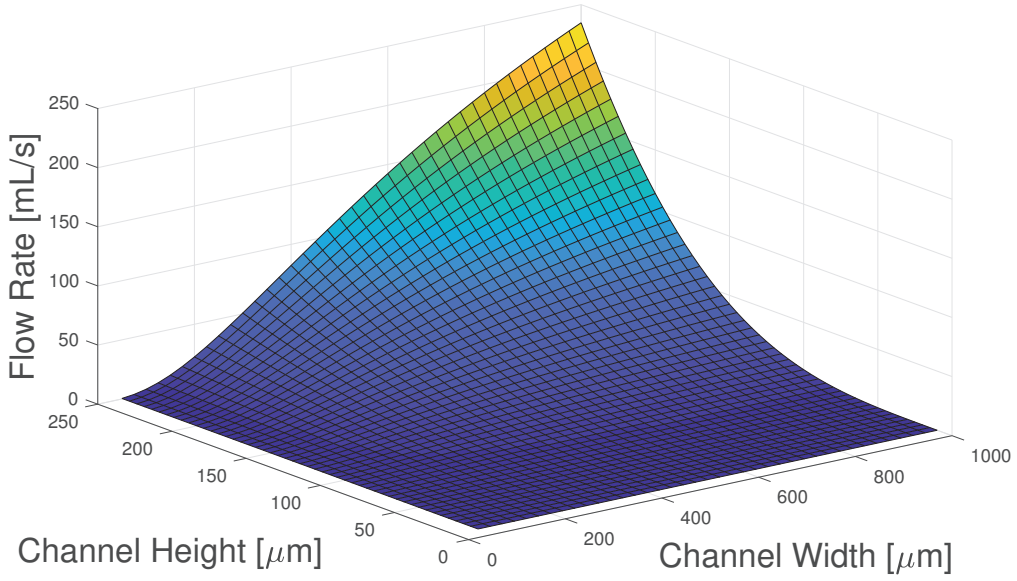

Figure 6.1: Output of flow rate modeling for pneumatic flow within a microchannel as a function of channel height and width. This model relies on the assumptions of the Hagen–Poiseuille equation. The calculations use an input pressure of 138 kPa and a channel length of 20 mm.

tigate three questions: What size scales are we theoretically able to influence? What size scales are we practically able to influence? What size scales do we want to influence? These questions were used to guide thinking when designing circuits, and are considered in detail in the following sections.

6.1.6 Circuit design workflow

So far this chapter has considered the governing equations and assumptions related to fluid flow in microchannels. We now turn to the question of how to design a microfluidic circuit for a specific soft robotic application. Of course, a microfluidic circuit is composed of microchannels, so the preceding discussion is of utmost relevance.

In designing a microfluidic circuit to control a soft actuator, we first must know the operating conditions of the soft actuator. At a fundamental level, we are most concerned with the pressure and flow rate at which the actuator will operate. Actuation pressures of soft actuators are commonly reported in the literature and are a standard metric of performance; flow rates are less commonly reported. However, a good estimate of an actuator's flow rate may be obtained from either reported values or estimates of both the actuator's internal volume and actuation frequency. In general, we see an inverse relationship between these two quantities; larger actuators are typically actuated at a lower frequency, while smaller actuators are actuated much more rapidly. As such, the range of flow rates relevant to soft robotics may be relatively small. From a course survey of the literature, we have found typical flow rates to range from 1

– 100 mL/s.

Once we have the soft actuator quantified in terms of pressure and flow rate, we can determine the hydraulic resistance using Eq. 6.4. Given the scaling presented in Eqs. 6.10 and 6.12, we know that the hydraulic resistance will be dominated by the microchannel dimensions. As such, we may use a plot similar to the one presented in Fig. 6.1 to determine appropriate channel heights and widths for a given pressure and flow rate. (The ratio of channel height to channel width is discussed in the earlier chapter on microchannel fabrication.) With our channel dimensions chosen, we can then go about designing the details of the microfluidic circuit.

6.2 The electrical analogy

We may consider a microfluidic circuit to be composed of individual components, and the connections between those components. The connections between components are nothing but the microchannels themselves. We have examined the question of microchannel shape and fabrication strategy in an earlier chapter, and have devoted the beginning of this chapter to understanding fluid flow within microchannels and how to size microchannels for the pressure and flow rate requirements of a given soft actuator.

With a strong understanding of the connections within a microfluidic circuit, the next questions are obvious: What are the individual components? How do we design them? And what are their driving parameters? To answer these ques-

tions, we turn to the world of electrical circuits.

6.2.1 Overview

An electrical circuit is, in its most basic sense, a system that enables and regulates the flow of electrons. Such a system depends on some voltage (or current) source, and some sink, typically called electrical ground. Between the source and ground, there may be numerous circuit elements, including resistors, capacitors, inductors, diodes, and transistors, in addition to many others.

When first learning about electrical circuits, students are often instructed to think of these systems as analogous to fluid systems, in hopes of providing a more intuitive understanding of their behavior. Whereas an electrical circuit is concerned with electrical flow (i.e., the flow of electrons), the fluid system is of course concerned with fluid flow. The somewhat abstract idea of an electrical circuit's charge flux (or current) can be understood in the much more familiar notion of a fluid system's volumetric flux (or flow rate). The driving potential of an electrical circuit (a voltage difference) can be understood by thinking of the driving force behind a fluid system (a pressure difference). An electrical resistor is an element that restricts the flow of electrons, in the same way that the narrowing of a pipe restricts the flow of fluid. With these simple comparisons, students gain an intuitive sense of how to think about electrical circuits.

For our purposes, it will be useful to turn this analogy around. Rather than using the analogy to gain a basic intuition about how electrical circuits work, we will use the analogy to gain significant insight into how to design fluidic cir-

cuits. The success of electronics is hard to overstate, and the ability of electrical circuits to enable complex behavior is a phenomenon with which everyone is familiar. Given this success, it is prudent for designers of fluidic circuits to leverage the lessons learned from electronics, rather than building a new system in isolation.

Using this analogy, we should be able to build sophisticated fluidic circuits approaching the level of complexity seen in electrical circuits. In theory, there is no reason why we should not be able to build computers that operate using fluid rather than electricity. However, there are certain practical considerations that impose limitations on the achievable level of complexity. One of the most obvious differences between electrical and fluidic circuits is their size. Electrical components have become extremely small, and the density with which electrical components can be packed is unparalleled. Because fluidic components are larger than their electrical analogs, so too are fluidic circuits. As such, the level of complexity that electrical circuits can achieve for a given spatial area greatly exceeds that available to fluidic circuits. In addition, the flow of electricity is orders of magnitude faster than the flow of fluid (whether water or air). As such, electrical circuits routinely operate at GHz frequencies, whereas fluidic circuits rarely operate beyond tens of Hz. Finally, there is the notion of resistivity. Electrical connectors (e.g., wires) typically have very low resistance, whereas fluidic connectors (e.g., microchannels) have comparatively high resistances. Consequently, the length of a microchannel becomes a limiting factor in a microfluidic circuit much sooner than the length of a wire starts to limit

an electrical circuit. These restrictions on minimum size, maximum speed, and connector length suggest that electrical circuits will always out-perform fluidic circuits. However, as discussed previously, there are many reasons why we may want to create fluidic circuits; the analogy to electronics allows us to do so in an intelligent manner.

6.2.2 Key relationships

The details of this analogy are explained in a paper by Oh et al[72]. In addition to the aforementioned relationships between voltage and pressure, and current and flow rate, there are other central analogs. For instance, a wire in electronics is simply a medium through which charge can flow. As such, the fluidic "wire" is any open space through which fluid can flow; for our purposes, this space is often the interior of a microchannel. A list of the key relationships upon which this analogy relies is presented in Table 6.1.

One detail that may be overlooked is the fact that, just as electrical circuits must be grounded for the theory to apply, fluidic circuits too must be grounded. The fluidic equivalent of electrical ground is simply atmospheric pressure. As such, any fluidic circuit must be open to the atmosphere at some point. Of course, almost any fluidic circuit of use will be grounded through a fluidic resistor; otherwise, the result would be a fluidic "short" (akin to a "short" in electronics) that effectively equates to a leak in the system.

Electronics	Microfluidics
Voltage (V)	Pressure (P)
Current (I)	Volumetric flow rate (Q)
Electrical Resistance (R_E)	Hydraulic Resistance (R_H)
Wire	Microchannel
Battery	Pump
Electrical ground	Atmospheric pressure
Ohm's Law $V = IR_E$	Hagen–Poiseuille's Law $\Delta P = QR_H$
Kirchoff's current law $\sum I_n = 0$ (at a node)	Law of mass conservation $\sum Q_n = 0$ (at a node)
Kirchoff's voltage law $\sum V_n = 0$ (in a closed path)	Law of energy conservation $\sum \Delta P_n = 0$ (in a closed path)

Table 6.1: A summary of key relationships in the electrical analogy for microfluidics.

6.3 Validating assumptions of the analogy

In the first section, we examined the governing equations for microfluidic systems, and asked when the assumptions of those equations were violated. We also compared published pressure and flow rate data from the literature to predictions from our model based on those governing equations, and found excellent agreement. In the next section, we considered an analogy between microfluidics and electronics, with the goal of gaining insight into microfluidic circuit design. In this section, we exploit that analogy to build simple microfluidic circuits with predictable behavior and characterize the deviation of these circuits from their ideal, theoretical performance. These tests elucidated additional assumptions not present in the governing equations but rather derived from the

introduction of the electrical analogy, and let us understand the scope of those assumptions.

6.3.1 Voltage divider principle

A voltage divider is a simple electrical circuit that produces an output voltage that is a fraction of the input voltage using just two resistors. A schematic of a voltage divider can be seen in the left half of Fig. 6.2. If the relative values of the two resistors in the circuit are known, the output voltage is given as a simple fraction of the input voltage. The standard proof relies on rearranging Ohm's law to express current as the ratio of the voltage drop to the effective resistance. If we assume that the current through the output is negligible, we can conclude that the current from the input to ground is identical to the current from the output to ground. That is:

$$I = \frac{V_{in}}{R_1 + R_2} = \frac{V_{out}}{R_2} \tag{6.13}$$

Solving for V_{out}, we find:

$$V_{out} = \frac{R_2}{R_1 + R_2} V_{in} \tag{6.14}$$

6.3.2 Pressure divider

Based on the discussion from the last section, we know the voltage divider should have a direct analogy in the microfluidics realm. Given that pressure is

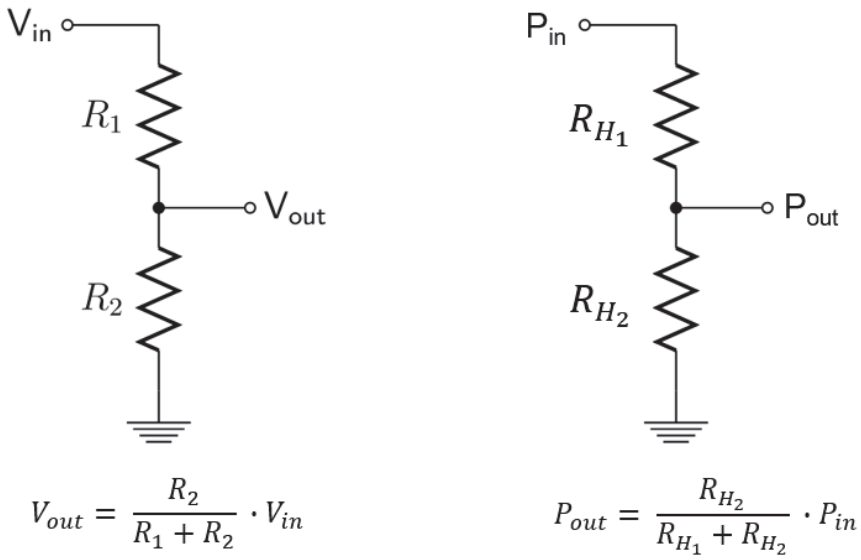

Figure 6.2: Schematics and transfer functions for an electrical voltage divider (left) and a fluidic pressure divider (right).

the analog of voltage, we will call such a fluidic circuit a pressure divider.

Referring back to Table 6.1, we know that pressure is analogous to voltage, and hydraulic resistance is analogous to electrical resistance. We make these substitutions in the right half of Fig. 6.2. We may arrive at an expression for the output pressure either by rederiving it using Hagen–Poiseuille's law (the analog of Ohm's law), or simply by making the appropriate substitutions to the final expression for the voltage divider.

6.3.3 Fluidic resistor design and experimental testing

It is important to note that the absolute value of the resistors (in either the electrical or the fluidic circuit) need not be known. Instead, the salient detail

is the relative values of the two resistors in the circuit. Referring back again to Eq. 6.5, we know that the hydraulic resistance (R_H) depends on the fluid viscosity (η), the length of the channel (L), and the effective radius of the channel (r). Given that there is only one fluid in the system, we cannot change the fluid viscosity to achieve different resistances. In choosing between changing the channel length and its effective radius, we opt to change the length. If we were to rely on changing the effective radius of the channel, fabrication errors that resulted in channel dimension discrepancies would be greatly magnified (refer back to the scaling presented in Eq. 6.12), resulting in unpredictable circuit behavior. Conversely, the linear scaling of the hydraulic resistance with channel length is much more forgiving of manufacturing defects.

To test the agreement between the predictions made by leveraging the electrical analogy and the behavior of actual fluidic circuits, we fabricated pressure dividers with different relative resistances. By using either two identical resistors or a pair of resistors in which one was twice the length (and thus twice the resistance) of the other, we made three pressure dividers with expected output pressures of 2/3, 1/2, and 1/3 of the input pressure. Schematics of these circuits can be seen in Fig. 6.3.

In our setup, we used an input pressure of 138 kPa, as measured by a digital pressure sensor connected immediately downstream of the point in the circuit at which the pressure source was connected. We used additional digital pressure sensors both at the point in the circuit between the resistors (i.e., the output) and after the second resistor. Downstream of the second resistor, we punched a

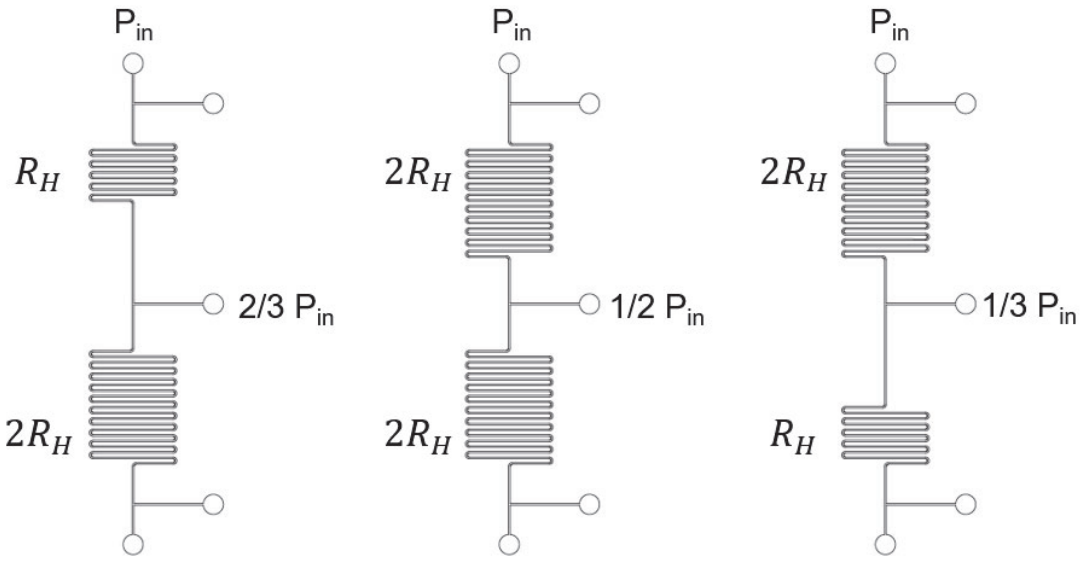

Figure 6.3: Schematics of the three pressure dividers used to test the assumptions of the electrical analogy. We opted to change resistance by changing resistor length rather than microchannel radius due to the more forgiving scaling with respect to fabrication errors.

hole to connect the circuit to atmospheric pressure, grounding it. The data from the three digital pressure sensors were recorded by an Arduino microcontroller that passed the pressure values to a computer running a MATLAB script that plotted the pressures in real time. This setup can be seen in Fig. 6.4.

For the three pressure dividers with expected outputs of 2/3, 1/2, and 1/3 of the input pressure, we found actual output pressures of 80%, 65%, and 55% of the input pressure, respectively. We expected that the discrepancy was largely due to the relatively high input pressure deforming the elastomeric walls of the microchannels. When we reduced the input pressure to 41 kPa, we found actual output pressures of 71%, 54%, and 42% of the input pressure. The fact that these values are much closer to the values predicted by theory lends support to

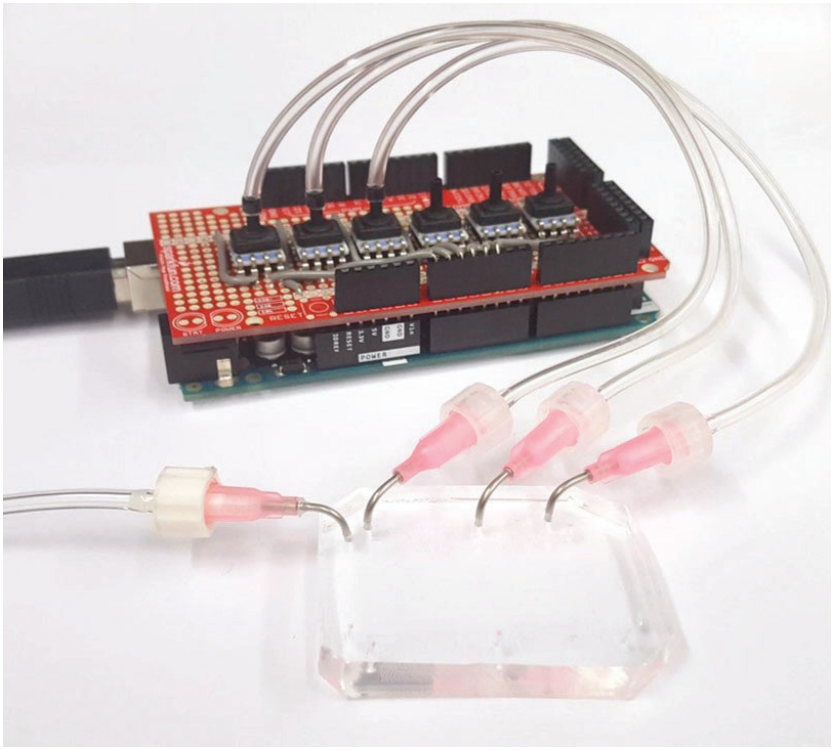

Figure 6.4: To record data from our pressure dividers, we used three digital pressure sensors whose output was recorded by an Arduino microcontroller.

	Circuit 1	Circuit 2	Circuit 3
Theory	67%	50%	33%
Input = 138 kPa	80%	65%	55%
Input = 41 kPa	71%	54%	42%

Table 6.2: A comparison between the theoretical outputs (expressed as a percentage of input pressure) from the pressure dividers alongside their actual outputs, for two different input pressures. The better agreement between theory and experiment at the lower input pressure implies that high pressures introduce complications not accounted for by the theory.

our hypothesis that high pressures contribute to behavior that deviates from ideal performance. These results are summarized in Table 6.2.

6.3.4 Analog vs. digital

In the previous section, we see better agreement between theory and experiment at lower input pressures. This result motivates the adoption of another convention from electronics: the distinction between analog and digital circuits. Just as electronic circuits perform logical operations at low voltages, and then amplify the output voltage to drive some kind of actuator, fluidic circuits too could perform logic at low pressures, only to amplify the result when that pressure is required to do mechanical work. This division of labor between analog and digital fluidic circuits would allow us do computation work at low pressures, where we can design and model complex circuits with confidence, and then magnify the result in a fluidic amplification stage. We now turn to the details of these digital fluidic circuits.

6.4 Logic gates and circuits

As suggested earlier, the importance of electrical circuits would be hard to overstate. The success of electronics is due in no small part to digital logic, which enables the complex behavior in systems driven by microcontrollers or computers.

In electronics, the fundamental building block of digital logic is the transistor. In fluidics, it is the microfluidic valve. We have already examined the microfluidic valve in detail, from a number of different perspectives, and have a strong understanding of its function as an individual circuit element. In this section, we explore how microfluidic valves may be combined to build the logic gates that enable a complete system of digital logic.

6.4.1 Principles of Boolean algebra

Boolean algebra is the mathematics used in digital logic systems. Any variable in this framework can only take on one of two values: true (1) or false (0). In electronics, these discrete values are mapped onto the continuous space of possible voltages through thresholding. For instance, a logical "high" signal (1) may be defined at 5V, whereas a logical "low" signal (0) may be defined at 0V. We can perform similar thresholding in fluidic systems, selecting pressures at which we define logical high and low signals.

Just as standard algebra has addition (+), subtraction (–), multiplication (×), and division (/), Boolean algebra too has basic operators. These basic op-

erators are negation ($\neg$), conjunction ($\wedge$), and disjunction ($\vee$). Negation operates on a single variable, and simply inverts its truth value. That is, $\neg$ A=0 if A=1, and $\neg$ A=1 if A=0. Negation is often denoted as NOT, as the output is true only if the input is not true. Conjunction operates on two variables, and gives a true output if and only if both inputs are true (i.e., $A \wedge B = 1$ iff A=1, B=1; else $A \wedge B = 0$). Conjunction is often denoted as AND, as the output is true only if both A and B are true. Disjunction also operates on two variables, and gives a false output if and only if both inputs are false (i.e., $A \vee B = 0$ iff A=0, B=0; else $A \vee B = 1$). Disjunction is often denoted as OR, as the output is true if A or B is true.

An important concept within Boolean algebra is "functional completeness". A functionally complete set of operators is one that can be used to construct any possible set of output truth values for a given set of variables. To solidify this idea, let us consider an example using our three basic operators. We shall show that the set of operators consisting of just negation and conjunction $\{\neg, \wedge\}$ is functionally complete. That is, we should be able to express our third basic operator, disjunction, as some combination of negation and conjunction. We begin by considering the negation of a disjunction:

$$\neg(A \vee B) \tag{6.15}$$

Based on our definitions above, we may consider this statement to say that "it is not the case" (negation) that "the output is false if and only if both A and B are false" (disjunction). That is, the output is true if and only if both A and

B are false. To say that A or B is false is simply a negation. Adding in the fact that "and" statements are conjuctions, we can write the expression in Eq. 6.15 as:

$$\neg(A \vee B) = \neg A \wedge \neg B \tag{6.16}$$

We may understand this equation as saying that if both A and B are false ($\neg$A $\wedge$ $\neg$B), it is not the case that A or B is true ($\neg$(A $\vee$ B)). This relationship is one of De Morgan's laws, and is often stated as "the negation of a disjunction is the conjunction of the negations". (The second of De Morgan's laws states that "the negation of a conjunction is the disjunction of the negations".)

By simply negating Eq. 6.16, we see that disjunction can be expressed in terms of negation and conjunction, suggesting functional completeness:

$$A \vee B = \neg(\neg A \wedge \neg B) \tag{6.17}$$

In addition to the set of negation and conjunction {$\neg$, $\wedge$}, there are other sets of Boolean operators that can be shown to be functionally complete. In fact, there are two functionally complete sets consisting of just one element. We just considered the negation of a disjunction, which is often denoted as NOR (for NOT OR), and have shown that it can be expressed as a combination of negation and conjunction, which compose a functionally complete set. As such, NOR by itself is functionally complete. If we instead consider the second of De Morgan's laws, we could conclude that the negation of a conjunction, which is

often denoted as NAND (for NOT AND), is similarly functionally complete. The implication is that any logical relationship between two variables can be constructed using only NOR or only NAND operators.

6.4.2 NOT, NOR, and NAND gates

With the basic theory of Boolean algebra discussed, we now turn to its implementation. To do so, we will begin to consider logic gates, which are simply physical elements that behave as Boolean operators. That is, a NOT gate is a circuit element that takes a signal (1 or 0) as input and produces the opposite signal (0 or 1) as output. Similarly, we can imagine OR, AND, NOR, and NAND logic gates. The salient question is now: how do we build these gates?

Let us return to our standard microfluidic valve, in which a high pressure on the control channel deflects a membrane and stops flow in the flow channel. If we consider our control channel as the input, and the flow channel as the output, we see that this is exactly a NOT gate. When the control channel is pressurized (1), there is no flow (0); when the control channel is depressurized (0), flow passes through the valve unrestricted (1). In Fig. 6.5, we show the symbol (for those familiar with electronics), truth table, and microfluidic implementation of the NOT gate.

We can construct a NOR gate by positioning two microfluidic valves in series. Flow only passes through to the output if both valves are inactive (i.e., there is output flow if it is NOT the case that either the first OR the second input is pressurized). Similarly, we can construct a NAND gate by splitting the

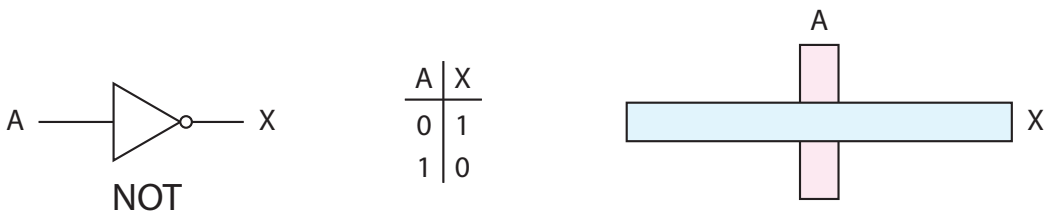

Figure 6.5: Symbol, truth table, and microfluidic implementation (from left to right) of NOT logic gate. This logic gate is simply a microfluidic valve, where the input is the control channel and the output is the flow channel.

flow channel and positioning two valves in parallel. Flow is only impeded if both valves are active (i.e., there is output flow if it is NOT the case that both the first AND the second inputs are pressurized). In Fig. 6.6, we show the symbol, truth table, and microfluidic implementation of the NOR and NAND gates.

Based on our previous discussion of functional completeness, we know that either the NOR gate or the NAND gate is sufficient to build any logical relationship between inputs that we desire. As has been shown in electronics, we can then build circuit elements such as comparators, latches, counters, and many more. As the microfluidic valve is the only component necessary to build either the NOR gate or the NAND gate, it would be accurate to say that this element alone is sufficient to build extremely complex fluidic circuits. This progression is detailed in Fig. 6.7.

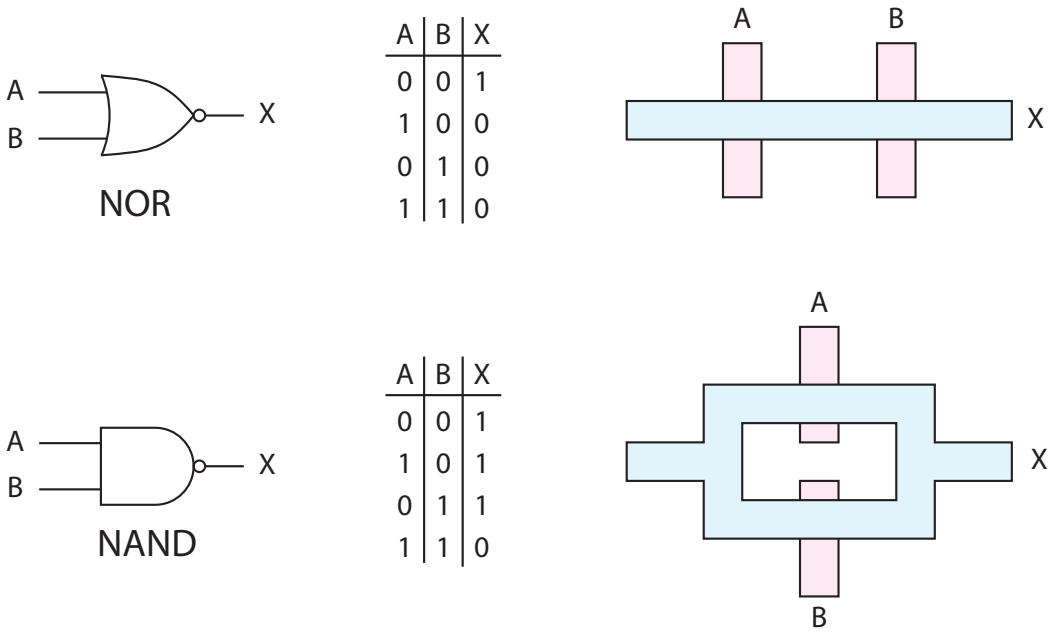

Figure 6.6: Symbols, truth tables, and microfluidic implementations (from left to right) of NOR and NAND logic gates (from top to bottom). The NOR gate is built from two NOT gates in series, while the NAND gate is built from two NOT gates in parallel.

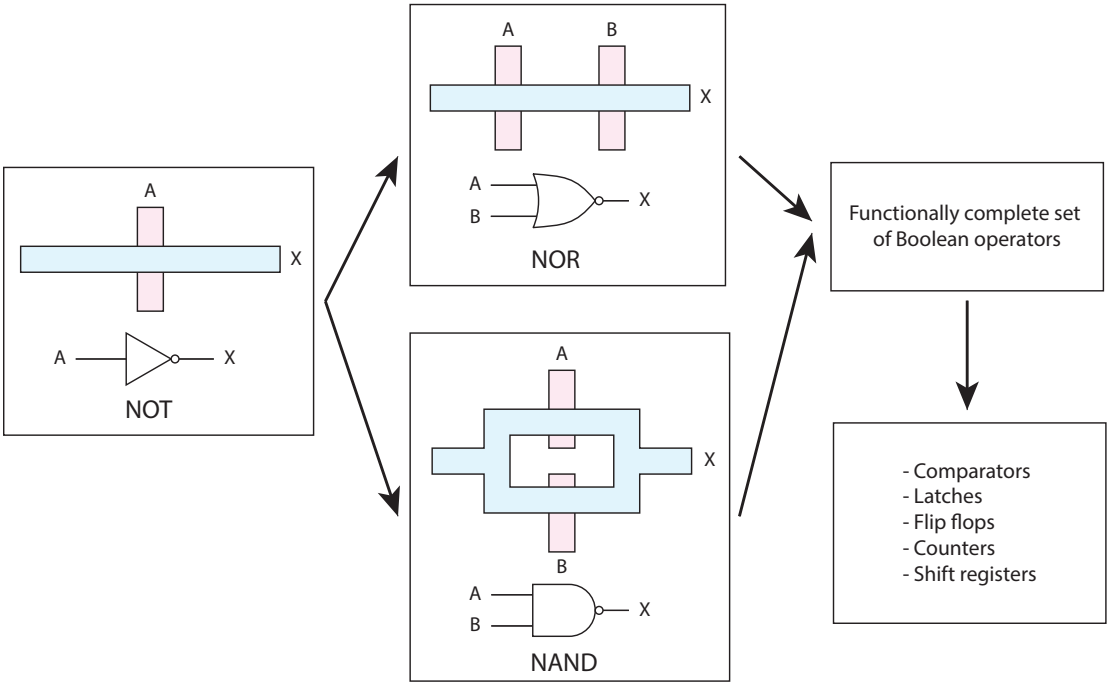

Figure 6.7: With just a microfluidic valve (which can be understood as a NOT gate), one can build NOR or NAND gates, either of which is a functionally complete set of Boolean operators. As such, one can then build advanced circuit elements that can enable complex behavior.

6.4.3 High gain valves and logic circuits

One detail that requires our attention is that of cascading circuit elements. We have seen that more complex behavior may be achieved by combining Boolean operators (e.g., how disjunction can be defined in terms of negation and conjunction); a similar increase in complexity may be achieved by combining logic gates. In the case of microfluidic logic, cascading gates requires that the output of one gate (the flow channel) serve as the input to the next gate (the control channel).

In our previous implementations of the microfluidic valve, we have relied on a higher pressure in the control channel relative to the flow channel to ensure valve closure. In a system of fluidic logic, this pressure difference can no longer be exploited, as flow channels themselves transition into control channels. As such, we need a valve that can stop flow (in the flow channel) at a certain pressure with an equal (or, ideally, lesser) pressure in the control channel. We call these valves "high gain valves".

There are a number of examples of high gain valves in microfluidics, which have been used to develop digital logic systems of varying complexity[125,18]. Others have obviated the need for high gain valves in their digital logic systems by introducing valves that are actuated with vacuum rather than positive pressure[28,89]. Although all of these systems operate at pressures and flow rates that are often significantly below values that are of interest to researchers in soft robotics, the high gain valves used in some of these systems can inspire the de-

sign of scaled valves that are appropriate for soft robotics.

6.5 Conclusions

In this chapter, we have discussed the possibility of building a system of fluidic logic for soft robots. We began with the equations that govern flow within a microchannel, and examined the assumptions of those equations. Most importantly, we performed a scaling analysis to determine how sensitive our model is to different variables. We then discussed a workflow for designing microfluidic circuits given the pressure and flow rate requirements of a soft actuator.

Next we introduced an analogy between electronics and fluidics, and suggested that this analogy could lend profound insight into the design of fluidic circuits. We characterized the limitations of this analogy by building pressure dividers (the fluidic equivalent of electrical voltage dividers) and measured the degree of deviation from theory.

With the electrical analogy established, we turned to logic gates. After reviewing the basics of Boolean algebra, we suggested ways in which Boolean operators could be realized in microfluidic logic gates. We discussed limitations of directly implementing our previously discussed microfluidic valve in these logic gates, and suggested design references for how to adapt our microfluidic valve to make it appropriate to serve as the building block of a complete system of microfluidic logic.

7

Conclusions and Future Work

In this dissertation, we have examined the question of how to control motion in soft robotic systems. The discussion has centered largely on practical questions concerning the design and fabrication of control systems, striving for generalizable design rules whenever possible. We have investigated both passive control, in which the robot's morphology performs some degree of control in a

fully integrated and organic fashion, and active control, wherein fluidic digital logic signals are manipulated to produce a desired behavior.

In systems with passive control, we discussed the idea of morphological computation, which suggests that the natural response of a body to some stimulus may be conceived of as a sort of control system in its own right. While it may be said that any soft robot performs some degree of morphological computation, we have endeavored to approach passive control in an intentional and systematic fashion. Given that a robot's body is the result of a manufacturing process, we have considered the question of morphological computation in light of the capabilities of novel fabrication paradigms that we have proposed and evaluated. Specifically, we first examined how multimaterial 3D printing enables the manufacture of stiffness gradients in soft robot bodies, which both solves integration concerns that have routinely plagued the field and simultaneously introduces soft robots with previously unseen speeds and robustness. Then we turned to a fabrication routine that combines a number of established techniques in a new fashion, creating small-scale robotic systems of unparalleled complexity.

For active control, we began with an exhaustive study of fabrication methodologies to create rounded microchannels, which are essential to the function of microfluidic valves, upon which we would base our entire control system. With an understanding of the relevant design and fabrication concerns for microchannels, we explored microfluidic valves, and evaluated their performance in a multiplexing scheme that hints at one practical implementation of active

fluidic control in soft robotic systems. From there, we laid out a procedure for designing fluidic circuits that behave analogously to electronic circuits, taking time to understand the governing equations, as well as their assumptions and limitations. We introduced a framework in which microfluidic valves may be combined to create logic gates, enabling a full system of fluidic logic.

There are a number of future directions for this line of research that will enable intricate control of soft robots. As suggested at the conclusion of the chapter on fluidic logic components and circuits, the microfluidic valve that we have been using must be adapted to be able to actuate without relying on a positive pressure differential between the control and flow channels. In that chapter, we suggested a number of microfluidic valves that exhibit this behavior, and lay out a framework that may be utilized to scale such valves to enable the pressures and flow rates relevant to soft robotics. With such valves, one can cascade logic gates and create mature logic circuits capable of complex control.

In the chapter on microfluidic multiplexing, we demonstrated a scheme in which one could drastically reduce the number of separate fluidic lines upon which a soft robot may need to rely while still retaining the ability to produce complex behavior. Reducing the number of lines in a tether even further would require the ability to drive a full logic circuit from only a single constant pressure source. For instance, a cyclical gait could be generated from a constant pressure source with an oscillator circuit composed of fluidic resistors and capacitors. To eliminate the tether entirely, the power source must be brought on board. While some work has looked at chemical power generation, these sys-

tems rarely act as constant pressure sources, necessitating future research into on-board power generatation.

To be able to be accurately called autonomous, soft robots must be able to respond to their environments. While we have argued that morphological computation enables this ability to some degree, we acknowledge that this level of interaction is limited. Specifically, morphological computation allows soft robots to immediately react to their environment, but not to plan future behaviors. To enable any level of complex behavior, active control systems capable of receiving input must be relied upon. If we exclude the type of input seen in the chapter on multiplexing, in which a user manipulates input signals through a tether, the goal of an interactive soft robot necessitates soft sensors that generate digital logic signals that are intelligible to a fluidic control system. The space for creative soft sensor design and implementation is nearly boundless; exploring this space should lead to a new class of soft robots unlike any the field has seen thus far.

Perhaps most exciting is the integration of these two control philosophies. In this dissertation, we have considered the questions of passive and active control separately. However, should active fluidic control be developed sufficiently in the manner described above, it could be incorporated into a system designed to perform morphological computation, leading to a soft robot cable of both active and passive control in a coordinated fashion. In such a system, both control methodologies might continuously interact with one another and behave as a single entity. To incorporate fluidic logic into morphologically complex robots,

one could imagine directly printing fluidic circuits into a robot body in a highly integrated fashion, leveraging the techniques and insights suggested in the chapter on multimaterial 3D printing, or fabricating fluidic circuits in a more traditional lithographic manner and manipulating layer profile geometry, as demonstrated in the chapter on precision micromachining for multilayer soft lithography.

The field of soft robotics has seen rapid development and has rightfully generated much excitement. However, it is still very much a field in its infancy. In this dissertation, we have taken advantage of an analogy to electronics to elucidate certain ideas. We have compared the microfluidic valves in this work to transistors in electronics; in reality, they are much more akin to vacuum tubes. In terms of computational complexity, we are still pre-ENIAC. While these statements may be understood as referring to active fluidic control systems, similar sentiments may be expressed about soft robotics generally. The hope is that the work presented in this dissertation may lay a foundation upon which later soft robotic control research can build, and that the future directions outlined here may inspire others to build control systems that enable autonomous soft robots.

References

[1] Abdelgawad, M., Wu, C., Chien, W.-Y., Geddie, W. R., Jewett, M. A., & Sun, Y. (2011). A fast and simple method to fabricate circular microchannels in polydimethylsiloxane (pdms). *Lab on a Chip*, 11(3), 545–551.

[2] Abgrall, P., Conedera, V., Camon, H., Gue, A.-M., & Nguyen, N.-T. (2007). Su-8 as a structural material for labs-on-chips and microelectromechanical systems. *Electrophoresis*, 28(24), 4539–4551.

[3] Asthana, A., Kim, K.-O., Perumal, J., Kim, D.-M., & Kim, D.-P. (2009). Facile single step fabrication of microchannels with varying size. *Lab on a Chip*, 9(8), 1138–1142.

[4] Bao, G., Fang, H., Chen, L., Wan, Y., Xu, F., Yang, Q., & Zhang, L. (2018). Soft robotics: Academic insights and perspectives through bibliometric analysis. *Soft Robotics*, 5(3), 229–241.

[5] Bartlett, N. W., Tolley, M. T., Overvelde, J. T., Weaver, J. C., Mosadegh, B., Bertoldi, K., Whitesides, G. M., & Wood, R. J. (2015). A 3d-printed, functionally graded soft robot powered by combustion. *Science*, 349(6244), 161–165.

[6] Bartlett, N. W. & Wood, R. J. (2016). Comparative analysis of fabrication methods for achieving rounded microchannels in pdms. *Journal of Micromechanics and Microengineering*, 26(11), 115013.

[7] Bellouard, Y., Said, A., Dugan, M., & Bado, P. (2004). Fabrication of high-aspect ratio, micro-fluidic channels and tunnels using femtosecond laser pulses and chemical etching. *Optics express*, 12(10), 2120–2129.

[8] Bhargava, K. C., Thompson, B., & Malmstadt, N. (2014). Discrete elements for 3D microfluidics. *Proceedings of the National Academy of Sciences of the United States of America*, 111(42), 15013–8.

[9] Borenstein, J. T., Tupper, M. M., Mack, P. J., Weinberg, E. J., Khalil, A. S., Hsiao, J., & García-Cardeña, G. (2010). Functional endothelialized microvascular networks with circular cross-sections in a tissue culture substrate. *Biomedical microdevices*, 12(1), 71–79.

[10] Breger, J. C., Yoon, C., Xiao, R., Kwag, H. R., Wang, M. O., Fisher, J. P., Nguyen, T. D., & Gracias, D. H. (2015). Self-folding thermomagnetically responsive soft microgrippers. *ACS Applied Materials and Interfaces interfaces*, 7(5), 3398–405.

[11] Cao, J., Qin, L., Lee, H. P., & Zhu, J. (2017). Development of a soft untethered robot using artificial muscle actuators. In *Electroactive Polymer Actuators and Devices (EAPAD) 2017*, volume 10163 (pp. 101631X).: International Society for Optics and Photonics.

[12] Chen, C., Hirdes, D., & Folch, A. (2003). Gray-scale photolithography using microfluidic photomasks. *Proceedings of the National Academy of Sciences*, 100(4), 1499–1504.

[13] Cho, K.-J., Koh, J.-S., Kim, S., Chu, W.-S., Hong, Y., & Ahn, S.-H. (2009). Review of manufacturing processes for soft biomimetic robots. *International Journal of Precision Engineering and Manufacturing*, 10(3), 171.

[14] Chou, H.-P., Unger, M. A., & Quake, S. R. (2001). A microfabricated rotary pump. *Biomedical Microdevices*, 3(4), 323–330.

[15] Christianson, C., Goldberg, N. N., Deheyn, D. D., Cai, S., & Tolley, M. T. (2018). Translucent soft robots driven by frameless fluid electrode dielectric elastomer actuators. *Science Robotics*, 3(17), eaat1893.

[16] Conradie, E. H. & Moore, D. F. (2002). Su-8 thick photoresist processing as a functional material for mems applications. *Journal of Micromechanics and Microengineering*, 12(4), 368.

[17] Czaplewski, D. A., Kameoka, J., Mathers, R., Coates, G. W., & Craighead, H. (2003). Nanofluidic channels with elliptical cross sections formed using a nonlithographic process. *Applied Physics Letters*, 83(23), 4836–4838.

[18] Devaraju, N. S. G. K. & Unger, M. A. (2012). Pressure driven digital logic in pdms based microfluidic devices fabricated by multilayer soft lithography. *Lab on a Chip*, 12(22), 4809–4815.

[19] Dy, A. J., Cosmanescu, A., Sluka, J., Glazier, J. A., Stupack, D., & Amarie, D. (2014). Fabricating microfluidic valve master molds in su-8 photoresist. *Journal of Micromechanics and Microengineering*, 24(5), 057001.

[20] Emerson, D. R., Cieślicki, K., Gu, X., & Barber, R. W. (2006). Biomimetic design of microfluidic manifolds based on a generalised murray's law. *Lab on a Chip*, 6(3), 447–454.

[21] Fordyce, P., Diaz-Botia, C., DeRisi, J., & Gomez-Sjoberg, R. (2012a). Systematic characterization of feature dimensions and closing pressures for microfluidic valves produced via photoresist reflow. *Lab on a Chip*, 12(21), 4287–4295.

[22] Fordyce, P., Diaz-Botia, C., DeRisi, J., & Gomez-Sjoberg, R. (2012b). Systematic characterization of feature dimensions and closing pressures for microfluidic valves produced via photoresist reflow. *Lab on a Chip*, 12(21), 4287–4295.

[23] Fu, A. Y., Chou, H.-P., Spence, C., Arnold, F. H., & Quake, S. R. (2002). An integrated microfabricated cell sorter. *Analytical Chemistry*, 74(11), 2451–2457.

[24] Futai, N., Gu, W., & Takayama, S. (2004). Rapid prototyping of microstructures with bell-shaped cross-sections and its application to deformation-based microfluidic valves. *Advanced Materials*, 16(15), 1320–1323.

[25] Gao, Y., Ota, H., Schaler, E. W., Chen, K., Zhao, A., Gao, W., Fahad, H. M., Leng, Y., Zheng, A., Xiong, F., et al. (2017). Wearable microfluidic diaphragm pressure sensor for health and tactile touch monitoring. *Advanced Materials*, 29(39).

[26] Gorissen, B., Reynaerts, D., Konishi, S., Yoshida, K., Kim, J.-W., & De Volder, M. (2017). Elastic Inflatable Actuators for Soft Robotic Applications. *Advanced Materials*, (pp. 1604977).

[27] Gottron, R., Kumar, V., & Corrado, A. (1975). Fluidic applications in north america. *IFAC Proceedings Volumes*, 8(1), 531–538.

[28] Grover, W. H., Ivester, R. H., Jensen, E. C., & Mathies, R. A. (2006). Development and multiplexed control of latching pneumatic valves using microfluidic logical structures. *Lab on a Chip*, 6(5), 623–631.

[29] Hines, L., Petersen, K., Lum, G. Z., & Sitti, M. (2016). Soft Actuators for Small-Scale Robotics. *Advanced Materials*, (pp. 1603483).

[30] Hines, L., Petersen, K., Lum, G. Z., & Sitti, M. (2017). Soft actuators for small-scale robotics. *Advanced Materials*, 29(13).

[31] Hongbin, Y., Guangya, Z., Siong, C. F., Shouhua, W., & Feiwen, L. (2009). Novel polydimethylsiloxane (pdms) based microchannel fabrication method for lab-on-a-chip application. *Sensors and Actuators B: Chemical*, 137(2), 754–761.

[32] Hua, Z., Xia, Y., Srivannavit, O., Rouillard, J.-M., Zhou, X., Gao, X., & Gulari, E. (2006). A versatile microreactor platform featuring a chemical-resistant microvalve array for addressable multiplex syntheses and assays. *Journal of Micromechanics and Microengineering*, 16(8), 1433.

[33] Iida, F. & Laschi, C. (2011). Soft robotics: challenges and perspectives. *Procedia Computer Science*, 7, 99–102.

[34] Ilievski, F., Mazzeo, A. D., Shepherd, R. F., Chen, X., & Whitesides, G. M. (2011). Soft robotics for chemists. *Angewandte Chemie*, 123(8), 1930–1935.

[35] Jamal, M., Zarafshar, A. M., & Gracias, D. H. (2011). Differentially photo-crosslinked polymers enable self-assembling microfluidics. *Nature communications*, 2, 527.

[36] Jia, Y., Jiang, J., Ma, X., Li, Y., Huang, H., Cai, K., Cai, S., & Wu, Y. (2008). Pdms microchannel fabrication technique based on microwire-molding. *Chinese Science Bulletin*, 53(24), 3928–3936.

[37] Johnston, I., McCluskey, D., Tan, C., & Tracey, M. (2014). Mechanical characterization of bulk sylgard 184 for microfluidics and microengineering. *Journal of Micromechanics and Microengineering*, 24(3), 035017.

[38] Joyce, J. W. (1983). *Fluidics: basic components and applications*. Technical report, Harry Diamond Labs Adelphi MD.

[39] Kartalov, E. P., Scherer, A., Quake, S. R., Taylor, C. R., & Anderson, W. F. (2007a). Experimentally validated quantitative linear model for the device physics of elastomeric microfluidic valves. *Journal of applied physics*, 101(6), 064505.

[40] Kartalov, E. P., Scherer, A., Quake, S. R., Taylor, C. R., & Anderson, W. F. (2007b). Experimentally validated quantitative linear model for the device physics of elastomeric microfluidic valves. *Journal of applied physics*, 101(6), 064505.

[41] Kim, C.-C., Lee, H.-H., Oh, K. H., & Sun, J.-Y. (2016a). Highly stretchable, transparent ionic touch panel. *Science*, 353(6300), 682–687.

[42] Kim, J., Salvatore, G. A., Araki, H., Chiarelli, A. M., Xie, Z., Banks, A., Sheng, X., Liu, Y., Lee, J. W., Jang, K.-I., et al. (2016b). Battery-free, stretchable optoelectronic systems for wireless optical characterization of the skin. *Science advances*, 2(8), e1600418.

[43] Kim, S., Laschi, C., & Trimmer, B. (2013). Soft robotics: a bioinspired evolution in robotics. *Trends in biotechnology*, 31(5), 287–294.

[44] Koukharenko, E., Kraft, M., Ensell, G., & Hollinshead, N. (2005). A comparative study of different thick photoresists for mems applications. *Journal of Materials Science: Materials in Electronics*, 16(11-12), 741–747.

[45] Kwon, G. H., Park, J. Y., Kim, J. Y., Frisk, M. L., Beebe, D. J., & Lee, S. H. (2008). Biomimetic soft multifunctional miniature aquabots. *Small*, 4(12), 2148–2153.

[46] Landkammer, S., Winter, F., Schneider, D., & Hornfeck, R. (2016). Biomimetic Spider Leg Joints: A Review from Biomechanical Research to Compliant Robotic Actuators. *Robotics*, 5(3), 15.

[47] Larson, C., Peele, B., Li, S., Robinson, S., Totaro, M., Beccai, L., Mazzolai, B., & Shepherd, R. (2016). Highly stretchable electroluminescent skin for optical signaling and tactile sensing. *Science*, 351(6277), 1071–1074.

[48] Laschi, C., Cianchetti, M., Mazzolai, B., Margheri, L., Follador, M., & Dario, P. (2012). Soft robot arm inspired by the octopus. *Advanced Robotics*, 26(7), 709–727.

[49] Laschi, C., Mazzolai, B., & Cianchetti, M. (2016). Soft robotics: Technologies and systems pushing the boundaries of robot abilities. *Sci. Robot.*, 1(1), eaah3690.

[50] Lee, K., Kim, C., Shin, K. S., Lee, J. W., Ju, B.-K., Kim, T. S., Lee, S.-K., & Kang, J. Y. (2007). Fabrication of round channels using the surface tension of pdms and its application to a 3d serpentine mixer. *Journal of Micromechanics and Microengineering*, 17(8), 1533.

[51] Li, S., Vogt, D. M., Rus, D., & Wood, R. J. (2017). Fluid-driven origami-inspired artificial muscles. *Proceedings of the National Academy of Sciences*, (pp. 201713450).

[52] Lin, H.-T., Leisk, G. G., & Trimmer, B. (2011). Goqbot: a caterpillar-inspired soft-bodied rolling robot. *Bioinspiration & biomimetics*, 6(2), 026007.

[53] Lipson, H. (2014). Challenges and opportunities for design, simulation, and fabrication of soft robots. *Soft Robotics*, 1(1), 21–27.

[54] Liu, H.-B. & Gong, H.-Q. (2009). Templateless prototyping of polydimethylsiloxane microfluidic structures using a pulsed CO 2 laser. *Journal of Micromechanics and Microengineering*, 19(3), 037002.

[55] Liu, J., Williams, B. A., Gwirtz, R. M., Wold, B. J., & Quake, S. (2006). Enhanced signals and fast nucleic acid hybridization by microfluidic chaotic mixing. *Angewandte Chemie International Edition*, 45(22), 3618–3623.

[56] Liu, Y., Genzer, J., & Dickey, M. D. (2016). "2D or not 2D": Shape-programming polymer sheets. *Progress in Polymer Science*, 52, 79–106.

[57] Loepfe, M., Schumacher, C. M., Lustenberger, U. B., & Stark, W. J. (2015). An untethered, jumping roly-poly soft robot driven by combustion. *Soft Robotics*, 2(1), 33–41.

[58] Lu, N. & Kim, D.-H. (2014). Flexible and stretchable electronics paving the way for soft robotics. *Soft Robotics*, 1(1), 53–62.

[59] Lu, Y. & Chen, S. (2008). Direct write of microlens array using digital projection photopolymerization. *Applied Physics Letters*, 92(4), 041109.

[60] Majidi, C. (2014). Soft robotics: a perspective—current trends and prospects for the future. *Soft Robotics*, 1(1), 5–11.

[61] Marchese, A. D., Onal, C. D., & Rus, D. (2014). Autonomous soft robotic fish capable of escape maneuvers using fluidic elastomer actuators. *Soft Robotics*, 1(1), 75–87.

[62] Marchese, A. D. & Rus, D. (2016). Design, kinematics, and control of a soft spatial fluidic elastomer manipulator. *The International Journal of Robotics Research*, 35(7), 840–869.

[63] Maselli, V., Osellame, R., Cerullo, G., Ramponi, R., Laporta, P., Magagnin, L., & Cavallotti, P. L. (2006). Fabrication of long microchannels with circular cross section using astigmatically shaped femtosecond laser pulses and chemical etching. *Applied physics letters*, 88(19), 191107.

[64] McDonald, J. C., Chabinyc, M. L., Metallo, S. J., Anderson, J. R., Stroock, A. D., & Whitesides, G. M. (2002). Prototyping of microfluidic devices in poly (dimethylsiloxane) using solid-object printing. *Analytical chemistry*, 74(7), 1537–1545.

[65] McMahan, W., Chitrakaran, V., Csencsits, M., Dawson, D., Walker, I. D., Jones, B. A., Pritts, M., Dienno, D., Grissom, M., & Rahn, C. D. (2006). Field trials and testing of the octarm continuum manipulator. In *Robotics and Automation, 2006. ICRA 2006. Proceedings 2006 IEEE International Conference on* (pp. 2336–2341).: IEEE.

[66] Melin, J. & Quake, S. R. (2007). Microfluidic large-scale integration: the evolution of design rules for biological automation. *Annu. Rev. Biophys. Biomol. Struct.*, 36, 213–231.

[67] Mengüç, Y., Park, Y.-L., Pei, H., Vogt, D., Aubin, P. M., Winchell, E., Fluke, L., Stirling, L., Wood, R. J., & Walsh, C. J. (2014). Wearable soft sensing suit for human gait measurement. *The International Journal of Robotics Research*, 33(14), 1748–1764.

[68] Miserez, A., Schneberk, T., Sun, C., Zok, F. W., & Waite, J. H. (2008). The transition from stiff to compliant materials in squid beaks. *Science*, 319(5871), 1816–1819.

[69] Mosadegh, B., Polygerinos, P., Keplinger, C., Wennstedt, S., Shepherd, R. F., Gupta, U., Shim, J., Bertoldi, K., Walsh, C. J., & Whitesides, G. M. (2014a). Pneumatic Networks for Soft Robotics that Actuate Rapidly. *Advanced Functional Materials*, 24(15), 2163–2170.

[70] Mosadegh, B., Polygerinos, P., Keplinger, C., Wennstedt, S., Shepherd, R. F., Gupta, U., Shim, J., Bertoldi, K., Walsh, C. J., & Whitesides, G. M. (2014b). Pneumatic networks for soft robotics that actuate rapidly. *Advanced functional materials*, 24(15), 2163–2170.

[71] NuSil (2018). *MED4-4220 Data Sheet*. NuSil Technology. https://nusil.com/services/downloadfile.ashx?productcode=MED4-4220&originalname=MED4-4220.pdf.

[72] Oh, K. W., Lee, K., Ahn, B., & Furlani, E. P. (2012). Design of pressure-driven microfluidic networks using electric circuit analogy. *Lab on a Chip*, 12(3), 515–545.

[73] Onal, C. D., Chen, X., Whitesides, G. M., & Rus, D. (2017). Soft mobile robots with on-board chemical pressure generation. In *Robotics Research* (pp. 525–540). Springer.

[74] Onal, C. D. & Rus, D. (2013). Autonomous undulatory serpentine locomotion utilizing body dynamics of a fluidic soft robot. *Bioinspiration & biomimetics*, 8(2), 026003.

[75] Palleau, E., Morales, D., Dickey, M. D., & Velev, O. D. (2013). Reversible patterning and actuation of hydrogels by electrically assisted ionoprinting. *Nature Communications*, 4, 2257.

[76] Pandolfi, A. & Ortiz, M. (2006). Modeling new design of fluidic microvalves. In *Thermal, Mechanical and Multiphysics Simulation and Experiments in Micro-Electronics and Micro-Systems, 2006. EuroSime 2006. 7th International Conference on* (pp. 1–4).: IEEE.

[77] Park, Y.-L., Chen, B.-r., Pérez-Arancibia, N. O., Young, D., Stirling, L., Wood, R. J., Goldfield, E. C., & Nagpal, R. (2014). Design and control of a bio-inspired soft wearable robotic device for ankle–foot rehabilitation. *Bioinspiration & biomimetics*, 9(1), 016007.

[78] Perry, H., Greiner, C., Georgakoudi, I., Cronin-Golomb, M., & Omenetto, F. G. (2007). Simple fabrication technique for rapid prototyping of seamless cylindrical microchannels in polymer substrates. *Review of scientific instruments*, 78(4), 044302.

[79] Pfeifer, R., Iida, F., & Lungarella, M. (2014). Cognition from the bottom up: on biological inspiration, body morphology, and soft materials. *Trends in cognitive sciences*, 18(8), 404–413.

[80] Pfeifer, R., Lungarella, M., & Iida, F. (2007). Self-organization, embodiment, and biologically inspired robotics. *Science*, 318(5853), 1088–1093.

[81] Pfeifer, R., Lungarella, M., & Iida, F. (2012). The challenges ahead for bio-inspired'soft'robotics. *Communications of the ACM*, 55(11), 76–87.

[82] Polygerinos, P., Correll, N., Morin, S. A., Mosadegh, B., Onal, C. D., Petersen, K., Cianchetti, M., Tolley, M. T., & Shepherd, R. F. (2017). Soft robotics: Review of fluid-driven intrinsically soft devices; manufacturing, sensing, control, and applications in human-robot interaction. *Advanced Engineering Materials*.

[83] Polygerinos, P., Wang, Z., Galloway, K. C., Wood, R. J., & Walsh, C. J. (2015). Soft robotic glove for combined assistance and at-home rehabilitation. *Robotics and Autonomous Systems*, 73, 135–143.

[84] Psaltis, D., Quake, S. R., & Yang, C. (2006). Developing optofluidic technology through the fusion of microfluidics and optics. *Nature*, 442(7101), 381–386.

[85] Qin, D., Xia, Y., & Whitesides, G. M. (2010). Soft lithography for micro- and nanoscale patterning. *Nature protocols*, 5(3), 491–502.

[86] Quake, S. R. (2000). From Micro- to Nanofabrication with Soft Materials. *Science*, 290(5496), 1536–1540.

[87] Rafsanjani, A., Zhang, Y., Liu, B., Rubinstein, S. M., & Bertoldi, K. (2018). Kirigami skins make a simple soft actuator crawl. *Science Robotics*, 3(15), eaar7555.

[88] Ranzani, T., Russo, S., Bartlett, N. W., Wehner, M., & Wood, R. J. (2018). Increasing the dimensionality of soft microstructures through injection-induced self-folding. *Advanced Materials*, 30(38), 1802739.

[89] Rhee, M. & Burns, M. A. (2009). Microfluidic pneumatic logic circuits and digital pneumatic microprocessors for integrated microfluidic systems. *Lab on a chip*, 9(21), 3131–3143.

[90] Roberts, T. J. & Azizi, E. (2011). Flexible mechanisms: the diverse roles of biological springs in vertebrate movement. *Journal of Experimental Biology*, 214(3), 353–361.

[91] Rogoz, M., Zeng, H., Xuan, C., Wiersma, D. S., & Wasylczyk, P. (2016). Light-Driven Soft Robot Mimics Caterpillar Locomotion in Natural Scale. *Advanced Optical Materials*, 4(11), 1689–1694.

[92] Rohde, C. B., Zeng, F., Gonzalez-Rubio, R., Angel, M., & Yanik, M. F. (2007). Microfluidic system for on-chip high-throughput whole-animal sorting and screening at subcellular resolution. *Proceedings of the National Academy of Sciences*, 104(35), 13891–13895.

[93] Rosset, S. & Shea, H. R. (2016). Small, fast, and tough: Shrinking down integrated elastomer transducers. *Applied Physics Reviews*, 3(3), 031105.

[94] Rus, D. & Tolley, M. T. (2015). Design, fabrication and control of soft robots. *Nature*, 521(7553), 467.

[95] Russo, S., Ranzani, T., Walsh, C. J., & Wood, R. J. (2017). An Additive Millimeter-Scale Fabrication Method for Soft Biocompatible Actuators and Sensors. *Advanced Materials Technologies*, (pp. 1700135).

[96] Saggiomo, V. & Velders, A. H. (2015). Simple 3d printed scaffold-removal method for the fabrication of intricate microfluidic devices. *Advanced Science*, 2(9).

[97] Seok, S., Onal, C. D., Cho, K.-J., Wood, R. J., Rus, D., & Kim, S. (2013). Meshworm: a peristaltic soft robot with antagonistic nickel titanium coil actuators. *IEEE/ASME Transactions on mechatronics*, 18(5), 1485–1497.

[98] Shepherd, R. F., Ilievski, F., Choi, W., Morin, S. A., Stokes, A. A., Mazzeo, A. D., Chen, X., Wang, M., & Whitesides, G. M. (2011). Multigait soft robot. *Proceedings of the National Academy of Sciences*, 108(51), 20400–20403.

[99] Shepherd, R. F., Stokes, A. A., Freake, J., Barber, J., Snyder, P. W., Mazzeo, A. D., Cademartiri, L., Morin, S. A., & Whitesides, G. M. (2013). Using explosions to power a soft robot. *Angewandte Chemie*, 125(10), 2964–2968.

[100] Shian, S., Bertoldi, K., & Clarke, D. R. (2015). Dielectric elastomer based "grippers" for soft robotics. *Advanced Materials*, 27(43), 6814–6819.

[101] Song, S., Drotlef, D.-M., Majidi, C., & Sitti, M. (2017). Controllable load sharing for soft adhesive interfaces on three-dimensional surfaces. *Proceedings of the National Academy of Sciences*, (pp. 201620344).

[102] Song, S.-H., Lee, C.-K., Kim, T.-J., Shin, I.-c., Jun, S.-C., & Jung, H.-I. (2010). A rapid and simple fabrication method for 3-dimensional circular microfluidic channel using metal wire removal process. *Microfluidics and Nanofluidics*, 9(2-3), 533–540.

[103] Stergiopulos, C., Vogt, D., Tolley, M. T., Wehner, M., Barber, J., Whitesides, G. M., & Wood, R. J. (2014). A soft combustion-driven pump for soft robots. In *ASME 2014 Conference on Smart Materials, Adaptive Structures and Intelligent Systems* (pp. V002T04A011–V002T04A011).: American Society of Mechanical Engineers.

[104] Studer, V., Hang, G., Pandolfi, A., Ortiz, M., Anderson, W. F., & Quake, S. R. (2004). Scaling properties of a low-actuation pressure microfluidic valve. *Journal of applied physics*, 95(1), 393–398.

[105] Suzumori, K., Iikura, S., & Tanaka, H. (1991). Development of flexible microactuator and its applications to robotic mechanisms. In *Robotics and Automation, 1991. Proceedings., 1991 IEEE International Conference on* (pp. 1622–1627).: IEEE.

[106] Sydney Gladman, A., Matsumoto, E. A., Nuzzo, R. G., Mahadevan, L., & Lewis, J. A. (2016). Biomimetic 4D printing. *Nature Materials*, 15(January).

[107] Tanaka, H. & Wood, R. J. (2010). Fabrication of corrugated artificial insect wings using laser micromachined molds. *Journal of Micromechanics and Microengineering*, 20(7), 075008.

[108] Therriault, D., White, S. R., & Lewis, J. A. (2003). Chaotic mixing in three-dimensional microvascular networks fabricated by direct-write assembly. *Nature Materials*, 2(4), 265–271.

[109] Thorsen, T., Maerkl, S. J., & Quake, S. R. (2002). Microfluidic large-scale integration. *Science*, 298(5593), 580–584.

[110] Tolley, M. T., Shepherd, R. F., Karpelson, M., Bartlett, N. W., Galloway, K. C., Wehner, M., Nunes, R., Whitesides, G. M., & Wood, R. J. (2014a). An untethered jumping soft robot. In *Intelligent Robots and Systems (IROS 2014), 2014 IEEE/RSJ International Conference on* (pp. 561–566).: IEEE.

[111] Tolley, M. T., Shepherd, R. F., Mosadegh, B., Galloway, K. C., Wehner, M., Karpelson, M., Wood, R. J., & Whitesides, G. M. (2014b). A Resilient, Untethered Soft Robot. *Soft Robotics*, 1(3), 213–223.

[112] Tolley, M. T., Shepherd, R. F., Mosadegh, B., Galloway, K. C., Wehner, M., Karpelson, M., Wood, R. J., & Whitesides, G. M. (2014c). A resilient, untethered soft robot. *Soft Robotics*, 1(3), 213–223.

[113] Trimmer, B. (2014). Soft robot control systems: A new grand challenge?

[114] Trimmer, B., Bartlett, N. W., & Tolley, M. T. (2015). New developments in soft robotics: An interview with nicholas w. bartlett and michael t. tolley. *Soft Robotics*, 2(3), 93–95.

[115] Trivedi, D., Rahn, C. D., Kier, W. M., & Walker, I. D. (2008). Soft robotics: Biological inspiration, state of the art, and future research. *Applied bionics and biomechanics*, 5(3), 99–117.

[116] Truby, R. L. & Lewis, J. A. (2016). Printing soft matter in three dimensions. *Nature*, 540(7633), 371–378.

[117] Tumbleston, J. R., Shirvanyants, D., Ermoshkin, N., Janusziewicz, R., Johnson, A. R., Kelly, D., Chen, K., Pinschmidt, R., Rolland, J. P., Ermoshkin, A., et al. (2015). Continuous liquid interface production of 3d objects. *Science*, 347(6228), 1349–1352.

[118] Unger, M. A., Chou, H.-P., Thorsen, T., Scherer, A., & Quake, S. R. (2000). Monolithic microfabricated valves and pumps by multilayer soft lithography. *Science*, 288(5463), 113–116.

[119] Verma, M. K., Majumder, A., & Ghatak, A. (2006). Embedded template-assisted fabrication of complex microchannels in pdms and design of a microfluidic adhesive. *Langmuir*, 22(24), 10291–10295.

[120] Vogt, D. M., Park, Y.-L., & Wood, R. J. (2013). Design and characterization of a soft multi-axis force sensor using embedded microfluidic channels. *IEEE sensors Journal*, 13(10), 4056–4064.

[121] Waheed, S., Cabot, J. M., Macdonald, N. P., Lewis, T., Guijt, R. M., Paull, B., & Breadmore, M. C. (2016). 3d printed microfluidic devices: Enablers and barriers. *Lab on a Chip*.

[122] Wang, G.-J., Ho, K.-H., Hsu, S.-h., & Wang, K.-P. (2007a). Microvessel scaffold with circular microchannels by photoresist melting. *Biomedical microdevices*, 9(5), 657–663.

[123] Wang, G.-J., Hsueh, C.-C., Hsu, S.-h., & Hung, H.-S. (2007b). Fabrication of plga microvessel scaffolds with circular microchannels using soft lithography. *Journal of Micromechanics and Microengineering*, 17(10), 2000.

[124] Wang, Y.-C., Choi, M. H., & Han, J. (2004). Two-dimensional protein separation with advanced sample and buffer isolation using microfluidic valves. *Analytical chemistry*, 76(15), 4426–4431.

[125] Weaver, J. A., Melin, J., Stark, D., Quake, S. R., & Horowitz, M. A. (2010). Static control logic for microfluidic devices using pressure-gain valves. *Nature Physics*, 6(3), 218.

[126] Wehner, M., Tolley, M. T., Mengüç, Y., Park, Y.-L., Mozeika, A., Ding, Y., Onal, C., Shepherd, R. F., Whitesides, G. M., & Wood, R. J. (2014). Pneumatic energy sources for autonomous and wearable soft robotics. *Soft Robotics*, 1(4), 263–274.

[127] Wehner, M., Truby, R. L., Fitzgerald, D. J., Mosadegh, B., Whitesides, G. M., Lewis, J. A., & Wood, R. J. (2016a). An integrated design and fabrication strategy for entirely soft, autonomous robots. *Nature*, 536(7617), 451–455.

[128] Wehner, M., Truby, R. L., Fitzgerald, D. J., Mosadegh, B., Whitesides, G. M., Lewis, J. A., & Wood, R. J. (2016b). An integrated design and fabrication strategy for entirely soft, autonomous robots. *Nature*, 536(7617), 451.

[129] Whitney, J. P., Sreetharan, P. S., Ma, K. Y., & Wood, R. J. (2011). Pop-up book MEMS. *Journal of Micromechanics and Microengineering*, 21(11), 115021.

[130] Wong, K. H., Chan, J. M., Kamm, R. D., & Tien, J. (2012). Microfluidic models of vascular functions. *Annual review of biomedical engineering*, 14, 205–230.

[131] Wu, H., Odom, T. W., Chiu, D. T., & Whitesides, G. M. (2003). Fabrication of complex three-dimensional microchannel systems in PDMS. *Journal of the American Chemical Society*, 125(2), 554–559.

[132] Wu, H., Odom, T. W., & Whitesides, G. M. (2002). Reduction photolithography using microlens arrays: applications in gray scale photolithography. *Analytical chemistry*, 74(14), 3267–3273.

[133] Xia, Y. & Whitesides, G. M. (1998). Soft lithography. *Annual review of materials science*, 28(1), 153–184.

[134] Yang, D., Verma, M. S., So, J.-H., Mosadegh, B., Keplinger, C., Lee, B., Khashai, F., Lossner, E., Suo, Z., & Whitesides, G. M. (2016). Buckling pneumatic linear actuators inspired by muscle. *Advanced Materials Technologies*, 1(3).

[135] Zhang, Y., Zhang, F., Yan, Z., Ma, Q., Li, X., Huang, Y., & Rogers, J. A. (2017). Printing, folding and assembly methods for forming 3D mesostructures in advanced materials. *Nature Reviews Materials*, 2(4), 17019.

[136] Zhou, F., Cao, W., Dong, B., Reissman, T., Zhang, W., & Sun, C. (2016). Additive manufacturing of a 3d terahertz gradient-refractive index lens. *Advanced Optical Materials*.